5-2014

Simulation of Materials Erosion and Lifetime Under Intense Radiation Heat Sources

Ghadeer H. Al-Malkawi
Purdue University

Graduate School ETD Form 9
(Revised 01/14)

PURDUE UNIVERSITY
GRADUATE SCHOOL
Thesis/Dissertation Acceptance

This is to certify that the thesis/dissertation prepared

By Ghadeer Hamzeh Al-Malkawi

Entitled
Simulation of Materials Erosion and Lifetime Under Intense Radiation Heat Sources

For the degree of Doctor of Philosophy

Is approved by the final examining committee:

Dr. Ahmed Hassanein

Dr. Valeryi Sizyuk

Dr. Anter El-Azab

Dr. Edwin Garcia

Dr. Sivanandan Harilal

To the best of my knowledge and as understood by the student in the *Thesis/Dissertation Agreement. Publication Delay, and Certification/Disclaimer (Graduate School Form 32)*, this thesis/dissertation adheres to the provisions of Purdue University's "Policy on Integrity in Research" and the use of copyrighted material.

Dr. Ahmed Hassanein

Approved by Major Professor(s): _____

_____

Approved by: Dr. Ahmed Hassanein 04/16/2014

Head of the Department Graduate Program Date

SIMULATION OF MATERIALS EROSION AND LIFETIME UNDER INTENSE RADIATION HEAT SOURCES

A Dissertation

Submitted to the Faculty

of

Purdue University

by

Ghadeer H. Al-Malkawi

In Partial Fulfillment of the

Requirements for the Degree

of

Doctor of Philosophy

May 2014

Purdue University

West Lafayette, Indiana

ACKNOWLEDGEMENTS

I would like to express my sincere gratitude and deepest appreciation to my advisor Prof. Ahmed Hassanein for his patience, motivation, immense knowledge, and continuous support and encouragement. His guidance helped me in all the time of my PhD study and research. I am also thankful for the excellent example he has provided as a successful professor.

I would like to thank the rest of my thesis committee: Prof. Sivanandan S. Harilal, Prof. Edwin Garcia, Prof. Anter El-Azab, and Prof. Valeryi Sizyuk, for their encouragement and insightful comments and advices.

I thank all my friends in the Unites states and Jordan for providing support and friendship that I needed. Their support and care helped me stay focused on my graduate study. Special thanks to my friend Shazia who helped me in taking care of my kids.

I also would like to thank my family and my in laws for their love, nice advices, help, and support during my study.

I especially thank my mom, dad, brother, and sisters, Abeer and Alaa. My parents have devoted much of their lives for us and provided unconditional love, care, and endless support. I love them so much, and I would not have progressed this far without them. My sisters are my best friends I want to thank both of you for your kind and love.

Special thanks to my brother Mohammad who helped me during many difficult times. His support from the first day I came to the US will never be forgotten.

There are no words to convey how much I thank my caring, loving, and unbelievably supportive husband, Montaser. I would like to thank him for showing me the beauty and opposite side of life and making my mind relax during the hard times of my study.

Finally, I would like to thank my three wonderful children, Arab, Maryam, and Ahmad for giving me happiness and for being very patient during the time I spent away from them. Thank you my kids for giving up your time that is supposed to be spent by take caring of you, I love you so much and I promise you that the near future will be more dedicated for you.

TABLE OF CONTENTS

Page

Page

LIST OF TABLES

LIST OF FIGURES

Figure Page

Figure Page

Figure Page

Figure Page

Figure Page

LIST OF ABBREVIATIONS

AFM	Atomic Force Microscope
CMUXE	Center for Materials Under eXtreme Environment
CPPS	Critical Point Phase Separation
DOS	Density of State
HAZ	Heat-Affected Zone
HEDP Lab	High Energy Density Physics laboratory
SEM	Scanning Electron Microscope
TTM	Two-Temperature Model

NOMENCLATURE

A	molar mass of the target (g/mol)
A_e	material constant for electron-phonon coupling factor ($s^{-1}k^{-2}$)
Be	coefficient for the electron heat capacity ($Jcm^{-3}k^{-2}$)
B_l	material constant for the electron-phonon coupling factor ($s^{-1}k^{-1}$)
C_e	electron heat capacity ($Jcm^{-3}k^{-1}$)
C_l	lattice heat capacity ($Jg^{-1}K^{-1}$)
g(ε)	the electron density of state at energy level ε
G	electron-phonon coupling factor ($Wcm^{-3}K^{-1}$)
G_l	liquid Gibbs free energy ($Jmol^{-1}$)
G_v	vapor Gibbs free energy ($Jmol^{-1}$)
$I_\circ$	the maximal power density (Wcm^{-2})
k_B	Boltzmann's constant (JK^{-1})
Ke	electron thermal conductivity ($Wm^{-1}K^{-1}$)
K_l	lattice thermal conductivity ($Wm^{-1}K^{-1}$)
L_v	latent heat of vaporization (J/g)
m_e	the effective electron mass (g)
n_e	density of the free electrons (cm^{-3})
P_v	vapor pressure (Pa)
$P_\circ$	reference pressure (Pa)

r	radial direction.
R	reflectivity.
r_b	the spot radius of the laser beam (cm)
s	the entropy ($Jmol^{-1}K^{-1}$)
S(r,z,t)	the time and space dependent volumetric laser energy (Wcm^{-3})
t	time (sec)
T_{amb}	ambient temperature (K)
T_{cr}	thermodynamic critical temperature (K)
T_D	the Debye temperature (K)
T_e	electron temperature (K)
T_F	the Fermi temperature (K)
T_l	lattice temperature (K)
T_m	melting temperature (K)
t_p	the laser pulse width (sec)
V	the volume (cm^3)
V_s	the speed of sound (cm/s)
z	direction along the depth

LIST OF SYMBOLS

α	the absorption coefficient
ε	the energy level
η	material constant for electronic conductivity coefficient
$\hbar$	the reduced Planck constant
λ	the electron-phonon mass enhancement parameter
$\langle\omega^2\rangle$	the second moment of the phonon
ρ	the temperature dependent density of the target
σ	spatial profile parameter
τ_e	the electron relaxation time
$\tau_{e\text{-}p}$	the electron phonon thermalization time
τ_p	the lattice relaxation time
χ	material constant for electronic conductivity coefficient

ABSTRACT

Al-Malkawi, Ghadeer H. Ph.D., Purdue University, May 2014. Simulation of Materials Erosion and Lifetime under Intense Radiation Heat Sources. Major Professor: Ahmed M. Hassanein.

The purpose of the present study was to investigate the energy transport through target materials irradiated by ultrashort laser pulses, which is characterized by the extremely high power density. The heat transfer and the ablation of the irradiated target were described numerically by the two-dimensional two-temperature model with temperature and phase dependent thermophysical properties of the electron and the lattice subsystems such as the heat capacity, the thermal conductivity, and the density. Based on the characteristics of the ultrashort laser heating two ablation mechanisms were used to estimate the ablation depth and the corresponding ablated mass and volume: the normal evaporation and phase explosion mechanisms. The impact of the total energy, spot size, reflectivity, and the electron- phonon coupling factor on the thermal evolution and the crater shape and size was investigated. Different models of temperature dependent electron-phonon coupling and electron heat capacity based on the calculation of the electronic structure of the density of state and other models based on the electron-electron and electron-lattice collision rate of copper irradiated by femtosecond laser pulse were

used to investigate the temporal and spatial thermal evolution and the corresponding ablation as well.

Due to the unique properties of the irradiation by ultrashort laser pulse with minimum heat-affected zone in target materials which makes it a promise choice for many applications, the coating was chosen as one of these applications by studying the double-layer irradiation by femtosecond laser where the first layer was the gold and the substrates were copper and aluminum. The impact of the thermal properties of the substrate on the thermal response of the first layer was investigated by analyzing the temporal and spatial electron and lattice temperature. Moreover some experiments were performed in order to validate the simulation results. In these experiments a set of copper target were prepared and irradiated by several energies of femtosecond laser pulses. The effect of crater depth on the number of pulses was studied by shooting various number of laser pulses at different spots and measuring the produced crater depths. The post irradiated samples were evaluated quantitatively and qualitatively by using the Atomic Force Microscope and the Scanning Electron Microscope respectively. Finally, a comparison between the experimental results and the simulation results was presented.

CHAPTER ONE: INTRODUCTION

Motivation

The study of laser matter interaction is an important research topics for several applications ranging from industrial applications to defense and national security applications in which an intense and high power radiation is needed. The presence of materials in the environment of the intense irradiation from high intensity lasers may cause severe damage to that material; therefore studying the physics of the laser material interaction will help to minimize/maximize the damage that may occur in this case depending on the application and the required goals. The ablation of the material irradiated by laser pulses became the basic process for many applications such as in industry, material science, defense, medicine, etc.

The duration of the laser pulse is a significant parameter that determines the thermal and mechanical response of the irradiated material; this was confirmed by studying the thermal evolution and the ablation of an irradiated material by short or ultrashort laser pulse. Any laser pulse with a duration of few picoseconds or shorter is considered as ultrashort laser pulse which is the topic of this study.

The ultrashort laser pulses have some unique properties such as the very high intensities, rapid deposition of the energy into materials, negligible heat-affected zone

(HAZ), and precise ablation. Besides that, the ultrafast laser can prevent the effect of the shielding of the incoming laser beam from the plasma that formed from the ablation, which causes higher absorption of the incoming laser energy. These properties of the ultrashort lasers make it a promising option for some special applications especially the ones that need high precision such as surface micromachining, pulsed laser precise processing of highly sensitive materials, surface alloying, femtosecond laser heating of thin films, coating, laser patterning, producing a self-arranged nanostructure, and various medical applications such as brain surgery and removing tumor tissue (Al-Nimr & Arpacib, 2000; R. Fang et al., 2008; Furusawa et al., 2000; Gurevich, Kittel, & Hergenröder, 2012; Jiang & Tsai, 2007; H. Lee, Jeong, & Chan, 2009; Oraevsky et al., 1995; Sonntag, Roth, Gaehler, & Trebin, 2009). Computer simulations were performed to study the thermal response of the irradiated materials by the ultrashort lasers and many experiments were carried out to verify the theoretical models (Colombier, Combis, Bonneau, Le Harzic, & Audouard, 2005; Ihtesham, Xianfan, & Andrew, 2003; Kim & Na, 2007; Oh, Kim, Kim, & Lee, 2007).

The aim of this work is to study the thermal response of metals that are irradiated by intense radiation of ultrashort laser pulses and the corresponding ablation and crater shape. The interaction between femtosecond laser pulse and copper target was studied theoretically based on two-dimensional two-temperature model (TTM) with temperature dependent thermal properties. Different models were used to study the impact of the electron-phonon coupling and the electron heat capacity on the thermal response of the irradiated material. In addition, some experiments have been performed in our center for

materials under extreme environment (CMUXE) in order to benchmark the simulation results. Finally, the simulation of the femtosecond laser interaction with double-layer metal films as an application of ultrashort laser pulses has been done. Full literature review is presented in the upcoming chapters.

The Physics of Ultrashort Laser Material Interaction

The thermal evolution in a material due to the interaction with the laser pulse of ultrashort duration (femtosecond or picosecond) is different from that irradiated by longer pulse width, since the time for the electron and phonon subsystems to reach the equilibrium ranges from 4 ps to 10 ps, which is larger than the pulse duration compared to nanosecond or millisecond laser pulses.

In order to explain this effect, the two-temperature model that is proposed by Anisimov et al. (1974) was used. This mathematical model introduces a clear explanation of the energy transport by dealing with the target as electrons and lattice subsystems. Once the ultrashort irradiation is applied on the material surface the free electrons absorb the photons directly by the inverse Bremsstrahlung process causing electron excitation. After the equilibrium is achieved between the electrons, rapid coupling to that lattice occurs by electron phonon collisions that lead to an increase of the lattice temperature until the equilibrium between the electron and the lattice is achieved. The mechanism of the non-equilibrium energy transport in any material irradiated by ultrashort laser pulse is illustrated in the schematic figure 1.1. The mathematical

equations that explain this model are presented in details in chapters 2 which is our published paper (Al-Malkawi & Hassanein, 2013).

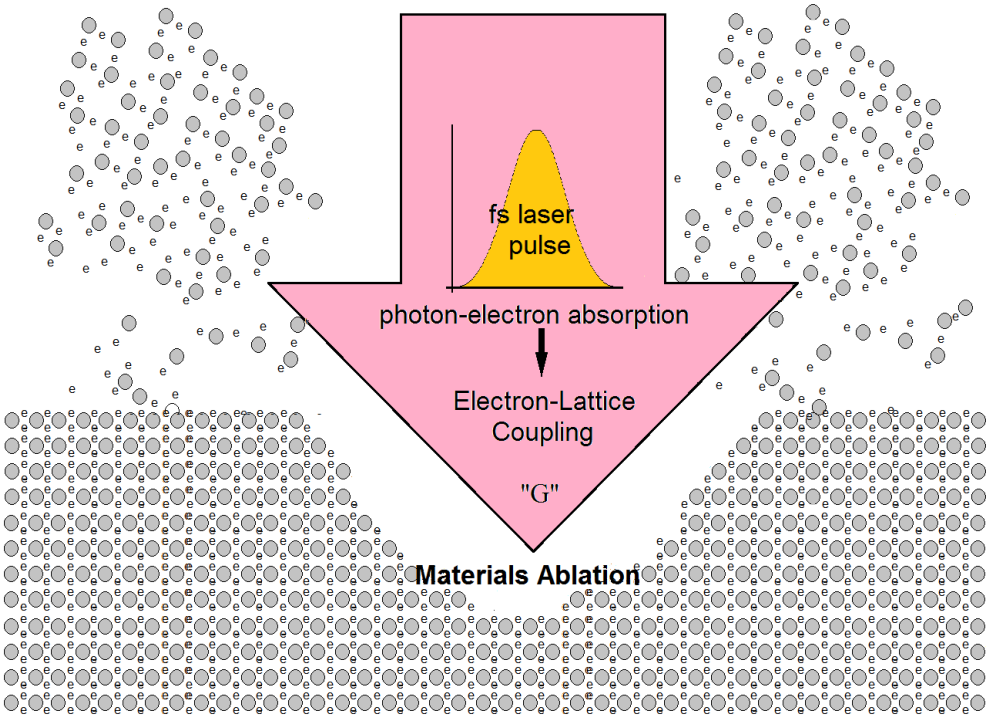

Figure 1.1 Schematic non-equilibrium thermal transport of the ultrashort laser pulse.

In the two-step model originated by Anisimov et al. the lattice heat conduction was neglected because of the slow diffusion in the lattice subsystem. After that Qiu and Tien (1993) used the Boltzmann heat equation and modified the model to the hyperbolic two-step radiation heating model and then they simplified it to the parabolic two-step model. Chen and Beraun (2001) modified Qiu and Tien model to the dual hyperbolic two-step

radiation model with taking into account the lattice heat conduction which added a higher precision to the results.

In the study of the ultrafast heating of materials by femtosecond and picosecond laser pulses we are interested in the three characteristics times (Marla, Bhandarkar, & Joshi, 2011); the electron relaxation time, τ_e, which represents the time needed for thermalization during the electrons subsystem, the other one is the electron-phonon thermalization time, $\tau_{e\text{-}p}$, this represents the time required to reach the equilibrium between the electronic and the lattice subsystems, and the last one is the lattice relaxation time, τ_p, which is the time needed for the thermalization of the lattice. The length of these times determines the heating process, in the case of our study of ultrashort laser the electron-phonon relaxation time is larger than the length of the laser pulse, therefore the two-step model is needed to study the heating process and the corresponding ablation and crater size.

Material Ablation By Ultrashort Laser Pulse

When the laser energy is absorbed by the irradiated surface the ejection of the particles in different phases (vapor, melt, solid) may occur, this depends on the laser parameters such as total energy, pulse duration, spot size, wavelength, and the thermal properties of the irradiated target. The main properties that made the femtosecond laser a good choice for the applications that need producing of precise and clean holes with wide range of materials compared to long pulses are the negligible heat-affected zone, high

peak intensity that can be achieved with low pulse energy, and negligible melt region (X. Liu, Du, & Mourou, 1997).

Different mechanisms were proposed in the literature to estimate the ablated depth and mass for wide range of materials numerically and experimentally such as the thermal evaporation (Jiang & Tsai, 2007), normal boiling, phase explosion (Bulgakovaa & Bourakov, 2002; Changrui & Chowdhury, 2004; Kim & Na, 2007), phase separation (Wu & Shin, 2007), fragmentation (Lorazo, Lewis, & Meunier, 2003; Nedialkov, Imamova, Atanasov, Berger, & Dausinger, 2005), and spallation (Nedialkov, et al., 2005; Zhigilei, Lin, & Ivanov, 2009).

In this work we studied both the heterogeneous and the homogeneous nucleation by thermal evaporation and phase explosion respectively. At low energies the ablation occurs mainly by the thermal evaporation in which the bubbles are formed at the surface of the irradiated target leading to ablation, the ablated mass and the crater size were calculated using the governing equations for the thermal evaporation in which the recession velocity and the vapor pressure at the surface temperature can be calculated (A. M. Hassanein, 1983). For high energies of ultrashort laser the main mechanism of the material ablation is the phase explosion, the ultrafast heating causes sudden increasing in the temperature to the value higher than the boiling temperature at given pressure and near the critical temperature. Superheated liquid in this region has a large fluctuation in density and entropy that leads to the nucleation of bubbles in the bulk of the target, and when the bubbles radius reaches a critical size the explosion occurs as a mixture of gas and liquid droplets from the bulk. Any point with a temperature of 0.9 of the

thermodynamic critical temperature or greater is eliminated. The detailed discussion of the ablation mechanisms is presented in chapter 3.

The simulation of the thermal evolution through the target irradiated by the ultrashort laser pulses and the corresponding ablation has been performed by using the finite difference techniques in A*THERMAL-2 computer code (A. Hassanein, 1996) which is modified to solve the two-dimensional two-temperature model equations for single and multi-layer target system with temperature dependent thermal properties. The flow chart of the code is shown in figure 1.2 (A. M. Hassanein, 1983).

As shown in this flow chart, the phase change from solid to liquid and the evaporation was considered in the calculations with moving boundaries. The phase and temperature dependent thermal properties for several materials are included. The code can be used to simulate the thermal response and life time analysis of the target irradiated by different types of heat sources.

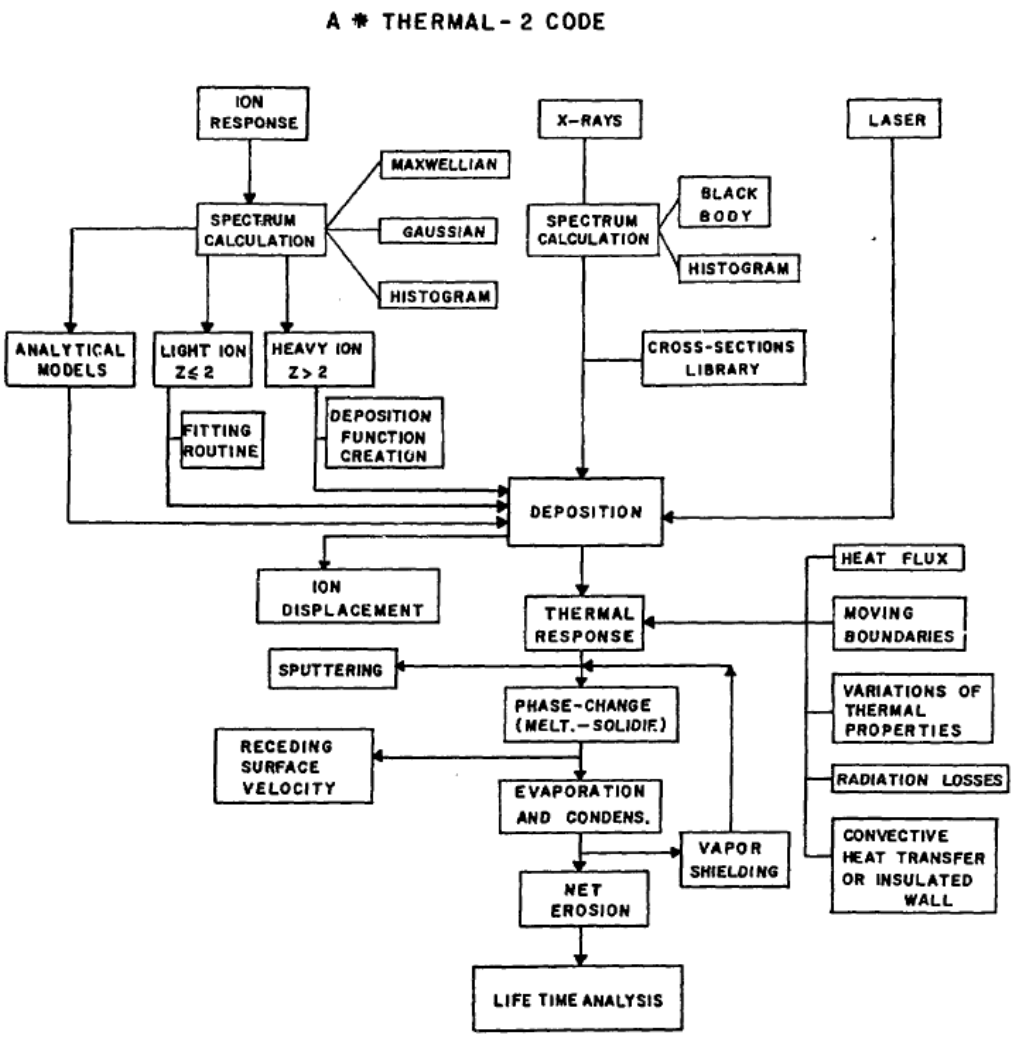

Figure 1.2 Flow chart of the computer code A*THERMAL-2 (A. M. Hassanein, 1983)

Experimental Study of Ultrashort Laser Pulses

The practical investigations of the femtosecond laser ablation have started during the eighties of the last century. At that earlier time people noticed the main characteristic of the ultrashort laser ablation mechanism where optimum material removal without molten layer with lower ablation threshold has been reported. Many experiments have been done in the literature to investigate the ablation behavior during the short and ultrashort laser pulses interacting with different materials under different laser conditions and to verify the heating and ablation theoretical models. In order to validate the simulation results for femtosecond laser ablation of copper target a set of copper samples were mechanically polished and irradiated by femtosecond pulses of T:Sapphire laser at 800 nm wavelength. The laser produced surface craters were analyzed qualitatively and quantitatively to benchmark the simulation results. Detailed discussion of the literature review is presented in chapter 6.

CHAPTER TWO: NON-EQUILIBRIUM TWO-DIMENSIONAL THERMAL EVOLUTIONS IN TARGET MATERIALS IRRADIATED BY FEMTOSECOND LASER

Introduction

The study of ultrashort laser pulses (picosecond and femtosecond) is one of the important evolving research fields because of its unique advantage of having high precision material ablation by extreme high-energy intensities with negligible thermal or heat-affected zone. This is because of the very short interacting time period, which is less than the time needed to reach the thermal equilibrium. The ultrashort laser pulses interacting with materials is used for many applications (Al-Nimr & Arpacib, 2000; R. Fang, et al., 2008; Furusawa, et al., 2000; Gurevich, et al., 2012; Jiang & Tsai, 2007; Sonntag, et al., 2009) such as drilling, welding, cutting, micromachining, precise processing of highly sensitive materials , surface alloying, femtosecond laser heating of thin films, laser patterning and various medical applications such as brain surgery and removing tumor tissue (H. Lee, et al., 2009; Oraevsky, et al., 1995). The physics of ultrashort pulses differs from that of the nanosecond or millisecond range pulses because the pulse width is less than the time needed to reach the thermal equilibrium state between the electrons and the phonons. During the irradiation of metals by picosecond or femtosecond laser pulses the electrons absorb the photon energy and then the heating of

the metal lattice occurs by the electron-phonon collisions (Ihtesham, Chowdhury, & Xianfan, 2003; Sonntag, et al., 2009; Zhang & Chen, 2007).

The non-equilibrium heat transfer between the electrons and the lattice can be described by the two-temperature model, which was first proposed by Anisimov et al. (1974) In this model the heat conduction by the lattice was neglected. After that, Qiu and Tien (1993) used the Boltzmann heat equation and developed the hyperbolic two-step radiation heating model and was simplified to the parabolic two-step model that has been solved numerically and has a reasonable agreement with experimental results. Then Qiu and Tien model was modified by Chen and Beraun (2001) dual hyperbolic two-step radiation model in which the heat conduction of the lattice was considered, the electron temperature from both models was very close while there was a remarkable difference in the lattice temperature.

The energy equations that describe the non-equilibrium heat transfer in the two-step model are given below (Al-Nimr & Arpacib, 2000; Ihtesham, Chowdhury, et al., 2003; Jiang & Tsai, 2007; Zhibin Lin, Zhigilei, & Celli, 2008; Sonntag, et al., 2009; Zhang & Chen, 2007):

$$C_e \frac{\partial T_e}{\partial t} = \nabla.(K_e \nabla T_e) - G(T_e - T_l) + Q(\vec{r}, t) \quad (2.1)$$

$$C_l \frac{\partial T_l}{\partial t} = \nabla.(K_l \nabla T_l) + G(T_e - T_l) \quad (2.2)$$

Where T is the temperature, t is the time, C is the volumetric specific heat, K is the thermal conductivity, where the subscripts e and l are associated with the electron and lattice respectively, G is the coupling factor that describes the interaction between the

electrons and the lattice, and Q is the volumetric laser energy deposition rate as a function of space and time.

Equation 2.1 describes the heat absorbed by electrons, the electronic heat conduction, the transfer of heat between the electrons and the lattice, and the energy distribution of the laser in time and space. The second equation describes the heat transfer through the lattice, heat conduction and the coupling heat with the electron system.

The laser heating source as a function of space and time can be described by the following expression:

$$Q(x,y,z,t) = I_{\circ}(1-R)I(t)I(x,y,z) \tag{2.3}$$

Where $I_{\circ}$ is the maximum power density, R is the reflectivity, I(t) and I(x,y,z) are the temporal distribution and the spatial distribution of the power density respectively.

Input and Assumptions

In this work a two-dimensional model for the solution of the transient heat transfer equations was developed with temperature and phase change dependent thermal properties (density, thermal conductivity, and specific heat) for both the electron and the lattice. The heat conduction term in the lattice energy equation was neglected because of the slow diffusion in the lattice system during the pulse duration. The Gaussian distribution was assumed for both the time (Tan et al., 2009) and the space (A. M. Hassanein, 1983) for the heating source. Therefore, the energy transport equations become:

$$Ce\frac{\partial T_e}{\partial t} = \frac{1}{r}\frac{\partial}{\partial r}\left(K_e\, r\frac{\partial T_e}{\partial r}\right) + \frac{\partial^2 T_e}{\partial z^2} - G(T_e - T_l) + S(r,z,t) \tag{2.4}$$

$$C_l \frac{\partial T_l}{\partial t} = G(T_e - T_l) \tag{2.5}$$

Equation 2.4 describes the heat transfer in cylindrical coordinate system where r is the radial direction and z is the direction along the depth inside the target, S(r, z, t) is the volumetric energy from the laser and it depends on r, z, and t as follows:

$$S(r,z,t) = I_{\circ}(1-R)\alpha\, I_{surf}\ (\mathrm{r})\mathrm{I(t)}\exp(-\alpha z) \tag{2.6}$$

$$I_{surf}\ (\mathrm{r}) = \exp\left(-\frac{r^2}{2\sigma^2}\right) \tag{2.7}$$

$$\mathrm{I(t)} = \exp\left(-\frac{\left(t-t_p\right)^2}{\tau^2}\right) \tag{2.8}$$

where α is the absorption coefficient, $I_{\circ}$ is the maximal power density, t_p is the laser pulse width in time, and $\sigma = r_b/2$ where r_b is the spot radius of the laser beam.

Thermo Physical Properties and Temperature Dependence

In this work the thermal properties of electron and lattice such as thermal conductivity, density, and heat capacity were assumed to be dependent on temperature, the following equations describe such dependency (A. M. Chen, Jiang, Sui, Ding, et al., 2011; Huang, Zhang, & Chen, 2009; Ihtesham, Chowdhury, et al., 2003; Zhibin Lin, et al., 2008; Ren, Chen, & Zhang, 2011; Zhang & Chen, 2007):

The thermal conductivity of electron is given by:

$$k_e = \chi\left(\frac{(\mu_e^2+0.16)^{5/4}(\mu_e^2+0.44)\mu_e^2}{(\mu_e^2+0.092)^{1/2}(\mu_e^2+\eta\mu_l)}\right) \tag{2.9}$$

where χ and η are material constants, $\mu_e = T_e/T_F$, $\mu_l = T_l/T_F$, and T_F is the Fermi temperature.

The specific heat of the electron is usually a linear function of electron temperature, is given by

$$C_e = B_e T_e \tag{2.10}$$

where $B_e = \pi^2 n_e k_B/2T_F$, n_e is the density of the free electrons, and k_B is the Boltzmann's constant.

The lattice specific heat is in the form of:

$$C_l = a + b T_l + c T_l^2 + dT_l^3 \tag{2.11}$$

where a, b, c, and d are constants which depend on the material.

The density of the material have been assumed temperature and phase dependent and it is given by

$$\rho = c_0 + c_1 T_l + c_2 T_l^2 + c_3 T_l^3 \tag{2.12}$$

where c_0, c_1, c_2, and c_3 are constants that depend on the material and it's phase. Most of the constants in these equations are tabulated in table 2.1 for the copper (Ranran Fang et al., 2010; Ren, Chen, & Zhang, 2011; Ren, Chen, Zhang, & Huang, 2011) (A. M. Chen, Y. F. Jiang, L. Z. Sui, D. J. Ding, et al., 2011; Huttner, 2009; Zhibin Lin, et al., 2008; Tan, et al., 2009)and other constants are taken from A*THERMAL-2 code (A. Hassanein, 1996).

Table 2.1

Thermal and Optical Properties of Copper

G W/cm^3K	R	α cm^{-1}	T_F K	B_e J/cm^3K^2	χ	η	T_m K
2.5×10^{11}	0.94	7.1×10^{5}	8.12×10^{4}	96.6×10^{-6}	3.77	0.14	1356

Initial and Boundary Conditions

The initial value of the target temperature is assumed to be the ambient temperature (300K) as well as the temperature far away from the exposed surface in r direction and also very far from the center in z direction.

$T(r, z, t=0) = T_{amb} = 300$ K

$T(r=\infty, z, t) = T_{amb} = 300$ K

$T(r, z=\infty, t) = T_{amb} = 300$ K

The adiabatic boundary conditions have been assumed for both sides in r and z directions:

$$\frac{dT}{dr} = 0 \ , \qquad for\ z = 0, \infty$$

$$\frac{dT}{dz} = 0 \ , \qquad for\ r = 0, \infty$$

In this chapter the two-temperature model was used to predict the thermal response of copper target with an ambient temperature of 300 K when exposed to ultrashort laser pulse of 100 fs, spot size of 40 microns, and with a total laser energy of 3.5 μJ. For

equations 2.6, 2.7, and 2.8 the maximum power density was calculated to be 1.5×10^{13} W/cm^2 (Al-Malkawi & Hassanein, 2013).

Results and Discussion

The calculation for our two-dimensional heat transfer equations was implemented using non-equilibrium heat transfer equations by modifying the A*THERMAL-2 computer code developed by Hassanein (1996). The finite difference methods were used to calculate both the electron temperature and the lattice temperature. For the 100 fs laser pulse with 40μm spot size the time step was 0.5 fs up to 100 fs and then increased to 5 fs to the end of the run time. The mesh size in r-direction was 0.5μm and it was changing in z-direction to speed up the calculations but maintain the accuracy.

The temporal distribution of laser power density is shown in figure 2.1, the black solid line describes the incoming laser power density while the red dotted lined describes the absorbed power density after the reflection, the total absorbed energy is much lower than the input source energy because of high value of reflectivity of copper which is about 0.94. It can be seen that the power density has its maximum value: 1.5×10^{13} W/cm^2 and 9×10^{11} W/cm^2 for the incoming and absorbed power density respectively at 50 fs and vanishes at 100 fs the end of the pulse.

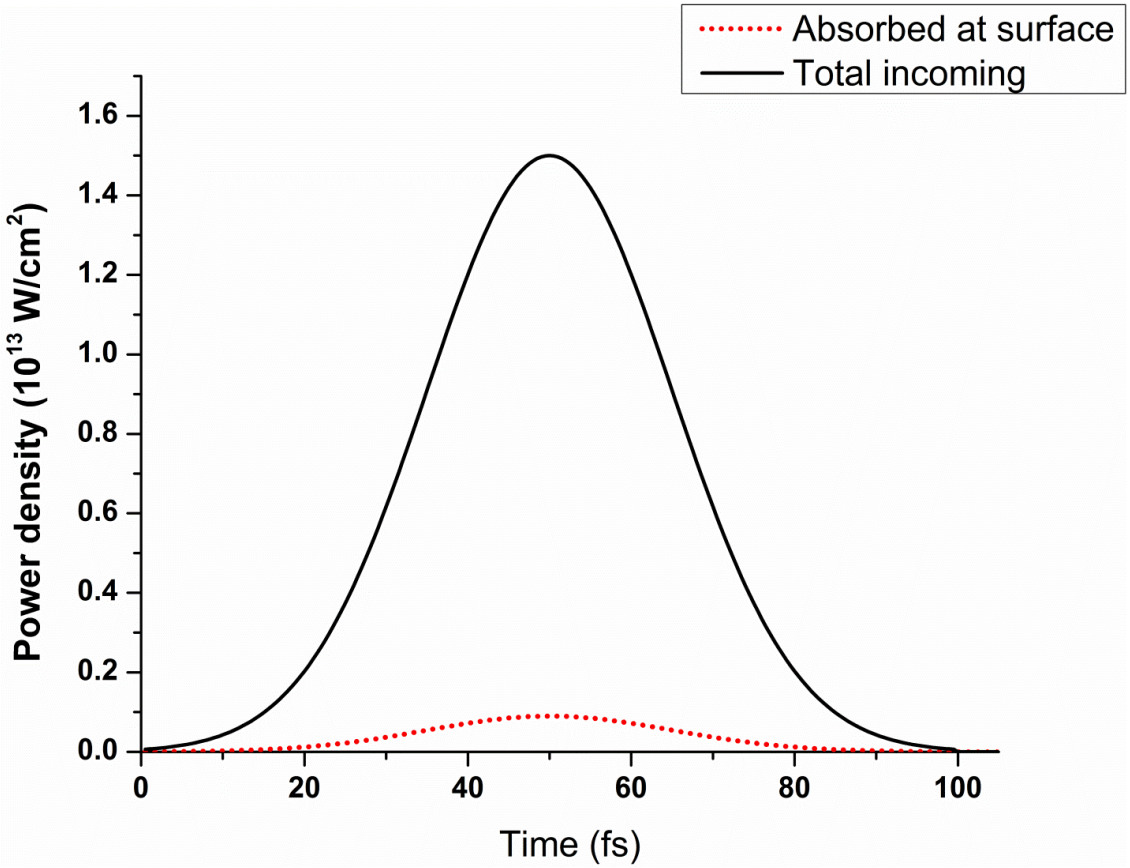

Figure 2.1 Temporal distribution of the laser beam power density of 100 fs, I_0 of 1.5×10^{13} W/cm^2 and R of 0.94

Figure 2.2 shows the spatial distribution of power density (incoming and absorbed) at the surface, the maximum power density is at the center of the laser beam (at r =0) and it decreases exponentially according to equation 2.7.

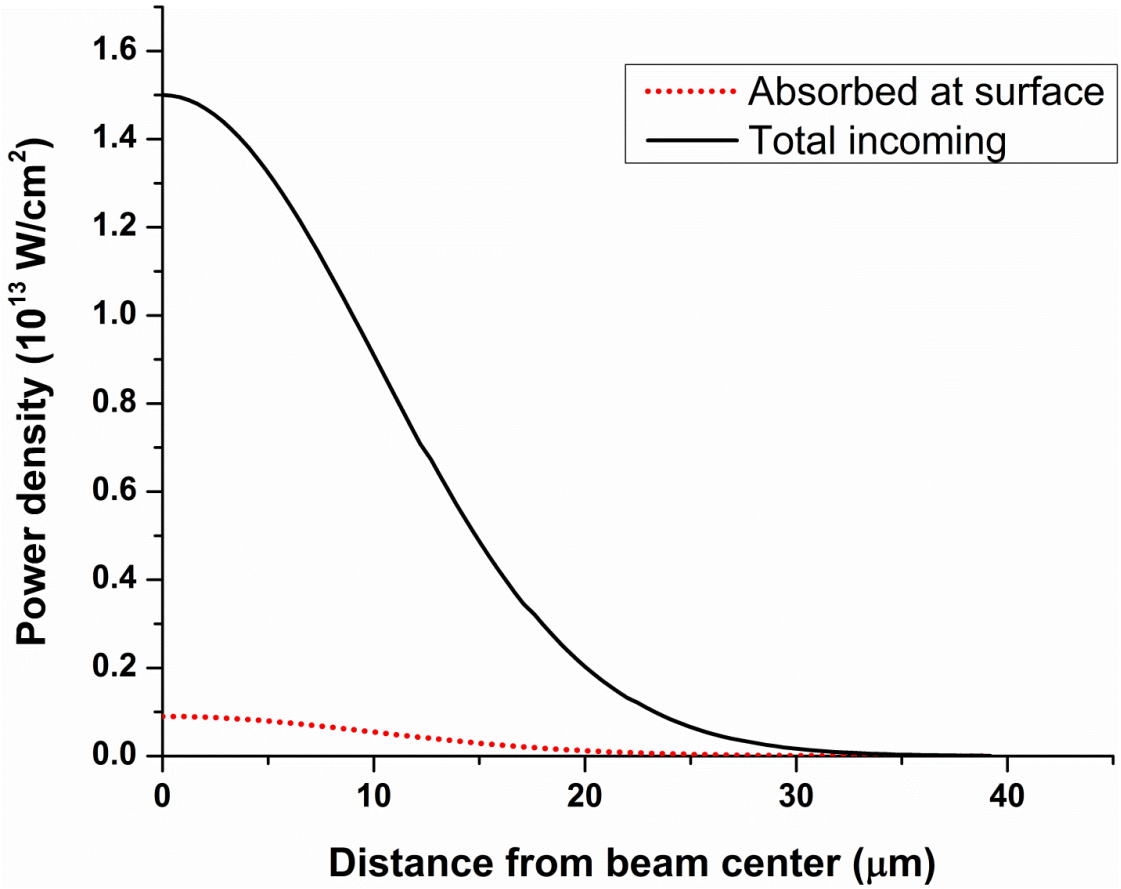

Figure 2.2 Spatial distribution of the laser beam power density of 100fs, I_0 of 1.5×10^{13} W/cm^2, R of 0.94 and spot radius of 20 μm at 50 fs

Figure 2.3 shows the temporal temperature distribution at the center of the laser beam for both the electron and the lattice, the electron temperature increases very fast within few femtoseconds and reaches to about 11700 K while the lattice temperature increases very slow. At this stage the electrons absorb the photons from the laser and their temperature remains constant to the end of the pulse duration as shown in the upper part of this figure. Then the electrons transfer the absorbed energy to other Electrons as well as through the coupling with the phonons, so the temperature of electrons decreases while the lattice temperature increases as shown.

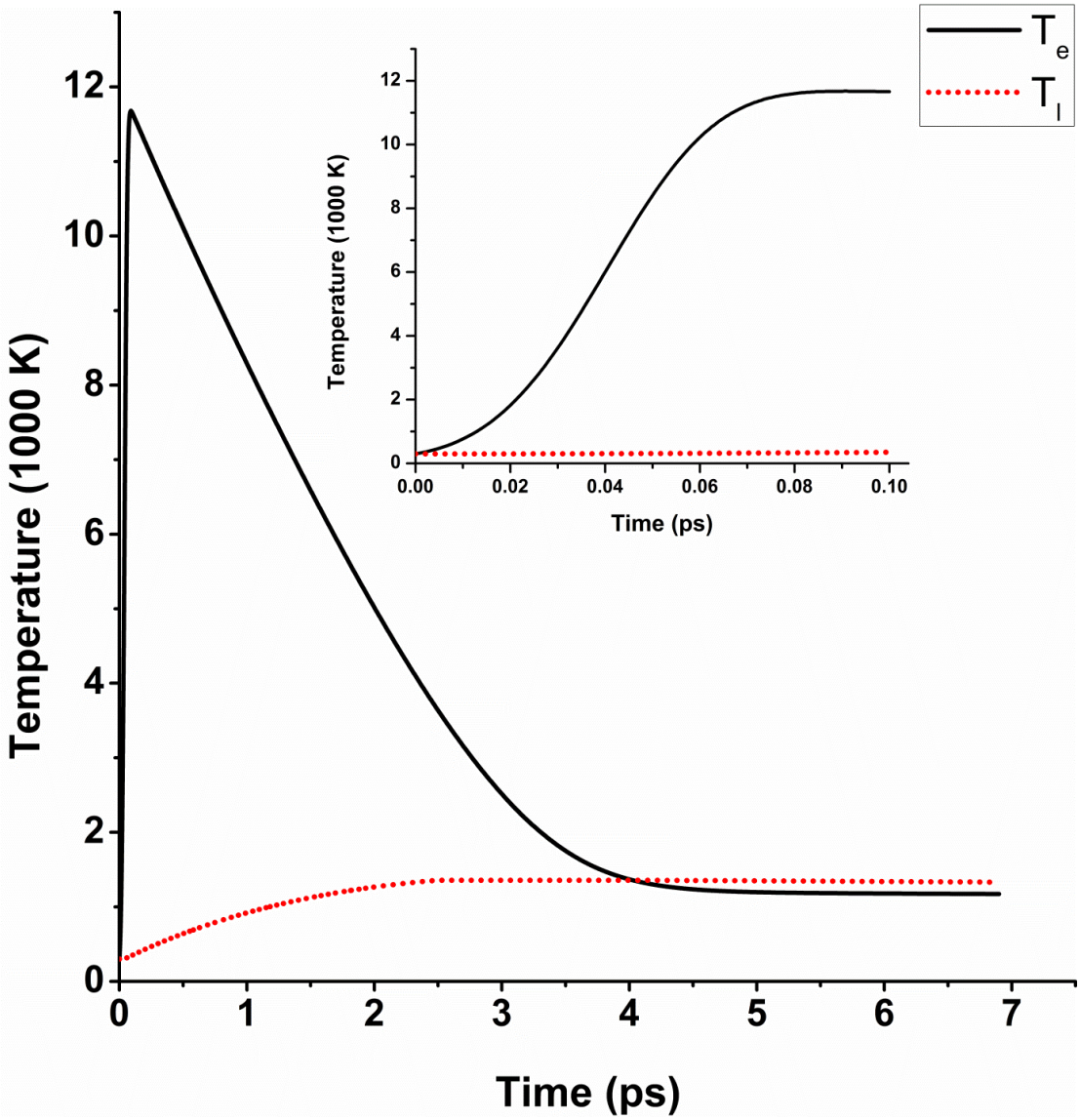

Figure 2.3 Electron and lattice temperatures of copper target at the center heated by laser pulse with pulse width of 100 fs, I_0 of 1.5×10^{13} W/cm^2, and spot radius of 20 μm

However, the decreasing in the electron temperature is much faster than the increasing in the lattice temperature because the rate of electron-electron interaction is higher than the rate of electron phonon interactions (J. B. Lee, Kang, & Lee, 2011). At ~ 4.8 picoseconds the system reaches thermal equilibrium with temperature ~ 1330 K. The

equilibrium distribution of the lattice temperature at the surface as a function of r is shown in figure 2.4. The temperature has its maximum value at the center of the laser beam (r =0) since the maximum power density of the laser is at the center and according to equation 2.7 the temperature decreases gradually till it reaches 300 K which is the assumed initial temperature at ~ 34 μm.

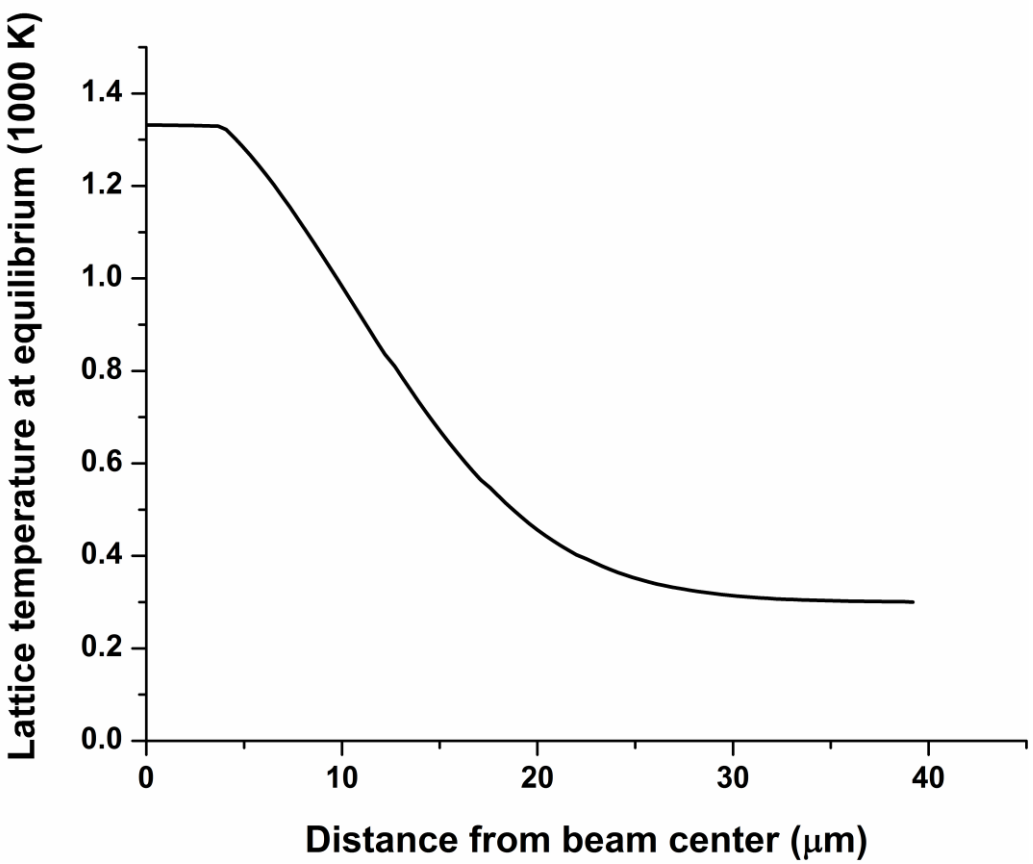

Figure 2.4 Lattice equilibrium temperature at the surface as a function of r heated by laser pulse with pulse width of 100 fs, I_0 of 1.5×10^{13} W/cm^2, and spot radius of 20 μm

Figures 2.5 and 2.6 show the temporal and spatial distribution of the electron temperature at the surface, at fixed location the electron temperature increases until it reaches the maximum, and remains constant to the end of pulse width as shown in figure 2.6. Then the temperature decreases gradually until reaching the thermal equilibrium. On

the other hand, for fixed time the electrons have their maximum value at the center then decreases with r due to the Gaussian distribution of the power density.

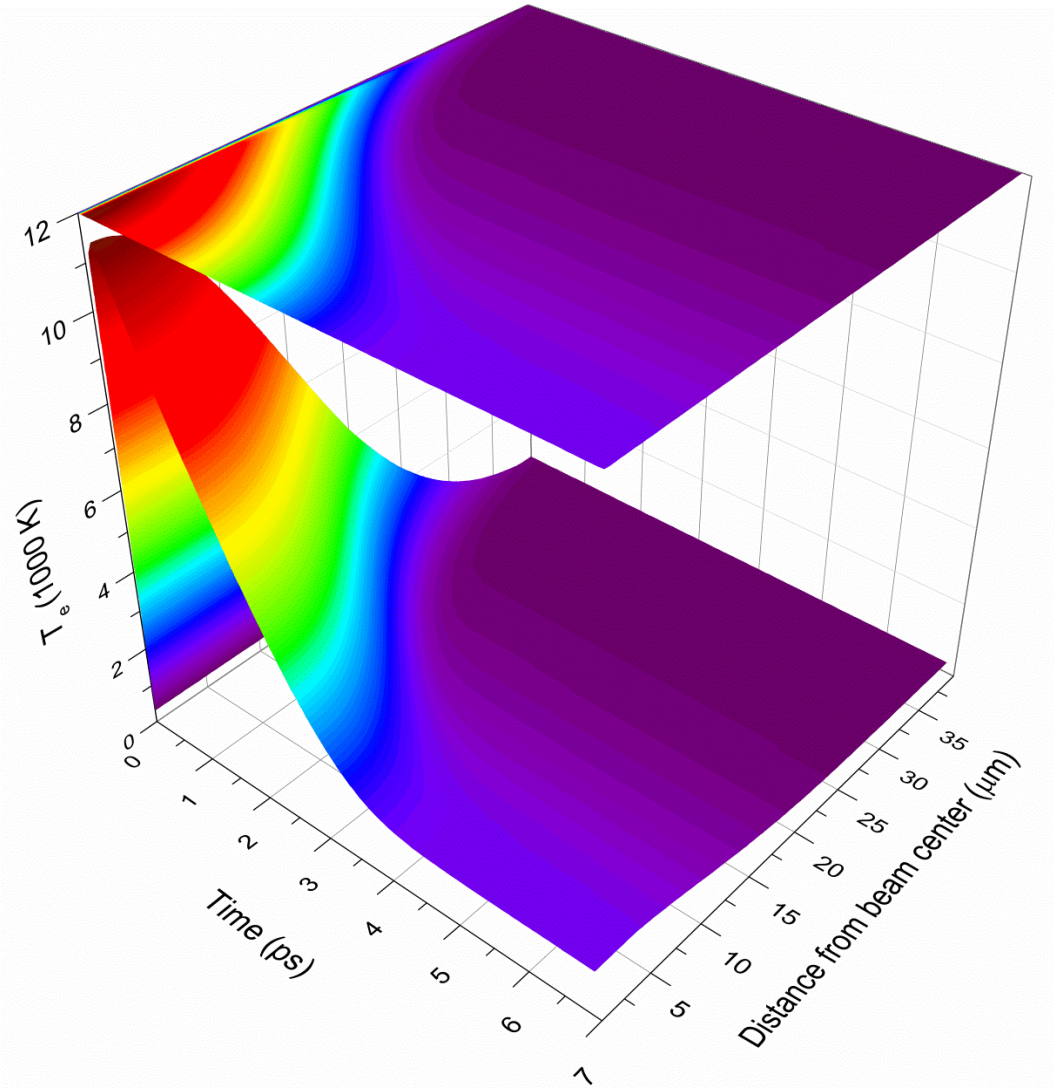

Figure 2.5 Two-dimensional temporal distribution of the electron temperature at the surface as a function of r irradiated by laser pulse with pulse width of 100 fs, I_0 of 1.5×10^{13} W/cm^2, and spot radius of 20 μm

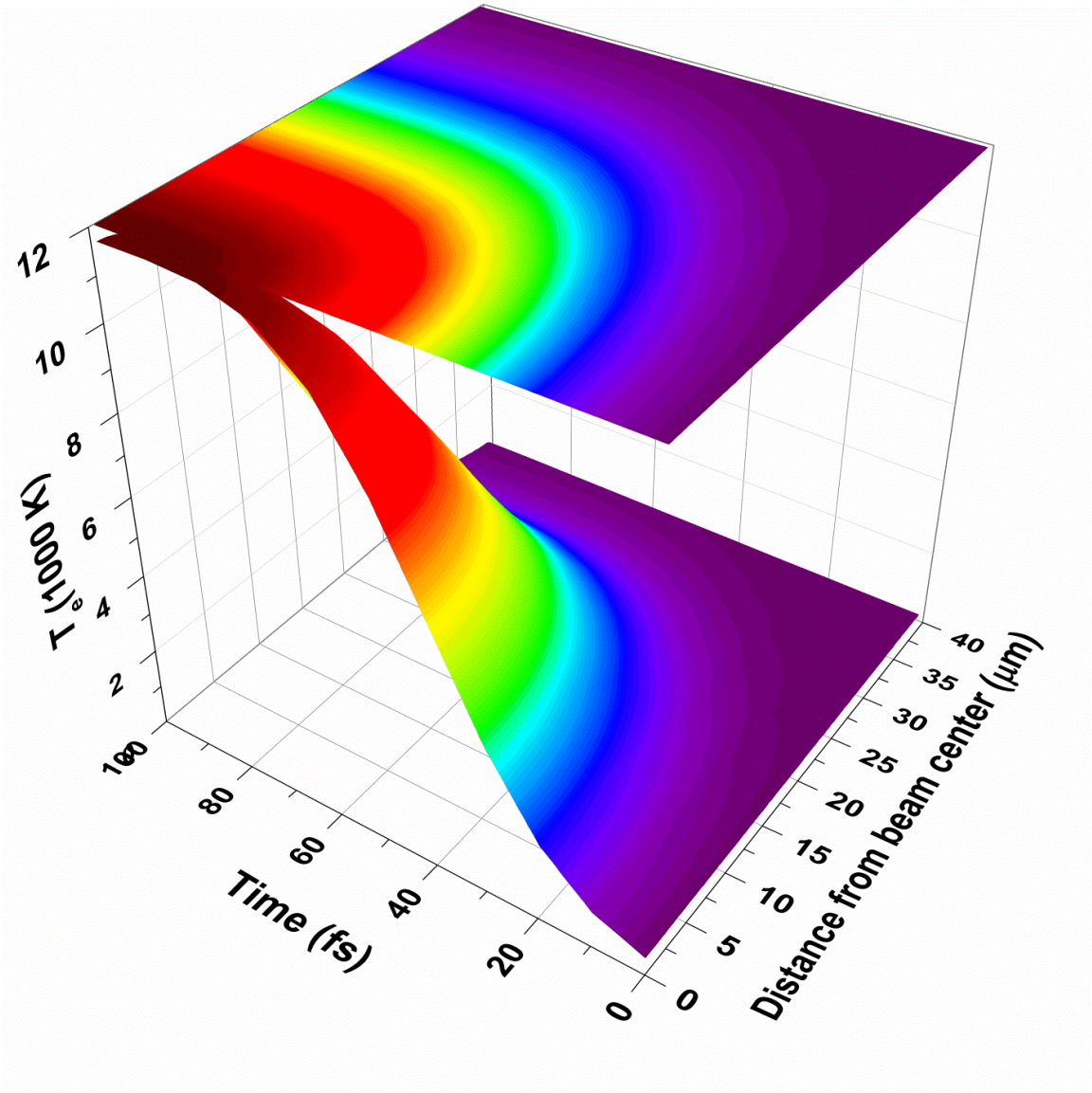

Figure 2.6 Two-dimensional temporal distribution of the electron temperature at the surface as a function of r irradiated by laser pulse with pulse width of 100 fs, I_0 of 1.5×10^{13} W/cm^2, and spot radius of 20 μm

The temporal and spatial distribution of the lattice temperature at the surface is shown in figure 2.7, for fixed location the temperature increases with low rate compared to electrons until reaching the thermal equilibrium and for fixed time the temperature decreases far away from the center as discussed above.

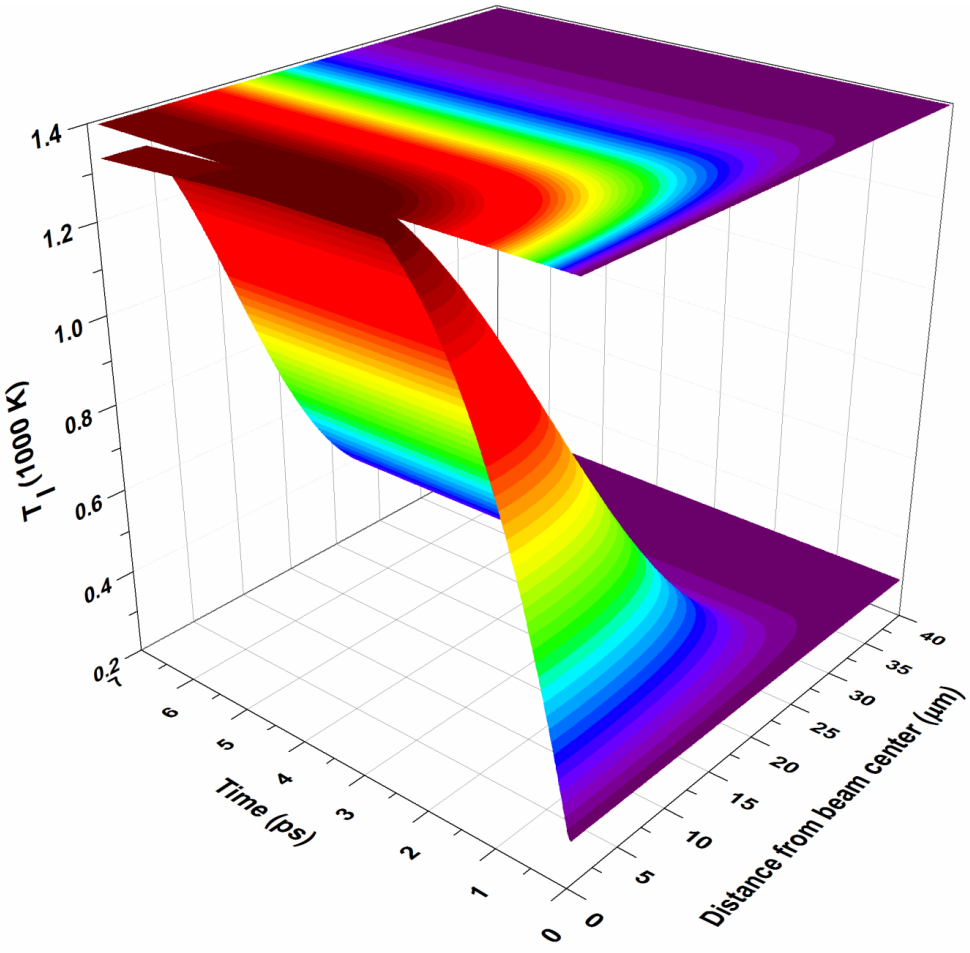

Figure 2.7 Two-dimensional temporal distribution of the lattice temperature at the surface as a function of r irradiated by laser pulse with pulse width of 100 fs, I_0 of 1.5×10^{13} W/cm^2, and spot radius of 20 μm

The electron and lattice temperature distribution in z-direction at the center as a function of time is shown in figures 2.8 and 2.9. The temperature at the center is the maximum and then decreases along with the depth exponentially according to the absorption in z-direction as in equation 2.6. The energy needs longer time to be absorbed inside the material. The behavior of the temporal distribution for both electron and lattice at any point along with depth is the same as discussed before.

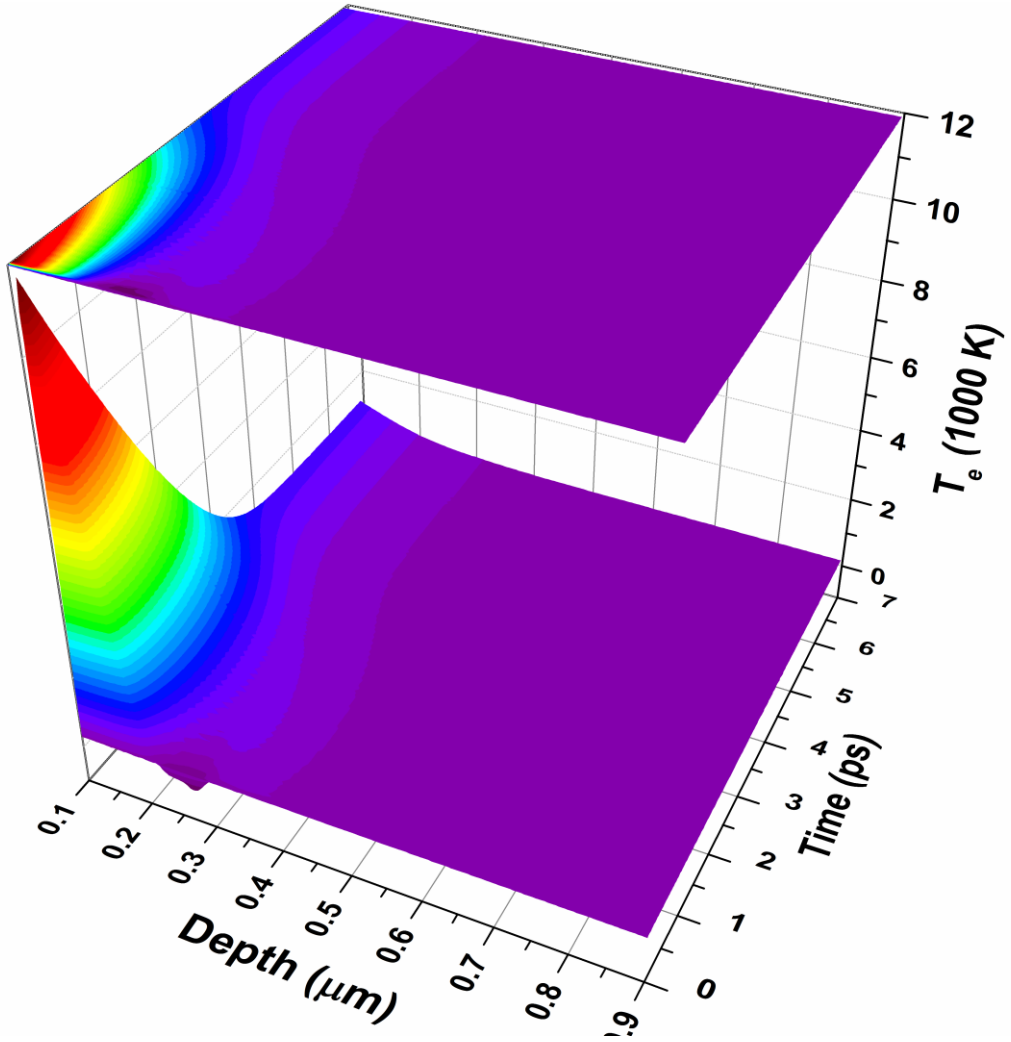

Figure 2.8 Two-dimensional temporal distribution of the electron temperature at the center as a function of z irradiated by laser pulse with pulse width of 100 fs, I_0 of 1.5×10^{13} W/cm^2, and spot radius of 20 μm

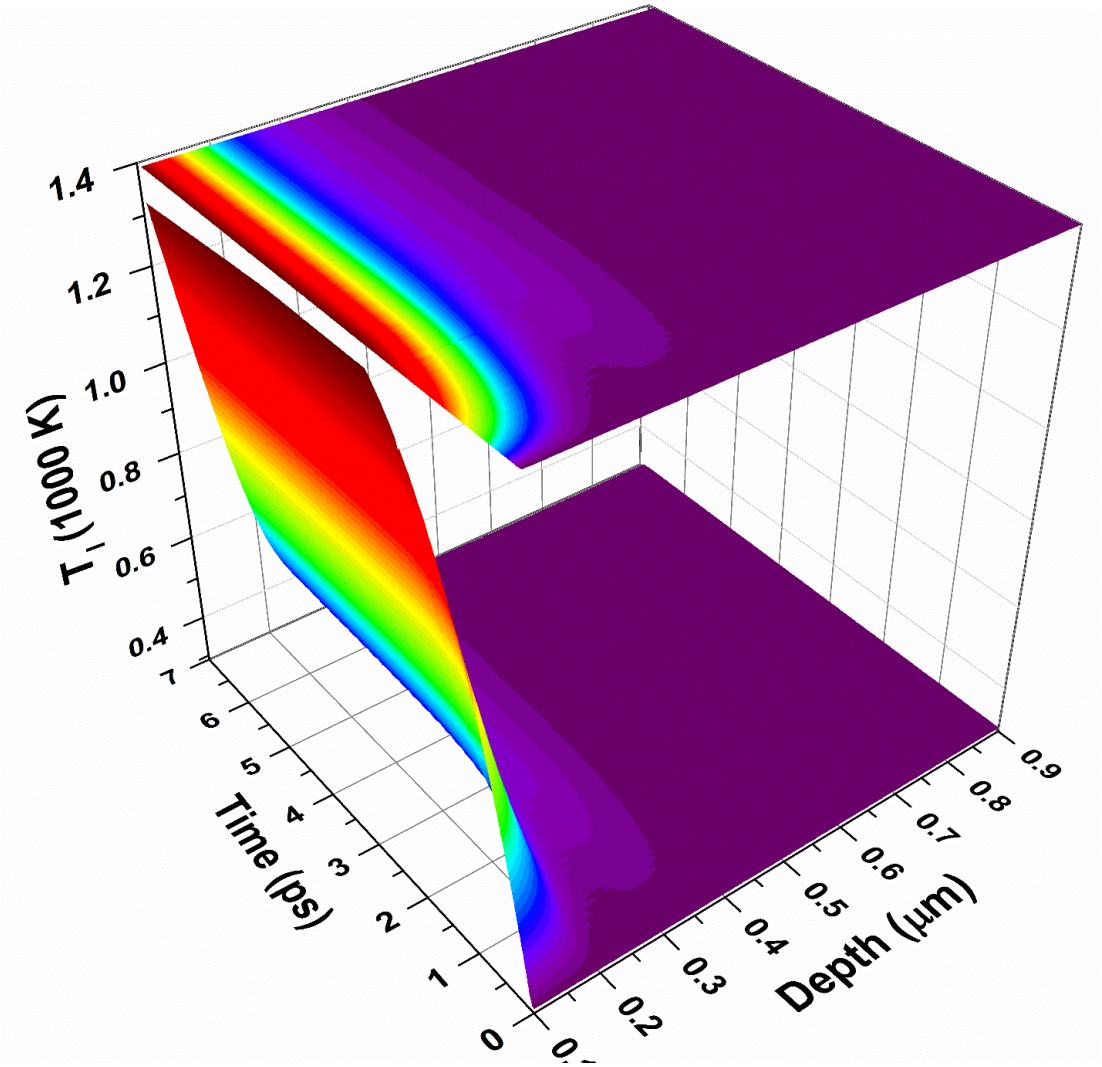

Figure 2.9 Two-dimensional temporal distribution of the lattice temperature at the center as a function of z irradiated by laser pulse with pulse width of 100 fs, I_0 of 1.5×10^{13} W/cm^2, and spot radius of 20 μm

The impact of the spot size of the laser beam on the thermal response of copper target is shown in figure 2.10. As the spot size increases the equilibrium temperature decreases because at the fixed total energy the smaller spot size causes higher power density and more heat is deposited at the surface leading to higher temperature. A 40% reduction in the temperature at equilibrium was observed when the spot size increased by 25%. For

the spot size of 40 μm using equations 2.6, 2.7, and 2.8 the maximal power density is 1.5×10^{13} W/cm^2 and the thermal equilibrium temperature is about 1330K. For spot size of 50 μm the maximum power density is 8.8×10^{12} W/cm^2 and the equilibrium temperature is only 800 K. On the other hand smaller spot size causes less heat dissipated in r-direction.

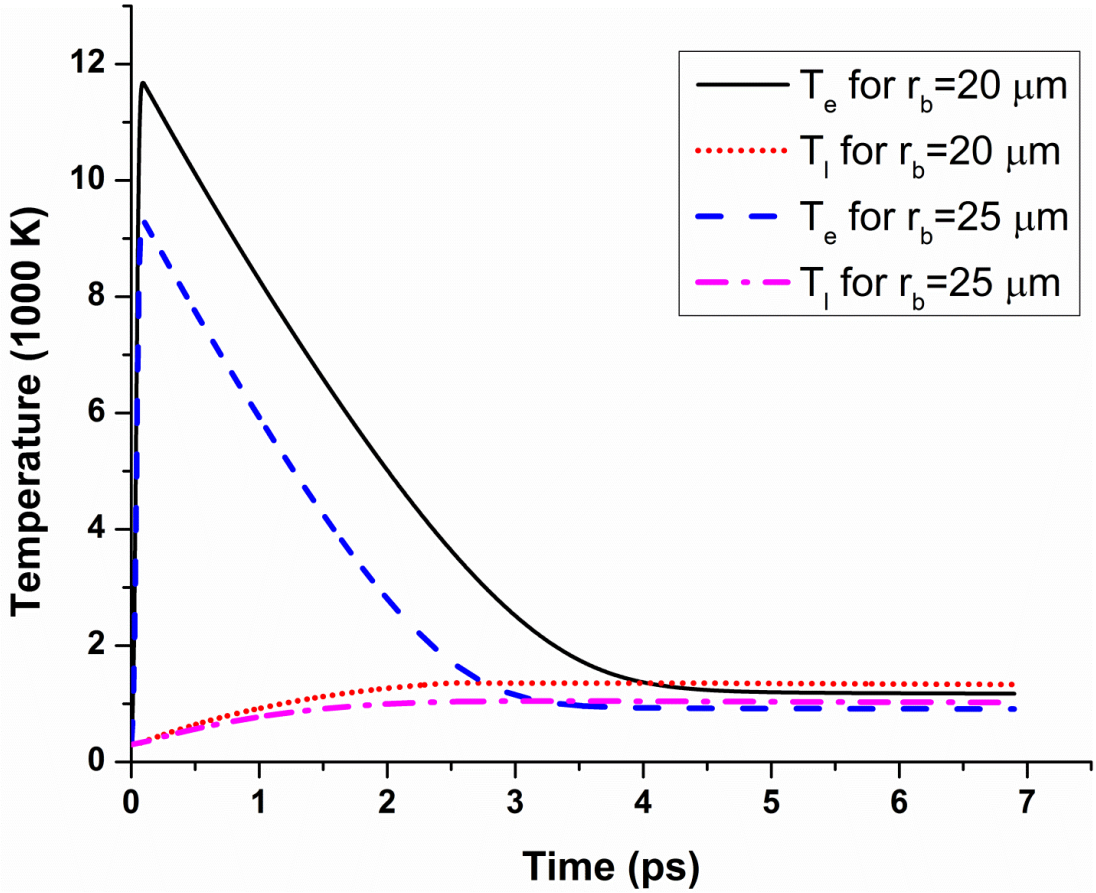

Figure 2.10 Electron and lattice temperatures at the center irradiated by laser pulse with pulse width of 100 fs, at different values of spot size

Figure 2.11 shows the impact of the electron-phonon coupling factor. When the value of the coupling factor is 2.5×10^{11} W/cm^{3}K the thermal equilibrium between the electron and lattice occurs at ~ 4.8 ps, whereas when its value is 5×10^{11} W/cm^{3}K the equilibrium occurs at ~ 2.6 ps. The higher value of coupling factor increases the rate of the electron

phonon interaction such that the thermal equilibrium occurs earlier. Therefore, doubling the coupling factor resulted in reducing the equilibrium time by a factor of 1.8.

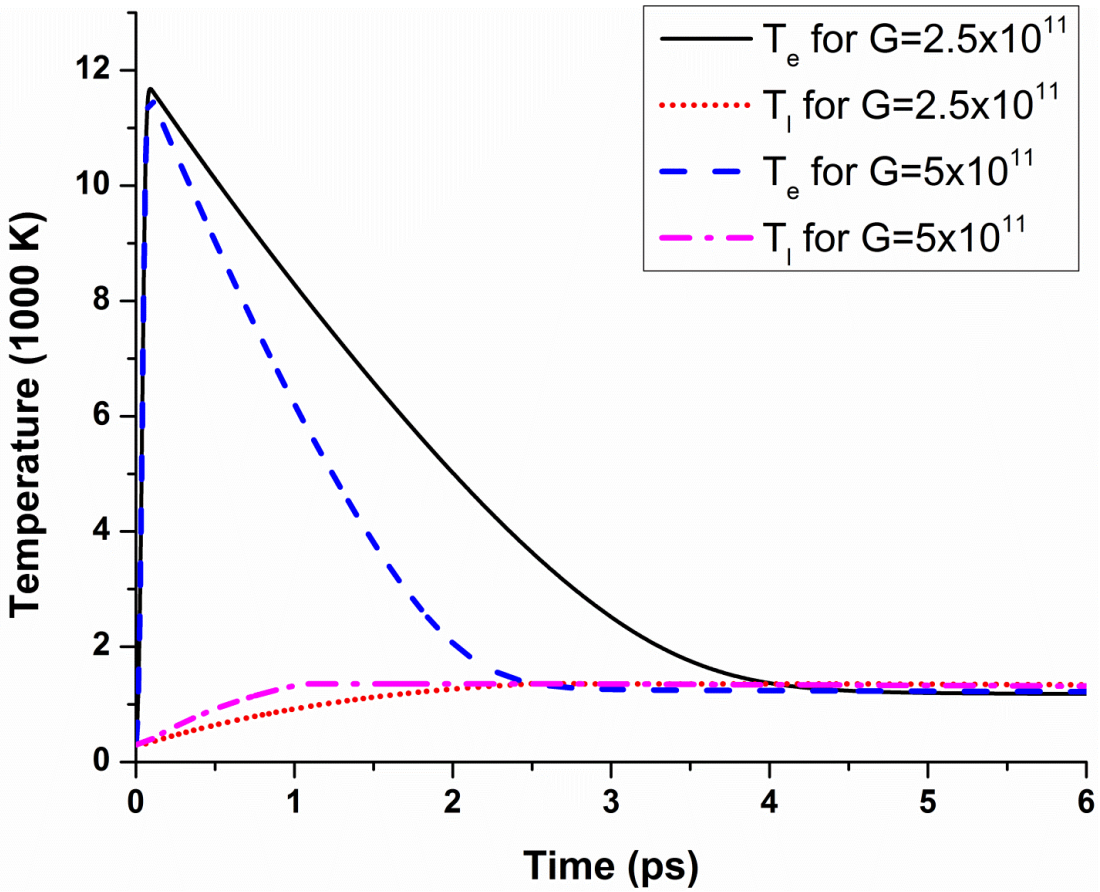

Figure 2.11 Electron and lattice temperatures at the center irradiated by laser pulse with pulse width of 100 fs, I_0 of 1.5×10^{13} W/cm^2, and spot radius of 20 μm at different values of electron-phonon coupling factor

The final parameter studied was surface laser reflectivity, which is shown in Figure 2.12. For the Cu reflectivity of 0.94, the maximum electron temperature is ~ 11700 and the equilibrium lattice temperature is 1330 K. Whereas for a reflectivity of 0.85 the maximum electron temperature is ~ 18500 K and the equilibrium temperature is ~ 2700 K, this is because as the reflectivity increases more photons from the input laser are reflected which leads to less laser power deposited on the surface.

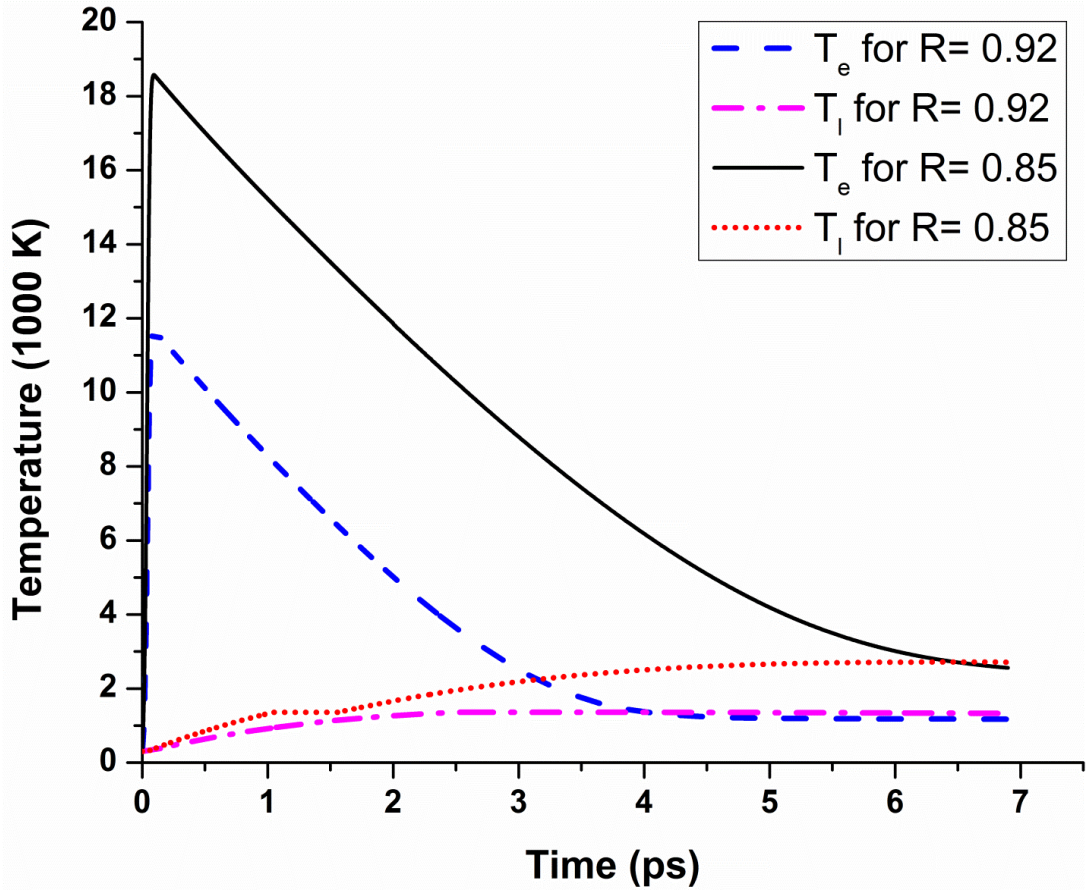

Figure 2.12 Electron and lattice temperatures at the center irradiated by laser pulse with pulse width of 100 fs, I_0 of 1.5×10^{13} W/cm^2, and spot radius of 20 μm at different values of reflectivity

In this case, a 10% decrease in target surface reflectivity increased the equilibrium temperature by a factor of 2. This is in contrast to nanosecond laser pulses where the reflected laser light will be absorbed in the evolving plasma of the target materials and additionally heating such plasma that can further contribute to erosion of target materials.

Conclusion

The work presented in this chapter describes a two-step temperature model that was developed and used to study the non-equilibrium thermal in two-dimensional heat

distribution when copper target is irradiated by femtosecond laser pulse with temperature dependent thermal properties. Gaussian temporal and spatial distributions of laser power density were assumed in our simulation. The predicted behavior of the temperature distribution of the electron and the lattice as a function of t, r, and z was explained by the physics of the heat exchange mechanisms among electrons, photons, and lattice atoms. The electrons initially absorb the laser photons and their temperature increases rapidly to maximum value then remains constant to the end of the femtosecond pulse. Then the heat is transferred to other electrons and phonons, such that the electron temperature decreases and the lattice temperature increases till reaching thermal equilibrium. The impact of the spot size of the femtosecond laser beam was also studied, and the larger spot size for a fixed total energy leads to smaller maximum power density so less heat deposited to the material and finally lower equilibrium temperature. The coupling factor has an important impact on the rate of interaction between the electrons and the lattice, higher values causes higher rate of interaction and faster thermal equilibrium. Finally, the effect of laser reflectivity was studied, and that higher value of reflectivity leads to high rate of photons reflection and less absorption of the energy in the target.

CHAPTER THREE: METAL ABLATION UNDER IRRADIATION BY ULTRASHORT LASER PULSES

Introduction

The ablation of metals means ejection of the material from the surface or the bulk of the metal due to the influence of the intense power deposited in a short period of time that may cause melting, evaporation, spallation, etc. The ablation of metals under the ultrashort laser pulses (picosecond or femtosecond) may have some significant advantages, for example, compared to longer pulse width of nanosecond or millisecond pulses because of the minimum heat-affected zone and the precise and clean ablation that helps to use in different applications that required high precision such as material science, medicine, industry, etc. (Bulgakovaa & Bourakov, 2002; Changrui & Chowdhury, 2004; Ho, Shih, Hung, Ma, & Lin, 2012; Ihtesham, Chowdhury, et al., 2003; Ihtesham, Xianfan, et al., 2003; Kim & Na, 2007; Oh, et al., 2007; Wu & Shin, 2007; Xu, Cheng, & Chowdhury, 2004)

There are many investigations in which the ablation of materials under the ultrashort laser pulses was studied by performing experiments as well as by computer simulations (Colombier, et al., 2005; E. Gamaly et al., 2005; Ihtesham, Xianfan, et al., 2003; Kim & Na, 2007; Oh, et al., 2007) . In the theoretical studies different ablation models and mechanisms were used to estimate the ablation depth by numerically solving the heat

conduction equations in the two-temperature model (Bulgakovaa & Bourakov, 2002; Changrui & Chowdhury, 2004; Ho, et al., 2012; Ihtesham, Chowdhury, et al., 2003; Ihtesham, Xianfan, et al., 2003; Kim & Na, 2007; Oh, et al., 2007; Wu & Shin, 2007; Xu, et al., 2004), use of molecular dynamics, and Monte Carlo methods (Hirayama & Obara, 2005; Lorazo, et al., 2003; Nedialkov, et al., 2005; Xu, et al., 2004; Zhigilei, et al., 2009). The mechanism of the ablation for the ultrashort laser pulses depends on the conditions of the pulse: fluence, pulse width duration, and also on the material itself. Different mechanisms are proposed in the literature for the ablation such as the thermal evaporation (Jiang & Tsai, 2007), normal boiling which is not applicable for the ultrashort laser ablation because of this slow process compared to pulse duration, phase explosion (Bulgakovaa & Bourakov, 2002; Changrui & Chowdhury, 2004; J. K. Chen & Beraun, 2003; Jiang & Tsai, 2007; Kelly & Miotello, 1996; Kim & Na, 2007; Lorazo, et al., 2003; Nedialkov, et al., 2005; Oh, et al., 2007), phase separation (Wu & Shin, 2007), fragmentation (Lewis & Perez, 2009; Lorazo, et al., 2003; Nedialkov, et al., 2005), and spallation (Lewis & Perez, 2009; Nedialkov, et al., 2005; Zhigilei, et al., 2009). Next paragraph will briefly summarize the work done for the ablation by ultrashort laser.

Komashko et al. (1999) model was based on the wave propagation and plasma hydrodynamics for the ablation, taking into account the beam polarization and the incident angle for the ultrashort laser beam at different conditions of pulse duration, fluence, and pre-pulses to estimate the absorption and the ablation of aluminum. The extended two-temperature model was used by Afanasiev et al. (2000) in which they considered the hydrodynamic plasma expansion and the electron degeneracy, they

estimated the ablation depth of copper and gold and they have achieved a good agreement between their own results and the experimental results. Gamaly et al. (2002) solved the heat transfer equations analytically based on some assumptions and introduced a formula to calculate the ablation depth as a function of ablation threshold and the optical and heat diffusion lengths. Sch¨afer et al. (2002) estimated the ablation rate of copper by using a hybrid finite-difference and molecular dynamics. Chen and Beraun (2003) suggested an enthalpy model from the two-temperature equations to estimate the superheating and ablation of material according to phase explosion mechanism, they verified their work by performing a comparison between their results and experimental data. Loranzo et al. (2003) studied the transition from phase explosion mechanism to the fragmentation for the ablation of silicon using Monte Carlo and molecular dynamic analysis for fluences near the threshold. He found that the phase explosion is dominant for the ultrafast heating in femtosecond ranges while the main ablation mechanism for slower heating in picosecond range is the fragmentation. Critical-point phase separation (CPPS) was used as a dominant mechanism for ultrashort high fluence laser in hydrodynamic simulations by Vidal et al. (2001) and molecular dynamic simulations by Xu et al. (2004) in which they found also that the phase explosion mechanism illustrates the ablation of material at low values of fluence. Jiang and Tsai (2007) used thermal evaporation model and the coulomb explosion for the wide gap materials.

In this chapter the parabolic form of the two-temperature model was used to calculate the heat evolution through the irradiated material. The thermal evaporation model and the phase explosion mechanism were implemented to estimate the ablated mass and the crater shape at different conditions.

The Heat Absorption Model

Due to very short pulse of the laser, which is shorter than the time needed to reach the equilibrium between the electrons and the phonons, different mechanism was used for the energy absorption. Two-step temperature model in parabolic form was suggested by Anisimov et al. (1974) in which the material is treated as two systems, i.e., the electronic system and the lattice system. The electrons absorb the photons spontaneously which causes sudden increase in the electron temperature then it reached a constant value to the end of the pulse width at which the equilibrium between electrons is reached, then the electrons start to transfer the energy to the lattice system that causes decrease in the electron temperature and increase in the lattice temperature till the two temperatures reach almost the same value in ~ 4-10 ps of time. Finally, the lattice system reaches the equilibrium. The effect of the electron and lattice relaxation times was added to the model of Chen et al. (2003) that has the hyperbolic form in the following equations:

$$C_e(T_e)\frac{\partial T_e}{\partial t} = \nabla.(Q_e) - G(T_e - T_l) + S \tag{3.1}$$

$$\tau_e \frac{\partial Q_e}{\partial t} + Q_e = -K_e \nabla(T_e) \tag{3.2}$$

$$C_l(T_l)\frac{\partial T_l}{\partial t} = \nabla.(Q_l) + G(T_e - T_l) \tag{3.3}$$

$$\tau_l \frac{\partial Q_l}{\partial t} + Q_l = -K_l \nabla(T_l) \tag{3.4}$$

where τ_e and τ_l is the time for the electrons system and the lattice system to reach the equilibrium respectively. Again, T is the temperature, t is the time, C is the volumetric specific heat, K is the thermal conductivity, where the subscripts e and l are associated with the electron and lattice respectively, G is the coupling factor that describes the

interaction between the electrons and the lattice, S is the volumetric laser energy deposition rate as a function of space and time. The heat diffusion in the lattice was assumed to be negligible. Compared to the pulse width duration both τ_e and τ_l are very short therefore, the hyperbolic form of the two-step model do converge to the parabolic form as the following:

$$C_e(T_e)\frac{\partial T_e}{\partial t} = \nabla.(K\nabla T_e) - G(T_e - T_l) + S \tag{3.5}$$

$$C_l(T_l)\frac{\partial T_l}{\partial t} = G(T_e - T_l) \tag{3.6}$$

Several publications (Ihtesham, Chowdhury, et al., 2003; Ihtesham, Xianfan, et al., 2003; Kim & Na, 2007; Marla, et al., 2011) have suggested the following form for the temporal distribution for the laser source term:

$$\mathrm{S(r,z,t)} = \mathrm{I_\circ} \times (1 - \mathrm{R}) \times 0.94 \times \left(\exp\left(-2.77 * \left(\frac{\mathrm{t} - 2\mathrm{tp}}{\mathrm{tp}}\right)2\right)\right) \times \exp\left(-.5 * \left(\frac{\mathrm{r}^2}{\sigma 2}\right)\right) \times \exp\left(-\frac{\mathrm{z}}{\alpha}\right) \tag{3.7}$$

where $\mathrm{I_\circ}$ is the maximum heat flux, $\mathrm{t_p}$ is the width at the half maximum of the heat flux. Again R is the reflectivity, r is the radial direction and z is the direction along the depth, and α is the absorption coefficient.

The Laser Ablation Models (Thermal Evaporation and Phase Explosion)

In this work two mechanisms were implemented to estimate target ablation and crater formation, i.e., the thermal evaporation and the phase explosion mechanisms. The following subsections will explain the theory behind these two different mechanisms.

Thermal Evaporation

Despite of the low contribution of the thermal vaporization during the ultrashort laser pulses of the irradiated surface we did include it in our work. The evaporation occurs on the outer surface in connection to the vapor pressure of the material at the calculated surface temperature. The surface evaporation velocity or ablation rate is given by (A. M. Hassanein, 1983)

$$v(r,t) = 5.8 \times 10^{-2} \frac{\sqrt{A}\, P_v\,(T_v)}{\rho_v\,(T_v)\,\sqrt{T_v}} \tag{3.8}$$

$$P_v = P_\circ\, e^{\left(\frac{-L_v}{K_B\, T_v}\right)} \tag{3.9}$$

where A is the molar mass of the target, P_v is the vapor pressure that depends on the temperature and the latent heat of vaporization L_v, T_v is the temperature at the surface, K_B is the Boltzmann constant, $P_\circ$ is the reference pressure, and ρ is the temperature dependent density of the target. The recession velocity was calculated at each time step at each point in the radial direction and then the evaporated thickness was calculated using the following relation:

The ablated thickness = Σ (ablation rate * time step) (3.10)

And then the ablated volume and the corresponding ablated mass were calculated.

Phase Explosion

The phase explosion was first introduced by Martynyuk (1974) for the electric explosion to heat and implode a wire. The phase explosion is considered as the main mechanism during the super heating such as that taking place during the interaction between the materials and the ultrashort laser pulses. The basic image of the phase explosion is the homogeneous bubble nucleation in the bulk of the material which is different from the heterogeneous nucleation that takes place at the surface in the case of slow heating process by the normal boiling which is not applicable in this case (Kelly & Miotello, 1996). The pressure-temperature phase diagram in figure 3.1 can be used to describe the ejection due to phase explosion (Kelly & Miotello, 1996; M. M. Martynyuk, 1993), in the case of slow heating the thermal equilibrium between the liquid metal and saturated vapor is reached at fixed temperature and pressure where the vapor pressure can be calculated using the Clausius-Clapeyron equation at the surface temperature. This process is represented by the binodal line; in this case the evaporation is heterogeneous and occurs at the surface of substance. (Bulgakova & Bulgakov, 2001; M. M. Martynyuk, 1977; M. M. Martynyuk, 1993; Xu & Willis, 2002)

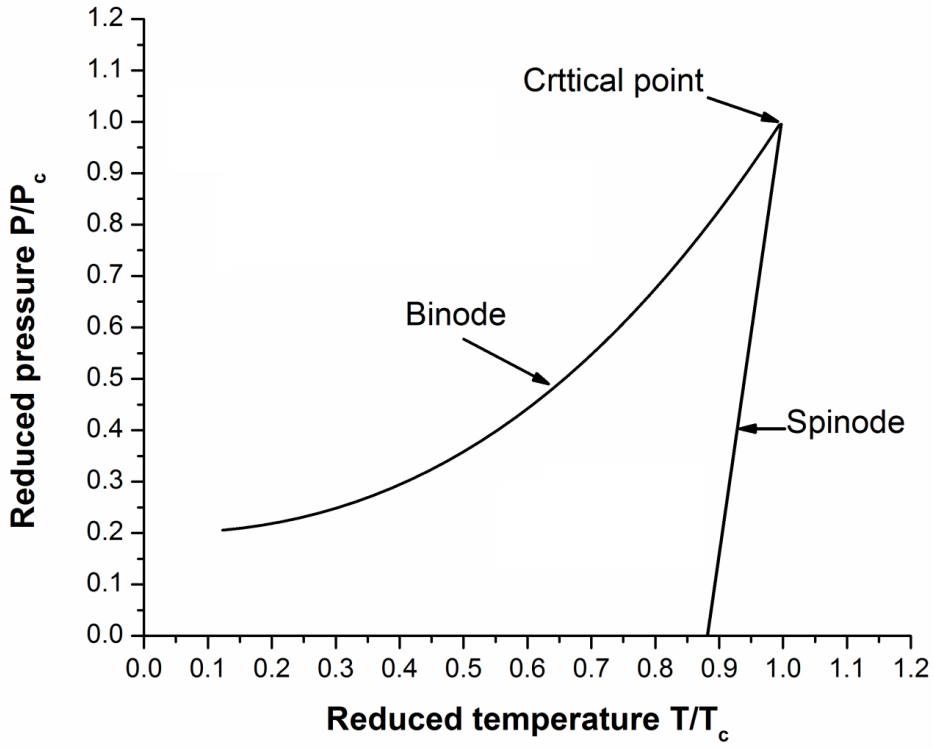

Figure 3.1 Schematic P-T diagram (Shubhrokallol)

The binodal line can be illustrated by assuming that the Gibbs free energy of liquid and vapor are equal (M. M. Martynyuk, 1993):

$G_l(P, T) = G_v(P, T)$ (3.11)

and also with positive values of the second derivatives of the Gibbs energy (stability coefficients) (M. M. Martynyuk, 1993) :

$$(\frac{\partial V}{\partial P})_T > 0 \quad (3.12)$$

$$(\frac{\partial s}{\partial T})_P > 0 \quad (3.13)$$

where T is the temperature, P is the pressure, V is the volume, and s is the entropy.

Now, when the heating is super-fast as in the femtosecond or picosecond laser interaction with material large amount of energy will be absorbed in very short time that causes sudden increase in the temperature. The liquid metal then reached to a temperature greater than the boiling temperature at the same value of surface pressure, which means the liquid becomes superheated. Higher heating rate leads to more approaching to the spinodal line, which is the boundary of thermodynamic phase stability, at which the stability coefficients equal to zero (M. M. Martynyuk, 1977; M. M. Martynyuk, 1993; Xu & Willis, 2002).

$$\left(\frac{\partial P}{\partial V}\right)_T = 0 \tag{3.14}$$

$$\left(\frac{\partial T}{\partial S}\right)_P = 0 \tag{3.15}$$

As the system approaches the region near the thermodynamic equilibrium critical temperature that causes large fluctuation of density and entropy which leads to homogeneous bubbles formation in the bulk of material. The system loose its stability as the nucleation increases and when the bubble size equals the critical size the superheated liquid explode as a mixture of gas and droplets that eject from the bulk of material "Phase explosion" (Bulgakova & Bulgakov, 2001; Kelly & Miotello, 1996; M. M. Martynyuk, 1977; M. M. Martynyuk, 1993; Xu & Willis, 2002).

The ablation depth by the phase explosion mechanism can be calculated by considering that at any point with lattice temperature equals to 0.9Tcr is removed. This factor was suggested in different publications (Bulgakovaa & Bourakov, 2002; J. K. Chen & Beraun, 2003; Kelly & Miotello, 1996; Kim & Na, 2007; Oh, et al., 2007). The

total ablated mass is then the sum of the calculated ablated mass from the thermal vaporization model and that from the phase explosion mechanism.

Method and Input

Several conditions for the ultrashort laser pulse interacting with copper were used (pulse width duration in femtosecond and picosecond ranges, total energy, and spot size). Equations 3.5 and 3.6 with two-dimensional cylindrical coordinate form were solved numerically using the finite difference method to calculate the electron temperature and the lattice temperature at every time step. The physical properties of the material for both the electronic and lattice systems are dependent of the temperature as discussed earlier except for the reflectivity, which is taken as a phase dependent. According to Ren et al. (2011) the thermal response and the resulting electron and lattice temperatures in the case of temperature dependent reflectivity is higher than that for the constant reflectivity at room temperature. They calculated the reflectivity of copper irradiated by ultrashort laser as a function of wavelength and temperature (Ren, Chen, & Zhang, 2011). In this study the phase dependent reflectivity is used and their values were taken from figure 3 of Ref. (Ren, Chen, & Zhang, 2011) at 700 nm. The maximum heat flux in equation 3.7 for fixed value of the total energy of the laser pulse, the spot size, and the pulse duration was calculated using the following relation:

$$\mathrm{E}_{t} = \mathrm{I}_{\circ} \times (1 - \mathrm{R}) \times 0.94 \times \int_{0}^{2tp} \int_{0}^{4\sigma} 2\pi r \exp\left(-.5 * \left(\frac{r^2}{\sigma 2}\right)\right) \times \exp(-2.77 \times \left(\frac{t - 2tp}{tp}\right)^2) \, \mathrm{dr} \, \mathrm{dt} \tag{3.16}$$

After calculating the lattice temperature at the surface, the vapor pressure and the velocity of the receding surface were calculated using equations 3.8 and 3.9 at each time step, and then ablated depth at each point in the radial direction r was calculated according to equation 3.10 so the crater size can be estimated. Following that, the ablated volume was calculated by the relation given by:

The ablated depth at $r_{(i)} = xtot_{(i)}$

The ablated volume $vol_{(i)} = vol_{(i-1)} + xtot_{(i)} \times (\pi r^2_{(i)} - \pi r^2_{(i-1)})$

where i is the cell index in the r-direction.

The ablated mass = density × ablated volume

According to the phase explosion mechanism any point with lattice temperature of $0.9T_{cr}$ is eliminated and considered as ablation depth and is added to the ablation depth from thermal evaporation, where the thermal equilibrium critical temperature of copper is 7696 K (Hess, 1998).

Results and Discussion

The temporal distribution of the laser heat flux at the surface is shown in figure 3.2 for the pulse duration of 50 fs, spot radius of 20 microns and 10-μJ total energy. According to equation 3.7 the temporal absorbed heat flux at the surface has a Gaussian distribution profile with a maximum heat flux of 3.2×10^{13} W/cm^2 and the maximum absorbed heat flux of 1.8×10^{12} W/cm^2 where the difference is reflected from the surface.

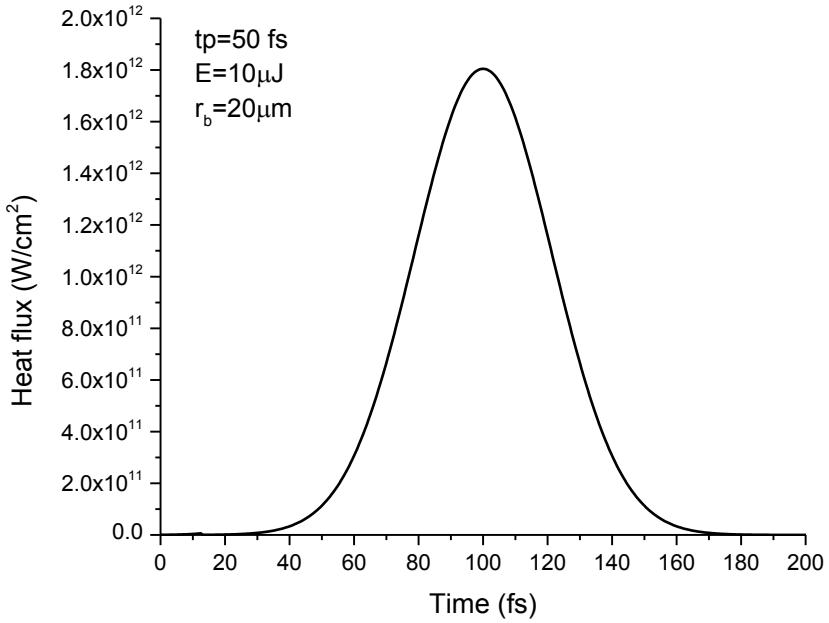

Figure 3.2 Temporal distribution of the absorbed laser heat flux, t_p = 50 fs, r_b = 20 μm, E_t = 10 μJ

The spatial distribution of the heat flux in the radial direction at 50 fs is shown in figure 3.3 where the maximum heat flux is at the center of the laser beam then it decreases exponentially with low values around 20μm which the spot radius of the laser beam.

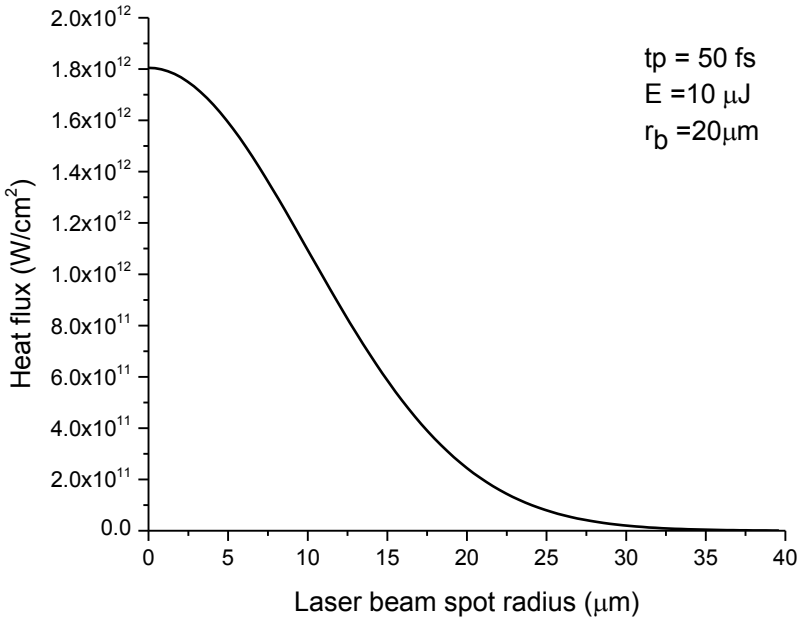

Figure 3.3 Spatial distribution of the absorbed laser heat flux, tp = 50 fs, r_b = 20 μm, E_t = 10 μJ

Figure 3.4 shows the electron and lattice temperature at the surface as a function of time at the same conditions. The electron system absorbs the photons leading to sudden increase in the electron temperature with maximum value of ~ 2.6 eV. The temperature becomes constant when the equilibrium between electrons is achieved at the end of the pulse duration. At that moment the increase in the lattice temperature is negligible. Then the hot electron gas transfers the energy to the cold lattice which causes decrease in the electron temperature and increase in the lattice temperature until an equilibrium between these two systems is reached, then the lattice temperature after equilibrium approaches ~ 0.23 eV at the center.

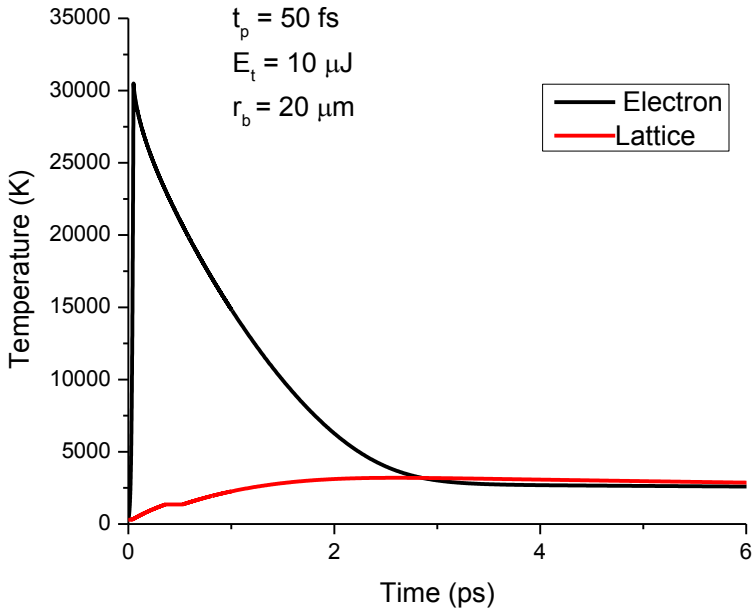

Figure 3.4 Electron and lattice temperature temporal distribution at the surface, t_p = 50 fs, r_b = 20 μm, E_t = 10 μJ

The difference between the ablation based on the thermal evaporation model and on the phase explosion mechanism can be seen in figure 3.5. The black line illustrates the thermal evaporation and the red line is for both mechanisms. The shape of the crater in the case of thermal evaporation is Gaussian and has a much lower contribution on the total material ablation ~ 5 nm compared to the ablation based on the phase explosion concept ~ 50 nm.

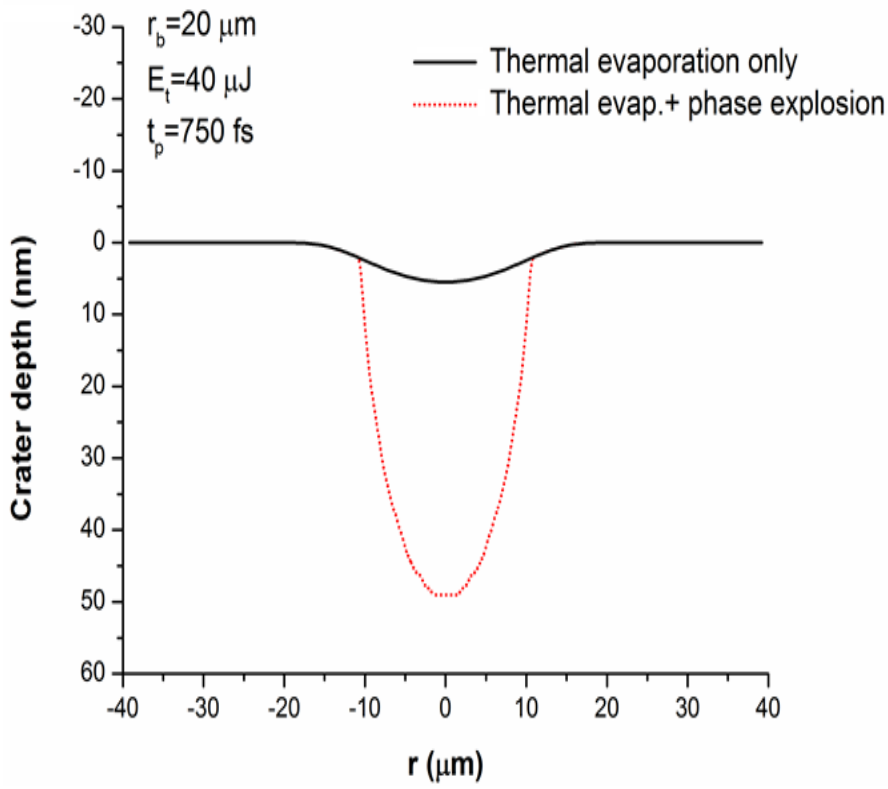

Figure 3.5 Comparison between thermal evaporation model and the phase explosion, t_p = 750 fs, r_b = 20 μm, E_t = 40 μJ

Figure 3.6 shows the crater shape at several values of the total energy for 1 ps laser pulse and 20μm spot radius. Larger values of the total energy lead to higher temperature and higher ablation. For small values of the total deposited energy the crater is smaller and has a smooth shape based on the thermal evaporation model. For the higher total pulse energy the crater is larger and it indicates that the phase explosion is the dominant in the case of high energy.

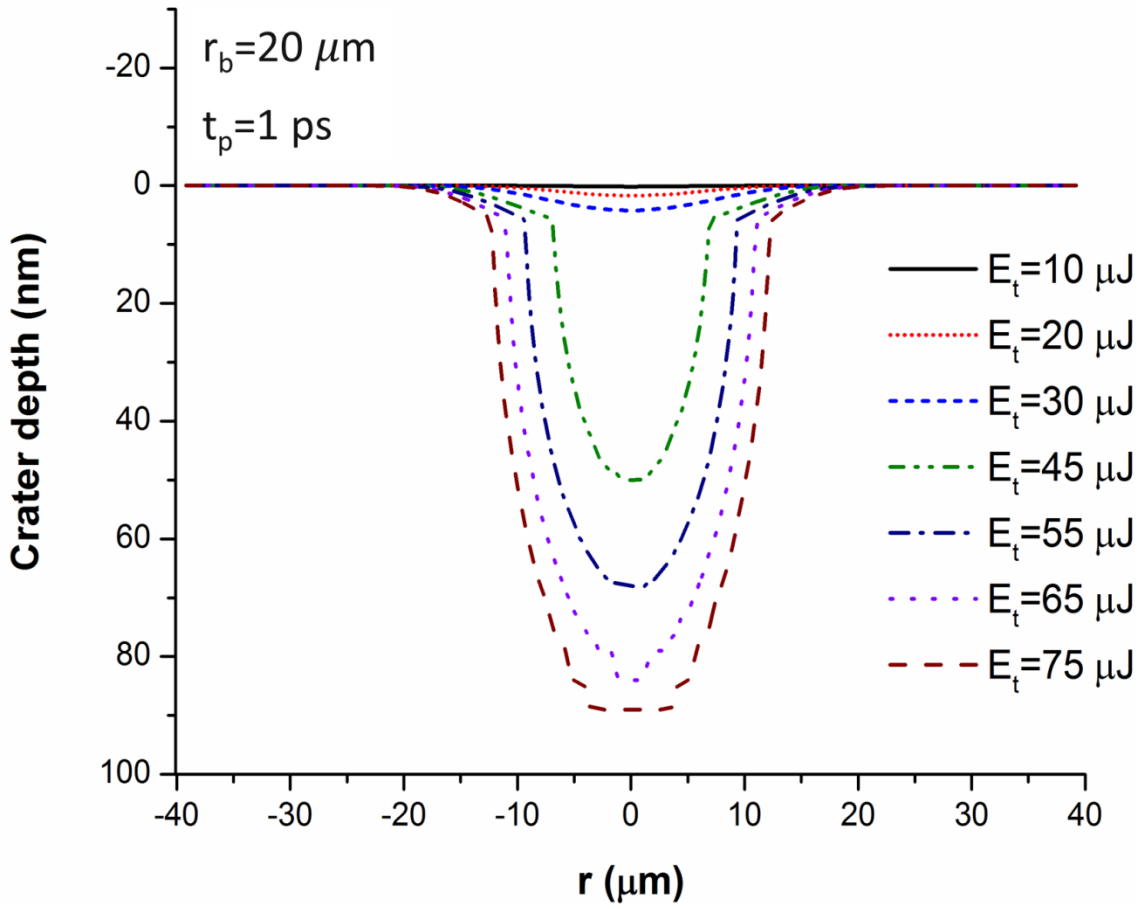

Figure 3.6 Crater shape as a function of total energy of the laser beam, t_p = 1000 fs, r_b = 20 μm

The maximum ablated depth at the center of the laser beam increases significantly as the total energy increases for the same conditions of the laser beam profile and parameters. For example, at 30 μJ the ablated depth is 7 nm whereas at 45 μJ it is ~ 50 nm, as shown in figure 3.7. The corresponding ablated material mass with the same laser conditions was calculated for several values of the total laser energy and also is shown in figure 3.7. It is clear that more energy deposition leads to higher ablated mass.

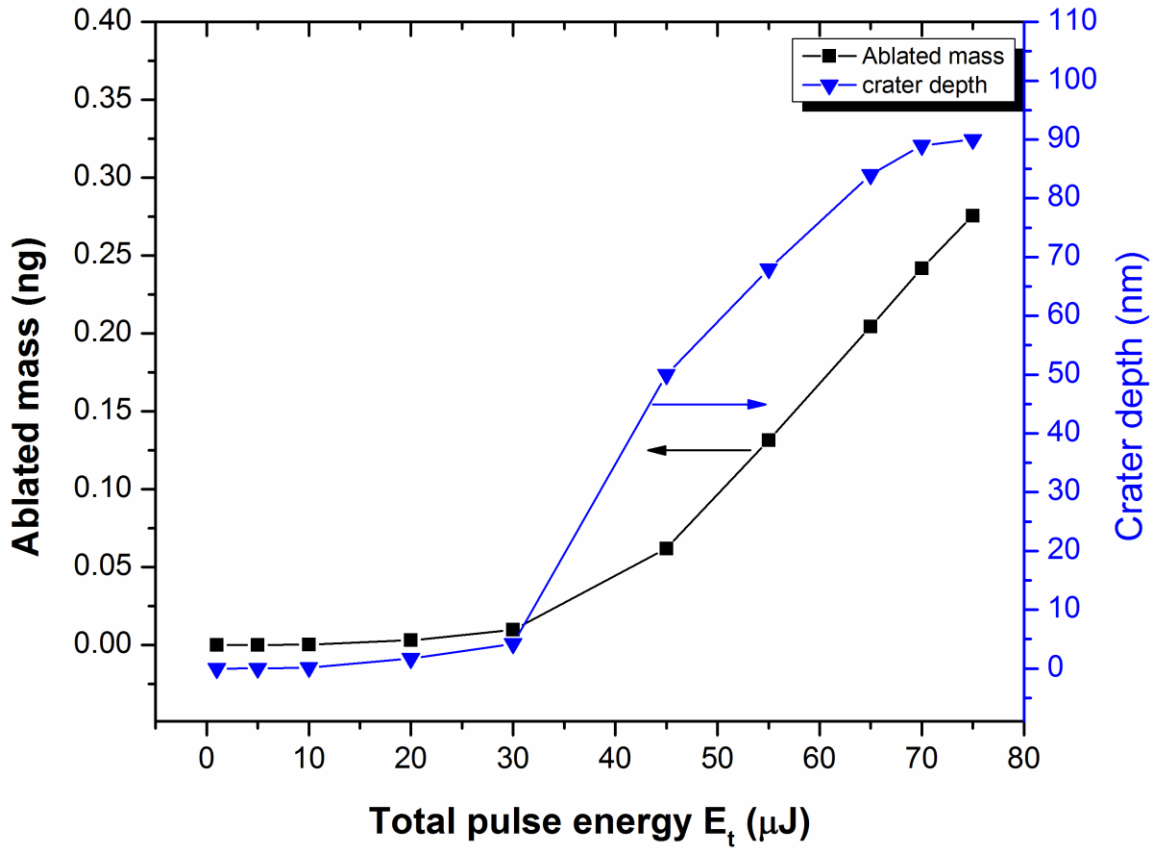

Figure 3.7 Maximum ablated mass and depth as a function of total energy of laser beam, t_p = 1000 fs, r_b = 20 μm

Finally, the impact of the spot radius on the crater shape was studied for 750 fs and 40 μJ laser beam with different spot sizes. Figure 3.8 shows that the larger spot size leads to lower heat flux that causes less ablation, so that the crater depth is shallower. The ablated mass for different values of spot radii was also calculated and shown in Figure 3.9. For spot radius of 20 μm the maximum ablated depth is 48 nm while it is 84nm for the spot radius of 15μm as shown in figure 3.8 the corresponding ablated mass for the same conditions is shown in figure 3.9.

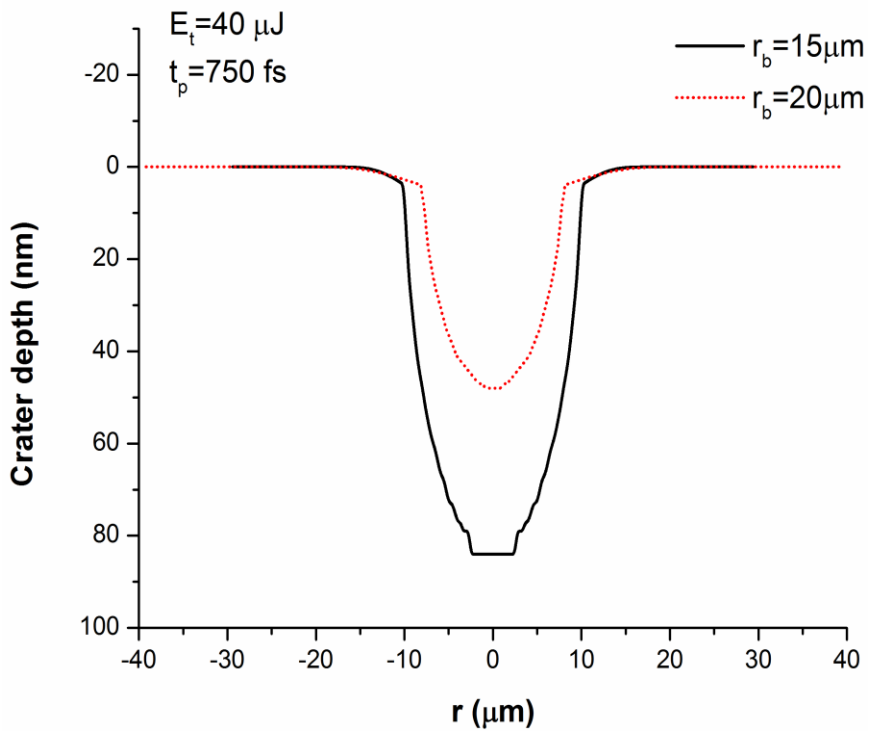

Figure 3.8 Crater shape as a function of spot radius of laser beam, t_p = 750 fs, E_t = 40 μJ

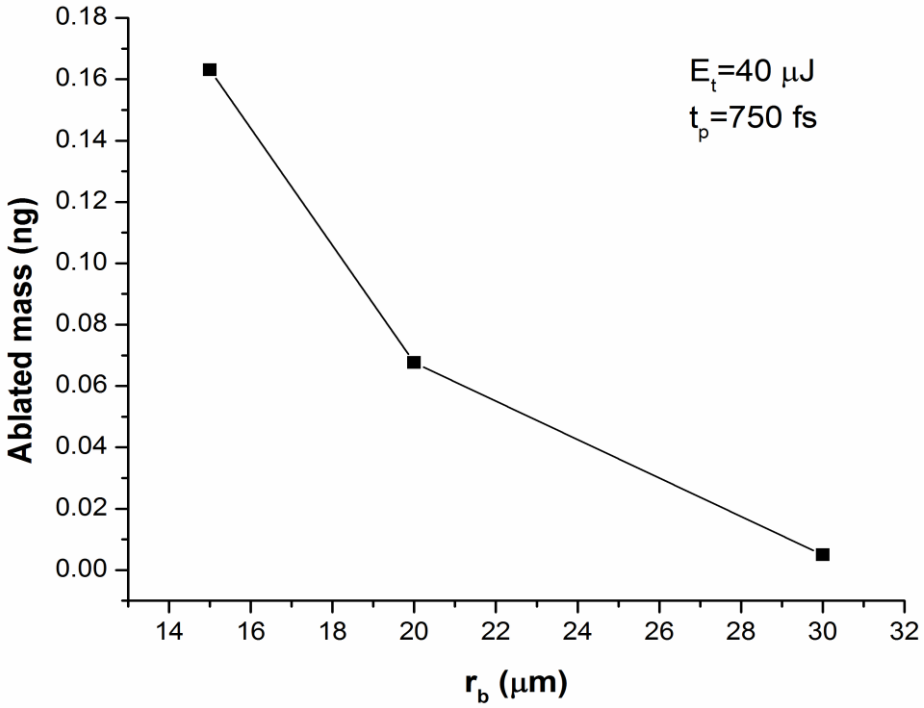

Figure 3.9 Ablated mass as a function of spot radius of laser beam, t_p = 750 fs, E_t = 40 μJ

Conclusion

In this chapter the ablation of copper irradiated by ultrashort laser pulses was studied. The parabolic two-dimensional two-temperature model with temperature dependent material properties was used to predict material behavior during the ultrashort laser beam. The electrons absorb the energy from the photons spontaneously then transfer the energy to the lattice system according to electron-phonon coupling mechanism. Thermal evaporation and phase explosion mechanisms were used to estimate the crater size and the ablated depth and mass. The ablation by the thermal evaporation can be estimated by calculating the surface recession velocity, which is a function of surface temperature, vapor pressure, and the latent heat of vaporization. The phase explosion mechanism, which is considered as the main mechanism for the ultrafast heating was implemented in the model. The liquid phase becomes superheated metastable and the temperature increases suddenly to the value near the spinodal line. As a result the homogenous bubble nucleation starts, which eventually causes explosive ejection of liquid droplets. For this mechanism any target material reaches the temperature of $0.9T_{cr}$ was eliminated and then accounted for the ablation depth. The impact of the total energy and the spot radius on the crater size and ablated mass were studied. It was found that when the total energy increases the maximum ablated depth increases at different rate depending on energy and the mode of ablation that is because higher total energy leads to higher heat absorbed and to higher ablation, also as the spot radius increases the absorbed heat flux decreases causes decrease in the ablation depth.

CHAPTER FOUR: THE IMPACT OF THE MODIFIED ELECTRON-PHONON COUPLING FACTOR AND ELECTRON HEAT CAPACITY ON THE THERMAL RESPONSE OF THE TARGET IRRADIATED BY FEMTOSECOND LASER.

Introduction

The thermal properties of any material of such as heat capacity, thermal conductivity, density, melting and evaporation temperature, latent heat of fusion, and vaporization,… etc., determine its thermal response when it interacts with a heat source. In addition, it was found that the nature of some thermal properties in terms of their dependency on the temperature, phase, or composition will have an important impact on the irradiated material thermal response. When the material is irradiated by ultrashort laser pulses, non-equilibrium heat transfer occurs because of the low heating pulse duration (femtosecond or picosecond) compared to the thermalization time, which leads to deal with two subsystems, electrons and lattice, in the calculations of the thermal evolution through the material target which is described by the two-temperature model (s.I Anisimov & Rethfeld, 1997; Kaganov, Lifshitz, & Tanatarov, 1957). In this case, the thermal properties of electron and lattice subsystems such as thermal conductivity and the heat capacity should be distinguished. Moreover the electron-phonon coupling factor which is responsible for the heat transfer from the electrons subsystem to the phonons subsystem should be selected carefully.

Many studies have been done to investigate the impact of the material thermophysical properties as material and temperature dependent in different models by comparing the results with the case if they were used as constant parameters. Lin et al. (2007; Zhibin Lin, et al., 2008; Phipps, Lin, & Zhigilei, 2006) investigated the dependency of electron temperature and the electron density of state (DOS) on the electron-phonon coupling and electron heat capacity for aluminum, copper, silver, gold, nickel, platinum, tungsten, and titanium. Their results differ from the approximations of using constant electron-phonon coupling factor and linear temperature dependence of the electron heat capacity. They found that the thermal excitation of the electrons depends strongly on the electronic structure of the electron density of state, and thus it has large impact on the thermophysical properties of the metals irradiated by ultrashort laser pulse. As an example, they found that for the noble metals (Au, Cu, and Ag) at very high electron temperature the thermal excitation of the d band electrons contribute to the increasing of the electron heat capacity and electron-phonon coupling, while the opposite result was observed in the case of the transition metal such as Pt. The data of temperature dependent electron heat capacity and the electron-phonon coupling factor for several metals based on their electron density of states and electron thermal excitation are tabulated in ("Electron-Phonon Coupling and Electron Heat Capacity in Metals at High Electron Temperatures,"), which are calculated using Lin's model (Ashcroft & Mermin, 1976; Z Lin & Zhigilei, 2007; Zhibin Lin, et al., 2008), the temperature dependent electron-phonon coupling factor and electron heat capacity data for copper were curve fitted by Ren et al. (2011). J. K. Chen et al. (2005) proposed a mathematical model in which the electron-electron and electron-phonon collision rate determines the electron relaxation.

This model connects the electron and lattice temperatures with the electron-phonon coupling factor; it was used for the gold film irradiated by ultrashort laser pulse (J. K. Chen, et al., 2005). They noticed a decrease in the electron temperature and an increase in the lattice temperature when this model is used compared to the use of constant value of the electron-phonon coupling factor in the two-temperature model. In addition, there was a good agreement between their results and the experimental results for the calculated ablation depth as a function of fluence. A full comparison between three different models was presented by J. Lee et al. (2011) to calculate the temperature dependent electron-phonon coupling factor; Chen's model (J. K. Chen, et al., 2005), Lin's model (Z Lin & Zhigilei, 2007; Zhibin Lin, et al., 2008) and Kaganov's model (Kaganov, et al., 1957) They compared their results with the commonly used constant value of electron-phonon coupling factor for gold. They found a good agreement among all the models at low temperature and there was a clear deviation at high temperature. Moreover, it was found that Lin's model is the most acceptable one to predict the electron-phonon coupling in the target irradiated by ultrashort laser pulse.

Mathematical Equations

Electron-Phonon Coupling Factor

The energy transport from the electrons to the lattice during the non-equilibrium heat transfer calculations was introduced by Anisimov et al. (1974) with a relation of the electron-phonon coupling factor of:

$$G = \frac{\pi^2}{6} \frac{m_e V_s^2 n_e}{\tau_e (T_{e)} T_e} \tag{4.1}$$

where, m_e is the effective electron mass, V_s is the speed of sound, n_e is the number density of electrons, τ_e is the electron relaxation time, and T_e is the electron temperature. Since $\tau_e \sim T_e^{-1}$ as suggested by Anisimov (1974) the coupling factor in this equation becomes independent of the electron temperature. For high electron and lattice temperature away from Debye temperature the electron-phonon coupling factor was suggested by Kaganov et al. (1957) by assuming the free electron of metals by the Debye phonon approximation (Kaganov, et al., 1957; J. B. Lee, et al., 2011):

$$G = \frac{\pi^2}{6} \frac{m_e V_s^2 n_e}{\tau_l (T_l) T_l} \qquad T_l \gg T_D\,;\ (T_e - T_l) \ll T_l \tag{4.2}$$

$$G = \frac{\pi^2}{6} \frac{m_e V_s^2 n_e}{\tau_e (T_e)\,(T_e - T_l)} \qquad T_e \gg T_D\,;\ T_l \ll T_e \tag{4.3}$$

where, T_D is the Debye temperature and τ_l is the lattice relaxation time as a function of the lattice temperature. Again, it was found that the dependency of the electron or lattice temperature on the electron-phonon coupling factor using these equations is negligible (J. B. Lee, et al., 2011).

The theoretical model that is suggested by J. k. Chen et al. (2005) for T_e and $T_l >> T_D$, to calculate the temperature dependent electron-phonon coupling factor is in the following form (s.I Anisimov & Rethfeld, 1997; J. K. Chen, et al., 2005):

$$G = G_{RT} \left[\frac{A_e}{B_l} (T_e + T_l) + 1 \right] \tag{4.4}$$

$$G_{RT} = \pi^2 \frac{m_e V_s^2 n_e B_l}{6} \quad (4.5)$$

where, $A_e = (v_{e0} T_f^{\,2})^{-1}$ and $B_l = (v_{p0} T_f)^{-1}$ with v_{e0} and v_{p0} are material constants that are related to the electron-electron collision and electron-lattice collision, and T_F is the Fermi temperature. For copper, A_e and B_l are 1.28×10^7 $s^{-1}K^{-2}$ and 1.23×10^{11} $s^{-1}K^{-1}$ respectively (F. Chen, Du, Yang, Si, & Hou, 2011). At room temperature the coupling factor reduced to G_{RT} (J. K. Chen, et al., 2005).

The last model was introduced by Lin's et al. (Z Lin & Zhigilei, 2007; Zhibin Lin, et al., 2008) based on the variations of the electronic structure of metals of the electron density of state at high electron temperature:

$$G = \frac{\pi \hbar K_B \lambda \langle \omega^2 \rangle}{g(\varepsilon_F)} \int_{-\infty}^{\infty} g^2(\varepsilon) \left(-\frac{\partial f}{\partial \varepsilon} \right) d\varepsilon \quad (4.6)$$

where, ħ is the reduced Planck constant, k_B is the Boltzmann constant, $\langle \omega^2 \rangle$ is the second moment of the phonon spectrum defined by McMillan (McMillan, 1968), λ is the electron-phonon mass enhancement parameter (Grimvall 1976), g(ε) is the electron DOS at the energy level ε, and $f(\varepsilon, \mu, T_e)$ is the Fermi distribution function with μ being the chemical potential (Z Lin & Zhigilei, 2007; Zhibin Lin, et al., 2008). The data of electron-phonon coupling as a function of electron temperature from this relation for copper were fitted by Ren et al. (2011) with the following corresponding function, where G is in $Wm^{-3}K^{-1}$:

$$G\ (T_e) = \begin{cases} 0.56\ \times\ 10^{17}, & T_e\ < 2750\ K \\ 1.341\ \times 10^{17} - \ 1.407\ \times 10^{14} T_e\ +\ 5.988\ \times 10^{10} T_e^2\ -\ 7.93\ \times 10^{6} T_e^3 & \\ \quad + 555.2 T_e^4 - 0.023272 T_e^5 + \ 6.041 \times 10^{-7} T_e^6\ -\ 9.529\ \times 10^{-12} T_e^7 & \\ + 8.377 \times 10^{-17} T_e^8\ -\ 3.15\ \times 10^{-22} T_e^9, & 2750\ K \le T_e \le 50 \times\ 10^3\ K \end{cases} \quad (4.7)$$

Electron Heat Capacity

When dealing with ultrafast heating, the electron and the lattice heat capacity should be distinguished. The commonly used relation for the electron heat capacity is the linear dependence with the electron temperature (Horng, 1984; J. B. Lee, et al., 2011; J. B. Lee & Lee, 2011; Zhibin Lin, et al., 2008; Tien, Majumdar, & Gerner, 1998; Veal & Rayne, 1962):

$$C_e = \ B_e\ T_e \quad (4.8)$$

where $B_e = \pi^2 n_e K_B^2 / 2\varepsilon_F$, but it was found that this relation is only applicable for low electron temperature. Therefore the following equation was suggested to calculate the heat capacity at high electron temperature (Ashcroft & Mermin, 1976; Zhibin Lin, et al., 2008):

$$C_e\ (T_e) = \ \int_{-\infty}^{\infty} \frac{\partial f(\varepsilon, \mu, T_e)}{\partial \varepsilon}\, g(\varepsilon) \varepsilon\ d\varepsilon \quad (4.9)$$

The data of the electron heat capacity in $Jm^{-3}K^{-1}$ as a function of electron temperature for the copper were accurately fitted by Ren et al. in the following function(Ren, Chen, & Zhang, 2011):

$$C_e(T_e) = \begin{cases} 117.47\,T_e, & T_e < 2 \times 10^3\ K \\ -2.049 \times 10^4 - 26.64\,T_e + 0.0996\,T_e^2 - 1.122 \times 10^{-5} T_e^3 \\ +5.735 \times 10^{-10} T_e^4 - 1.524 \times 10^{-14}\,T_e^5 + 2.044 \times 10^{-19} T_e^6 \\ -1.094 \times 10^{-24} T_e^7, & 2 \times 10^3\ K \le T_e \le 50 \times 10^3\ K \end{cases} \quad (4.10)$$

In this chapter, different models of temperature dependent electron-phonon coupling and electron heat capacity of copper irradiated by femtosecond laser pulse were used to investigate the temporal and spatial thermal evolution using the two-temperature model with Gaussian distribution of the laser beam heating source in time and space. Temperature dependent of the electron thermal conductivity and the lattice density and heat capacity were taken into account. For all of the simulations in this chapter the reflectivity of 50% and laser spot size of 40 μm were used. The constant value for the electron-phonon coupling factor was chosen to be 0.56×10^{11} $Wcm^{-3}K^{-1}$ in this chapter.

Results and Discussion

Figure 4.1 shows the dependency of the electron-phonon coupling factor on the electron temperature by using Chen's model in the equation 4.4 which is represented by solid line, and Lin's model by using the data fitted function in equation 4.7 (the dashed line), to compare these two models with the using of constant value for the electron-phonon coupling factor. As can be seen in this figure at low electron temperature the values of the coupling factor are very close in the three cases, but the deviation started with increasing the electron temperate. Lin's model shows the highest value which means

the strength of the heat coupling between the electrons and the lattice is high when we take into account the calculations of the density of state. Next to it the Chen's model which shows also high values of the coupling factor compared to the constant value.

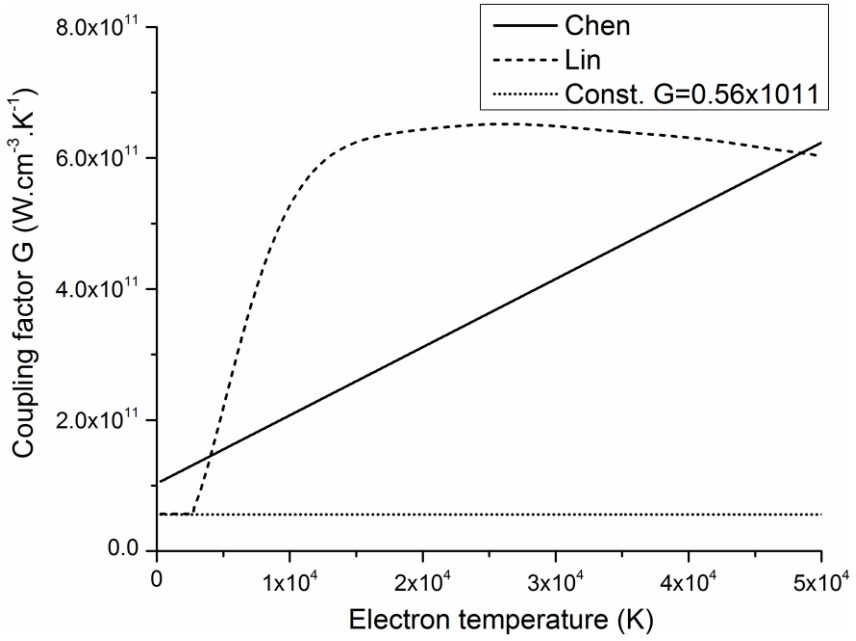

Figure 4.1 Electron-phonon coupling factor of the copper as a function of electron temperature in Chen's model (the solid line), Lin's model (the dashed line), and constant G with a value of 0.56×10^{11} $Wcm^{-3}K^{-1}$ (the dotted line)

The temporal distribution of the surface electron and lattice temperature at the center of the laser beam with pulse duration of 50 fs and fluence of 0.05 J /cm^2 for the three models are presented in figure 4.2, where the top left is for the Lin's model, the top right is for the Chen's model, and the bottom of the figure is for the constant coupling model. As can be seen in this figure the maximum electron temperatures have the same value of 1.27×10^4 K for all of these three cases. It is clear from this figure that the thermalization time which is defined as the time needed for the electron and lattice subsystems to reach the equilibrium is different between the models, for example the lowest thermalization

time was for the Chen's model with the above mentioned laser conditions was ~3.6 ps while it was ~5 ps and ~6 ps for the Lin's model and constant G model respectively. The same results for the comparison between these two model and the constant G for the gold target was achieved by Lee et al. (J. B. Lee, et al., 2011).

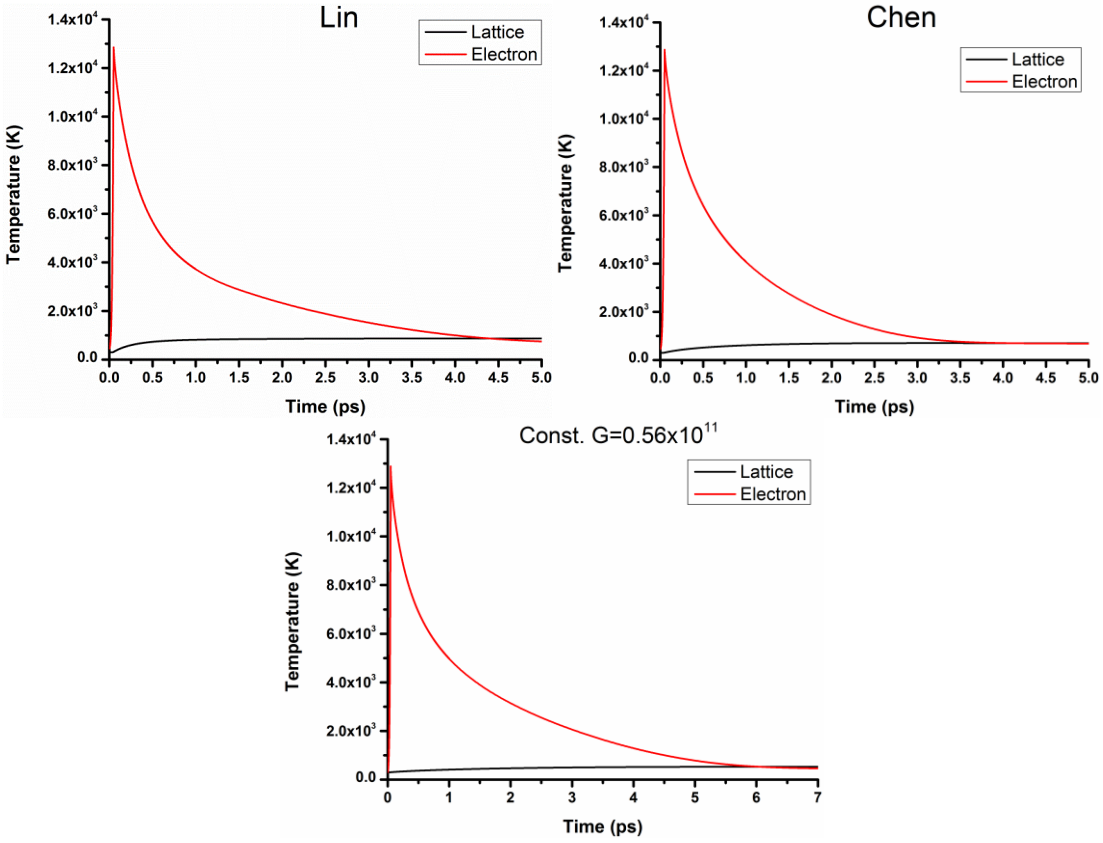

Figure 4.2 Temporal evolution of the surface electron and lattice temperatures of the irradiated copper at the center of laser beam with pulse duration of 50 fs and fluence of 0.05 J/cm^2. Lin's DOS model, Chen's model, and constant electron-phonon coupling factor of 0.56×10^{11} Wcm^{-3}K^{-1}

Figure 4.3 shows the two-dimensional representation of the lattice temperature evolution at the end of the run time with the same laser pulse conditions for Lin's model (top left), Chen's model (top right), and with constant coupling factor (bottom). The

temperature at the surface has the highest values then it decreases along the depth. It can be noticed in this figure that the highest lattice temperature can be achieved if Lin's model is used then Chen's model comes after that, and that is because of the high coupling strength as the electron temperature increases compared by using constant value of the coupling factor. As an example, the maximum lattice temperature at the center of the laser beam was 835 K in the case of Lin's model while it was 676 K and 520 K for Chen's model and constant coupling respectively.

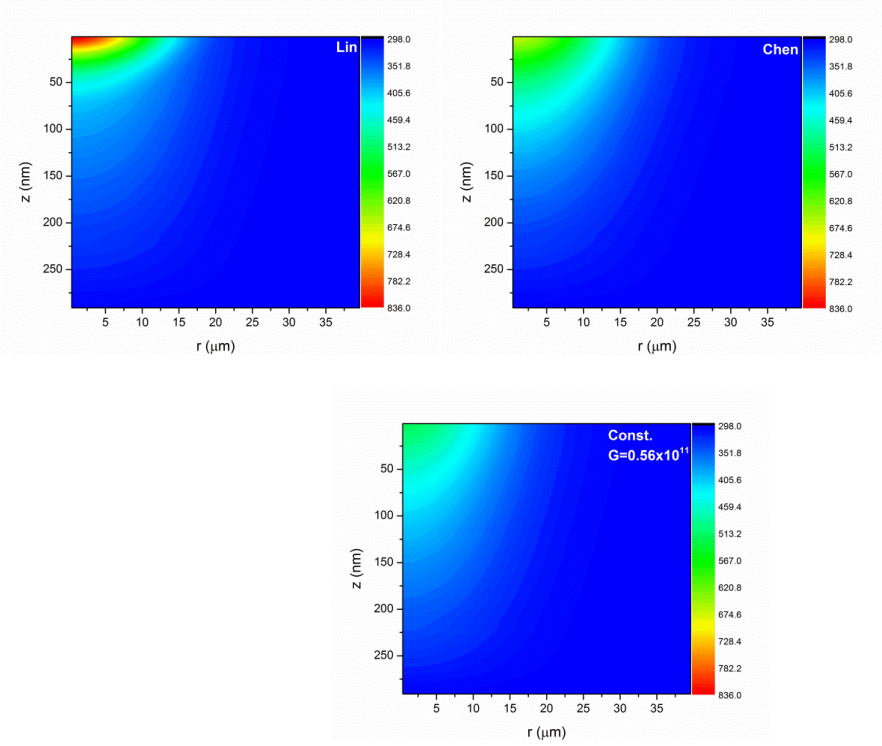

Figure 4.3 Two-dimensional evolution of the lattice temperature of the copper irradiated by laser beam with pulse duration of 50 fs and fluence of 0.05 J/cm^2 at 20 ps, for Lin's model, Chen's model, and constant G factor of 0.56×10^{11} Wcm^{-3}K^{-1}

The relationship between the fluence and the thermalization time is presented in figure 4.4 for laser pulse duration of 200 fs. As can be seen in this figure the thermalization time increases slightly with the fluence in the case of Chen's model and

Lin's model till it becomes independent of the fluence and reaches ~5 ps. While when constant value of electron-phonon coupling factor is used the thermalization time keeps increasing as the fluence increase and this result was reported also in (J. B. Lee, et al., 2011) for the gold target.

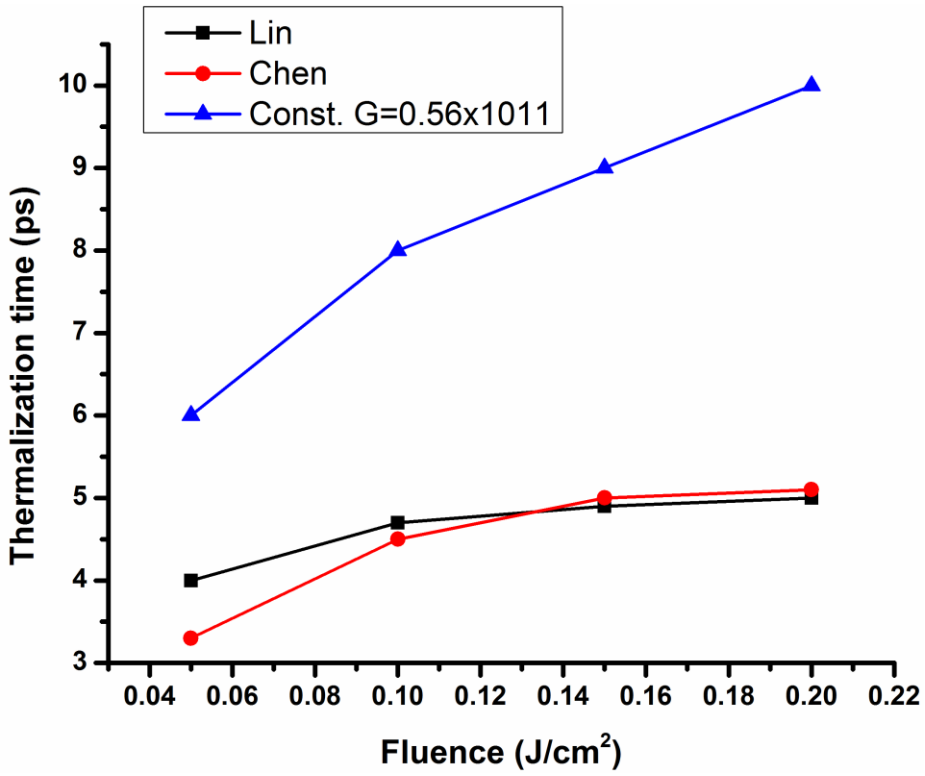

Figure 4.4 Thermalization time versus fluence for the copper irradiated by 200 fs lase pulse using different electron-phonon coupling models

Figure 4.5 shows the maximum ablated depth of the copper irradiated by 200 fs laser beam with various values of fluence. Lin's model gave the highest ablation depth with the minimum ablation threshold of 0.4 J/cm^2 while using the Chen's model increases the ablation threshold to the value of 0.5 J/cm^2 which are in agreement with experimental and analytical result of the ablation threshold of copper (E. G. Gamaly, et al., 2002). It can be

noticed that the very low constant value of electron-phonon coupling factor of 0.56×10^{11} $Wcm^{-3}K^{-1}$ shows no ablation even at high fluence.

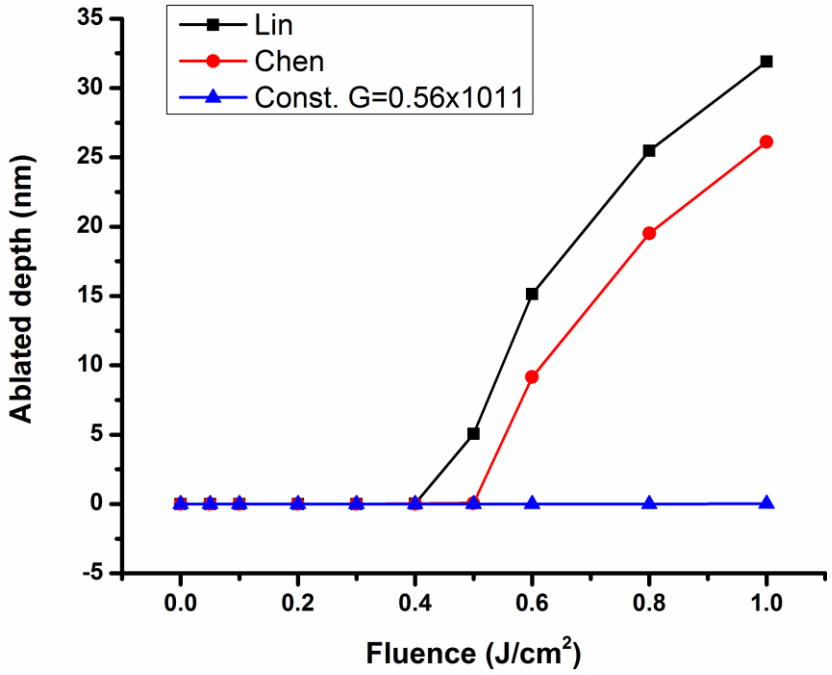

Figure 4.5 The maximum ablated depth of copper at the center of the laser beam with pulse duration of 200 fs at different values of fluence for Lin's model, Chin's model, and constant G of 0.56×10^{11} $Wcm^{-3}K^{-1}$

Since the large scale may prevent showing the very low ablation in the case of constant G-factor, the ablation crater at the fluence of 1 J/cm^2 for each model was presented in figures 4.6 and 4.7. As can be seen in figure 4.4 the crater formed when the Lin's model was used was larger with the maximum ablated depth of 31.9 nm while it is 26.1 nm for the Chen's model. The crater formed when the constant G was used was shown in figure 4.7 with different depth scale; in this case the ablation was negligible.

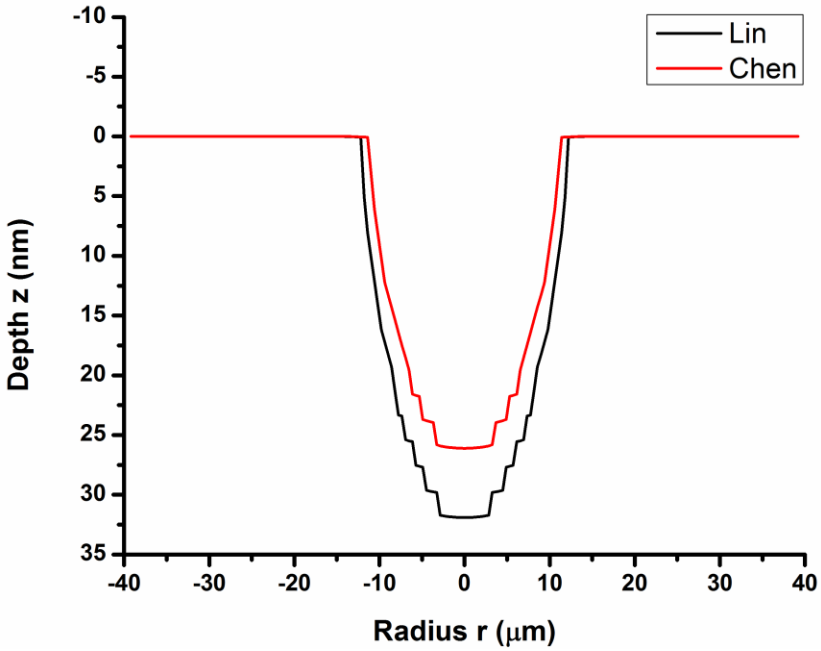

Figure 4.6 The crater profile performed after the ablation of the copper irradiated by laser of pulse duration of 200 fs and fluence of 1 J/cm^2 for Chen's models and Lin's model

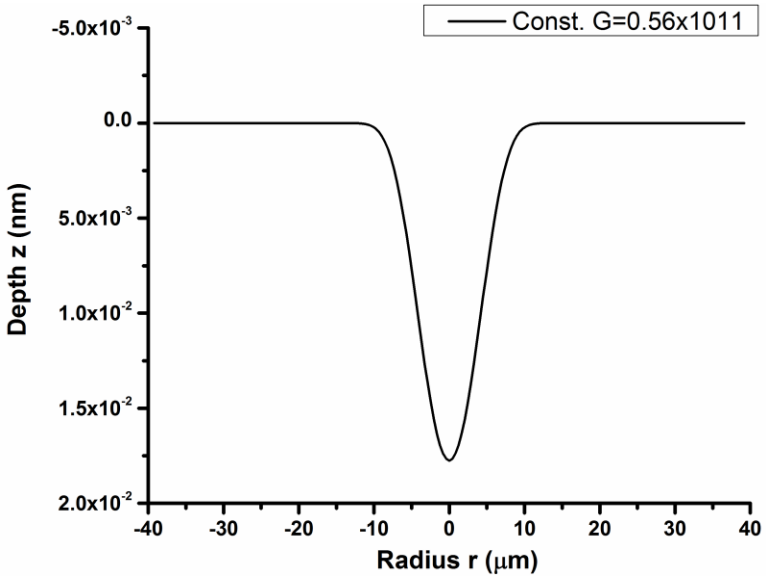

Figure 4.7 The crater profile performed after the ablation of the copper irradiated by laser of pulse duration of 200 fs and fluence of 1 J/cm^2 for temperature independent electron-phonon coupling factor of 0.56×10^{11} Wcm^{-3}K^{-1}

The final objective of this chapter is to investigate the impact of using the temperature dependent electron heat capacity that resulted from the calculation of the DOS (Lin's

model) versus the commonly used linear relation. The comparison between the two mentioned models of the electron heat capacity is presented in figure 4.2. The red line is the Lin's model data fitted by Ren et al. (2011). As can be seen in this figure the Lin's model electron heat capacity was ~ 40% higher than that was calculated using the linear relationship with the electron temperature (the black line).

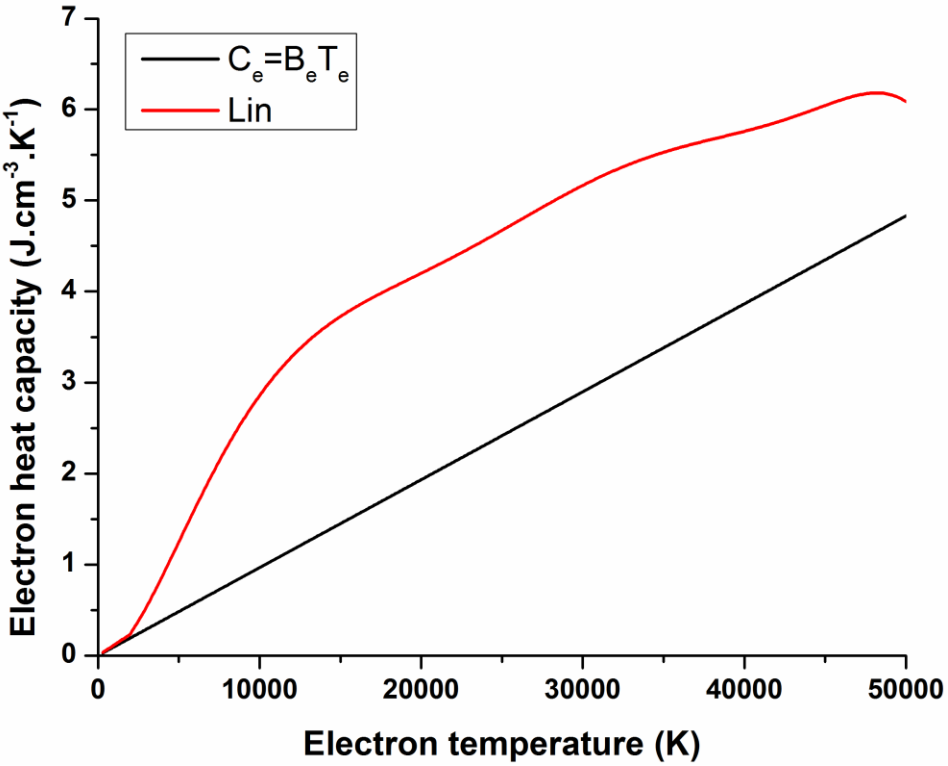

Figure 4.8 Electron heat capacity as a function of electron temperature from using the Lin's DOS model (the red line) and the linear relationship $C_e= B_eT_e$ (the black line)

In order to study the impact of the modified model of electron heat capacity, the temporal evolution of the surface lattice and electron temperature at the center of the laser beam with pulse duration of 200 fs and 0.2 J/cm^2 for Lin's model and linear relation of the electron heat capacity and Chen's model of electron-phonon coupling for both are

presented in figure 4.9. As shown in this figure the, the electron temperature that is achieved by Lin's model had lower value compared to the linear relationship, that refers to the higher electron heat capacity for Lin's model as presented in figure 4.8 which causes to have lower thermal response when the same power is absorbed.

On the other hand is was noted that the thermalization time in the case of using the linear relation for the electron heat capacity is lower than that for the Lin's model, this is caused by the higher electron temperature which increases the electron-phonon coupling factor as shown in figure 4.1 and strengthen the heat coupling process by increasing the coupling rate or in other words decreasing the thermalization time.

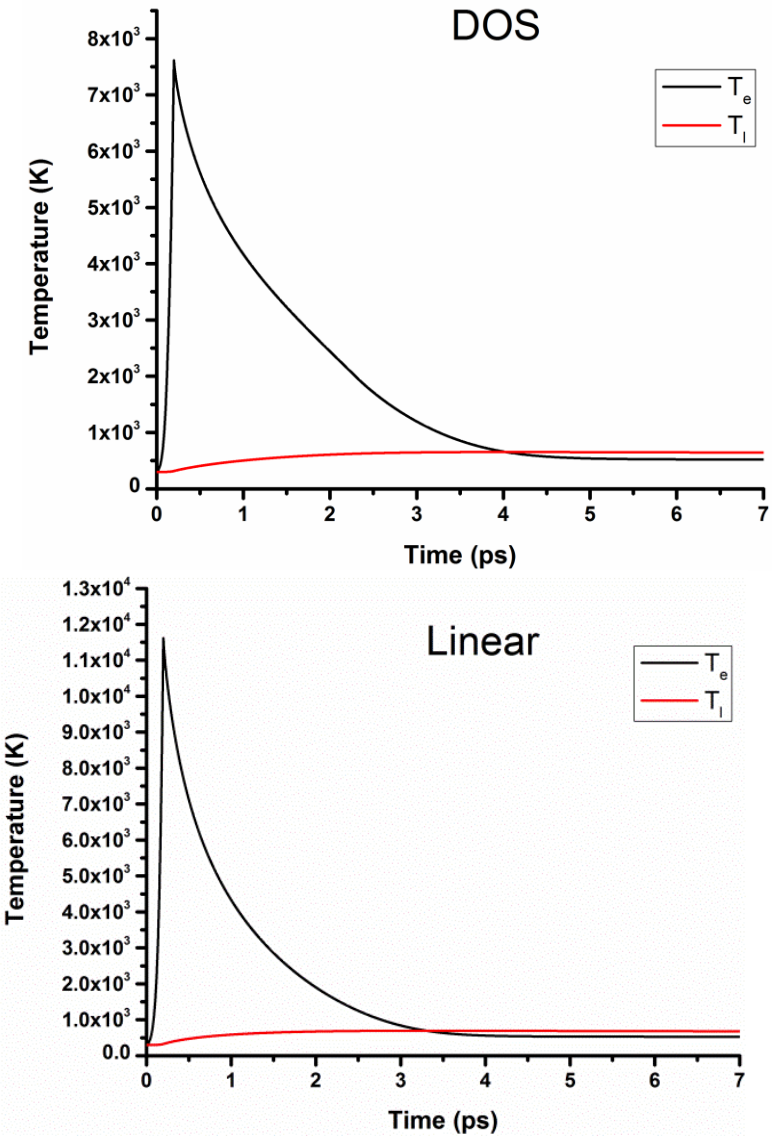

Figure 4.9 The temporal evolution of the surface electron and lattice temperature of copper irradiated by laser beam with pulse duration of 200 fs and 0.2 J/cm^2 using Lin's model and linear relation for the electron heat capacity

Conclusion

In this chapter we investigated the impact of the electron-phonon coupling factor and the electron heat capacity for the copper irradiated by the femtosecond laser pulses.

Two models of the electron phonon coupling was used, the Lin's models in which the excitation of the d band electrons and their contribution to the coupling of the heat between electrons and phonons at high electron temperature was taken into account, the second models was the Chen's model in which the electron-electron collisions and electron-lattice collision calculations were considered. These two models were compared to the commonly used constant values for the electron-phonon coupling factor. It was found that faster coupling, higher lattice temperature, and higher ablation can be achieved by using the Lin's and Chin's models compared to use of the temperature independent value for the electron-phonon coupling factor. The relationship between the fluence and the thermalization was studied as well, it was found that at high fluence the thermalization converges to fixed value regardless of the fluence in the case of Chen's and Lin's models while it continues to increase with the fluence when constant value of the coupling factor is used as reported by lee et al. (2011). The comparison between the Lin's model of the electron heat capacity based on the density of state calculation and the linear relationship between the electron heat capacity and the electron temperature was presented. It was found that the higher electron heat capacity of the Lin's model leads to lower the electron temperature and eventually decreases the rate of the coupling of energy between the electrons and the lattice. Finally, it can be concluded that the temperature dependent electron-phonon coupling and electron heat capacity and the calculations of the electrons excitation and scattering must be taken into account when a target is irradiated by ultrashort laser pulses.

CHAPTER FIVE: THERMAL EVOLUTION IN THE DOUBLE-LAYER METAL TARGET INTERACTION WITH FEMTOSECOND LASER PULSE

Introduction

Multi-layer films or coating-substrate assemblies under the influence of the intense irradiation are widely used for many applications in material science and technology especially for microelectronic devises and metal mirror coatings that desire specific properties (A. M. Chen, Jiang, Sui, Liu, et al., 2011; F. Chen, et al., 2011; Gao, Song, & Lin, 2011; Karakas, Tunc, & Camdali, 2010; K.-C. Liu, 2007; Margetic, Bolshov, Stockhaus, Niemax, & Hergenrder, 2001; T. Q QIU & TIEN, 1994; Sitnikov & Ovchinnikov, 2011). The femtosecond laser pulse is considered as high power radiation because of very short pulse duration that leads to extremely high power density absorbed by the target material with minimum heat-affected zone (Hwang, Chimmalgi, & Grigoropoulos, 2006). When the target is coated by a material with high value of reflectivity such as gold a small portion of the laser energy will be absorbed and diffused through the target and this will minimize the damage that may occur. On the other hand, we can use the double-layer assembly to enhance the thermal response of the first layer by changing the padding layer type with suitable thermal properties mainly the lattice heat capacity and the electron phonon coupling factor (Ibrahim, Elsayed-Ali, Shinn, & Bonner, 2003), or by choosing a minimum thickness of the film leads to the reduction in

the damage caused by the high power density of the laser pulse (A. M. Chen, Y. F. Jiang, L. Z. Sui, H. Liu, et al., 2011; A. M. Chen et al., 2010; Ibrahim, et al., 2003).

Many studies have been performed to investigate the thermal evolution through the multi-layer assemblies. For example, Qiu and Tien (1994) studied the gold-chromium assembly irradiated by femtosecond laser pulse and they investigated the impact of having the chromium as a substrate to reduce the lattice temperature of the gold layer and minimize the thermal damage compared to single gold layer target. They confirmed their simulation results from the two-temperature model by performing femtosecond thermo-reflectivity experiments (Q. QIU, JUHASZ, SUAREZ, W, & TIEN, 1994). Ibrahim et al. (2003) studied the damage threshold of the single gold layer versus multi-layer systems of gold-vanadium and gold-titanium systems. They defined the damage threshold as the fluence needed to cause melting, and they found that the damage threshold for the multi-layer films is higher than that for the single-layer. Karkas et al. (2010) derived a non-Fourier three dimensional transient heat transfer model, HTS model, using the Boltzmann equation to study the heat transfer in gold-chromium multi-layer films irradiated by femtosecond laser. They found that the lattice temperature of the gold layer decreases as a result of depositing more energy in the chromium layer. F. Chen et al. (2011) studied different configurations of double and three-layers assemblies of gold, silver, copper, and aluminum material target under the irradiation by femtosecond laser pulses. They investigated the effect of thermal properties of substrate layer on the thermal response of the first layer numerically by introducing the time dependent electron and lattice temperature distribution. They showed that the electron-phonon coupling factor and the

lattice heat capacity of the substrate have huge impact on the temperature evolution in the first layer. Also, they found that the temperature dependent thermal properties must be taken into account for the ultrashort laser pulse interacting with multi-layer assemblies. A. M. Chen et al. (A. M. Chen, Y. F. Jiang, L. Z. Sui, H. Liu, et al., 2011; 2010) studied the improvement to the damage threshold of gold surface in the case of gold coated chrome using the two-temperature model, they found that higher electron-phonon coupling factor leads to improve the damage threshold, they selected chrome as a substrate metal layer with high melting temperature in order to increase the damage threshold. Finally they reached the highest damage threshold by finding an optimal proportion of thickness of gold and chrome.

In this chapter the thermal response of double-layer target irradiated by femtosecond laser pulse was studied. The temporal electron and lattice evolution of single gold layer, 100 nm of gold coated copper, and 100 nm of gold coated aluminum substrates were investigated by using the two-temperature model. The two-dimensional temporal temperature distributions for each case have been shown. The effect of thermal properties of the substrate material and the comparison between constant electron phonon coupling factor and temperature dependent one was investigated.

Theoretical Model

For the irradiation by femtosecond laser pulse, the two-temperature model (s.I Anisimov & Rethfeld, 1997; Kaganov, et al., 1957) must be used in which the electrons subsystem absorb the laser energy directly and then transfer the heat to the lattice

subsystem by the electron phonon coupling. Figure 5.1 shows a schematic drawing of the laser pulse interaction with double-layer metal films, where l is the thickness of the top-layer and L is the thickness of the two layers.

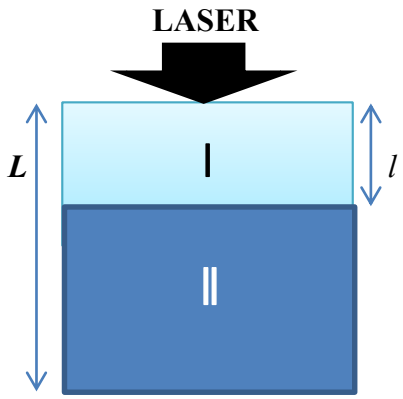

Figure 5.1 Schematic drawing of double-layer films irradiated by femtosecond laser pulse at the top

Temperature and phase dependent thermal properties in two-dimensional cylindrical coordinate and two-temperature model is used for both layers as following (A. M. Chen, Y. F. Jiang, L. Z. Sui, H. Liu, et al., 2011; A. M. Chen, et al., 2010; F. Chen, et al., 2011; Gao, et al., 2011; K.-C. Liu, 2007; T. Q QIU & TIEN, 1994; Tzou, Chen, & Beraun, 2002; Wang, Dai, & Melnik, 2006):

$$C_e^{\mathrm{I}} \frac{\partial T_e^{\mathrm{I}}}{\partial t} = \frac{1}{r}\frac{\partial}{\partial r}\left(K_e^{\mathrm{I}}\, r \frac{\partial T_e^{\mathrm{I}}}{\partial r}\right) + \frac{\partial^2 T_e^{\mathrm{I}}}{\partial z^2} - G^{\mathrm{I}}\left(T_e^{\mathrm{I}} - T_l^{\mathrm{I}}\right) + S^{\mathrm{I}}(r,z,t) \tag{5.1}$$

$$C_l^{\mathrm{I}} \frac{\partial T_l^{\mathrm{I}}}{\partial t} = G^{\mathrm{I}}\left(T_e^{\mathrm{I}} - T_l^{\mathrm{I}}\right) \tag{5.2}$$

$$C_e^{\mathrm{II}} \frac{\partial T_e^{\mathrm{II}}}{\partial t} = \frac{1}{r}\frac{\partial}{\partial r}\left(K_e^{\mathrm{II}}\, r \frac{\partial T_e^{\mathrm{II}}}{\partial r}\right) + \frac{\partial^2 T_e^{\mathrm{II}}}{\partial z^2} - G^{\mathrm{II}}\left(T_e^{\mathrm{II}} - T_l^{\mathrm{II}}\right) \tag{5.3}$$

$$C_l^{\parallel}\frac{\partial T_l^{\parallel}}{\partial t} = G^{\mid}\left(T_e^{\parallel} - T_l^{\parallel}\right) \tag{5.4}$$

Again, C_e, C_l, K_e and G are electron and lattice heat capacity, electronic heat conductivity and electron-phonon coupling factor respectively for each layer. All of these thermal properties are material, phase and temperature dependent. The electron-phonon coupling factor, G, is calculated from Chen's model with the following equation which was presented in chapter 4 (F. Chen, et al., 2011; J. K. Chen, et al., 2005; Hopkins & Norris, 2007):

$$G(T_e, T_l) = G_{RT}\left[\frac{A_e}{B_l}(T_e + T_l) + 1\right] \tag{5.5}$$

The equations for other thermal properties and the definition of the constants in these equations were discussed in chapters 2 and 3 in details.

The laser heat flux in equation 5.1 has the Gaussian temporal and spatial distribution as discussed previously:

$$S^{\mid}(r,z,t) = I_{\circ} \times (1 - R^{\mid}) \times 0.94 \times \left(\exp\left(-2.77 * \left(\frac{t - 2tp}{tp}\right)^2\right)\right) \times \exp\left(-.5 * \left(\frac{r^2}{\sigma 2}\right)\right) \times \exp\left(-\frac{z}{\alpha}\right) \tag{5.6}$$

Where, $R^{\mid}$ is the reflectivity of the top-layer which is 0.95 for the gold, t_p is the pulse duration; σ is spatial profile parameter and α is the absorption coefficient of gold 15.3 nm (Karakas, et al., 2010). The constants used to calculate thermal properties for gold, copper and aluminum are tabulated in table 5.1 (A. M. Chen, Y. F. Jiang, L. Z. Sui, H.

Liu, et al., 2011; A. M. Chen, et al., 2010; F. Chen, et al., 2011; Gragossian, Tavassoli, & Shokri, 2009; Hu et al., 2011; Sonntag, et al., 2009; Yilbas, 2002).

Table 5.1

Thermal Properties and Constants for Au, Cu and Al

	B_e $Jcm^{-3}k^{-2}$	χ	η	G_{RT} $Wcm^{-3}k^{-1}$	A_e $s^{-1}k^{-2}$ $\times10^7$	B_l $s^{-1}k^{-1}$ $\times10^{11}$	Γ_F K $\times10^4$	T_m K
Au	68×10^{-6}	3.53	0.16	2.1×10^{10}	1.18	1.25	6.4	1336
Cu	96.6×10^{-6}	3.77	0.14	1×10^{11}	1.28	1.23	8.12	1356
Al	135×10^{-6}	2.29	0.14	2.45×10^{11}	0.376	3.9	3.5	933

Initial and Boundary Conditions

The initial conditions are assumed to be 300 K of electron and lattice temperature at any r and z for both layers:

$$T_e^{\mathrm{I}}(t=0,r,z) = T_e^{\mathrm{II}}(t=0,r,z) = T_l^{\mathrm{I}}(t=0,r,z) = T_l^{\mathrm{II}}(t=0,r,z) = 300\ K \qquad (5.7)$$

It was assumed that no heat losses across the boundaries for both electron and lattice, and also we assumed perfect thermal contact at the interface (z = l) (A. M. Chen, Y. F. Jiang, L. Z. Sui, H. Liu, et al., 2011; A. M. Chen, et al., 2010; Gao, et al., 2011; Karakas, et al., 2010; Wang, et al., 2006):

$$\nabla.T_e^{\mathrm{I}}(t,r,z=0,\infty) = \nabla.T_e^{\mathrm{II}}(t,r,z=0,\infty) = 0 \qquad (5.8)$$

$$\nabla . T_l^{\mathrm{I}}(t, r = 0, \infty, z) = \nabla . T_l^{\mathrm{II}}(t, r = 0, \infty, z) = 0 \quad (5.9)$$

$$T_e^{\mathrm{I}}(t, r, z = l) = T_e^{\mathrm{II}}(t, r, z = l) \quad (5.10)$$

$$T_l^{\mathrm{I}}(t, r, z = l) = T_l^{\mathrm{II}}(t, r, z = l) \quad (5.11)$$

$$\nabla . T_e^{\mathrm{I}}(t, r, z = l) = \nabla . T_e^{\mathrm{II}}(t, r, z = l) \quad (5.12)$$

$$\nabla . T_l^{\mathrm{I}}(t, r, z = l) = \nabla . T_l^{\mathrm{II}}(t, r, z = l) \quad (5.13)$$

The two-temperature model equations system for the double-layer metal films was solved numerically using the finite difference in A*THERMAL-2 code (A. Hassanein, 1996) with some modifications by taking into account the temperature and phase dependent thermal properties. The calculations were carried out for the laser fluence of 0.2 J/cm^2 with pulse duration of 100 fs and spot size of 50 μm. Two different double-layer compositions were studied: 100 nm of gold film on copper substrate and 100 nm of gold film on aluminum substrate.

Results and Discussion

The temporal distribution of surface electron and lattice temperature at the center of the laser beam and the spatial lattice temperature distribution at 5 ps of pure single metals of gold, copper, and aluminum are presented in figures 5.2, 5.3 and 5.4 respectively. This is just to show the thermal response for each metal under irradiation of the femtosecond laser pulse of 100 fs and 0.2 J/cm^2 and how each material acts as a single-layer and when

it will be coupled with other metal layer. The maximum electron temperatures for Au, Cu and Al are 8916 K, 8118 K and 15220 K respectively. As can be seen in these figures the copper and aluminum electron and lattice subsystems reached the equilibrium earlier than gold because of the higher value of electron-phonon coupling factor. The equilibrium value of the lattice temperatures for Au, Cu and Al are 393 K, 467 K and 1375 K respectively. Higher value of aluminum lattice temperature refers to its low lattice heat capacity.

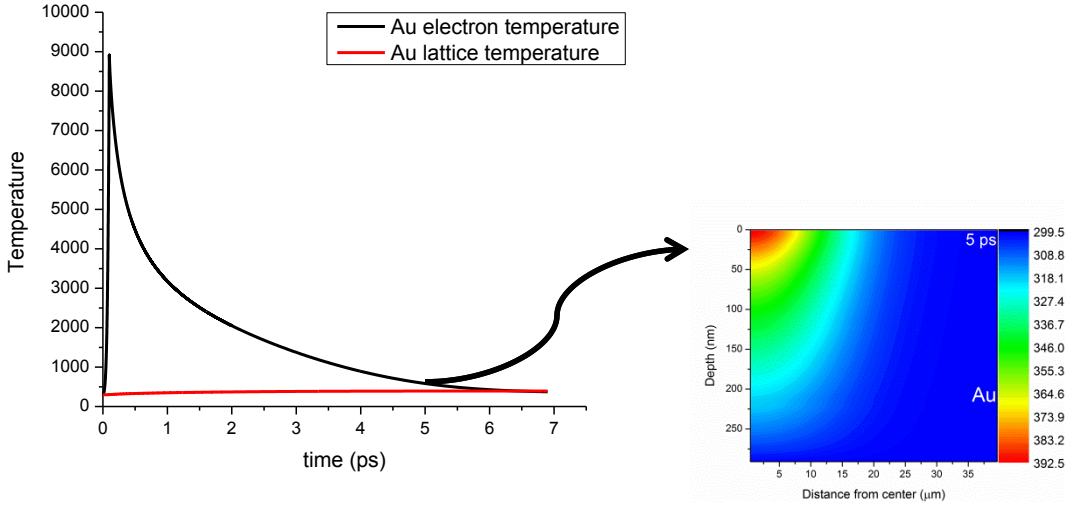

Figure 5.2 Temporal distribution of electron and lattice temperatures of Au surface at the center of the laser beam of 100 fs and 0.2 J/cm^2, R=0.95 (at the left), spatial distribution of the lattice temperature at 5 ps (at the right)

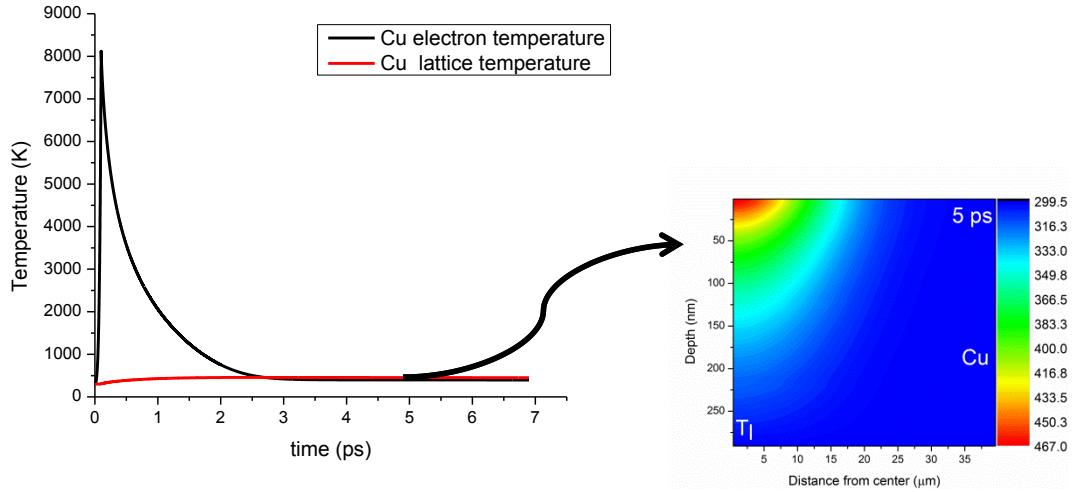

Figure 5.3 Temporal distribution of electron and lattice temperatures of Cu surface at the center of the laser beam of 100 fs and 0.2 J/cm^2, R=0.7 (at the left), spatial distribution of the lattice temperature at 5 ps (at the right)

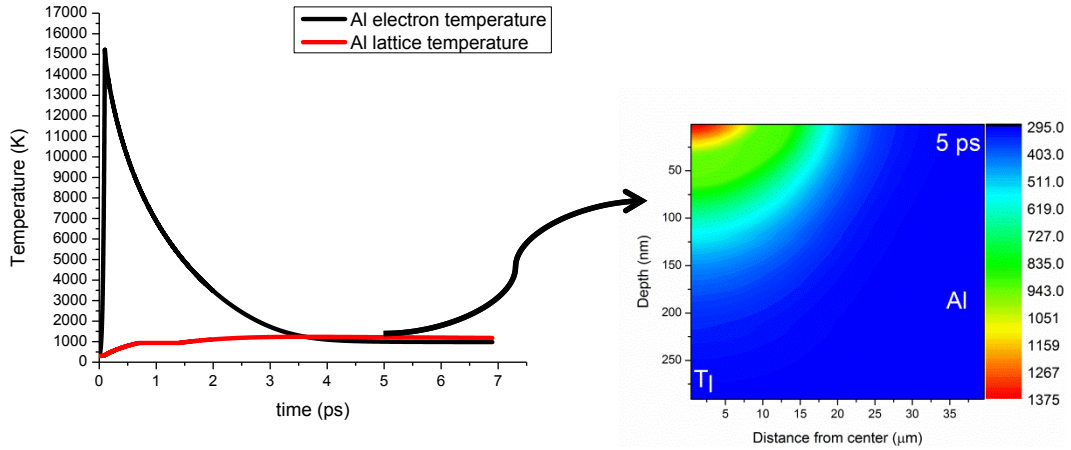

Figure 5.4 Temporal distribution of electron and lattice temperatures of Al surface at the center of the laser beam of 100 fs and 0.2 J/cm^2 (at the left), spatial distribution of the lattice temperature at 5 ps (at the right)

Figure 5.5 shows the temporal distribution of surface electron temperature at the center of the laser pulse of 100 fs and 0.2 J/cm^2 for three different target configurations: single-layer of gold, double-layer of gold/copper films and double-layer of

gold/aluminum films. It is clear that up to 1 picosecond the temporal distribution of the electron temperature for all three cases have the same behavior and they reach the maximum temperature of 8916 K, after that the temperature distribution for the double-layer films shows some deviation from the single pure gold film. For example, in the case of the gold-copper assembly which is represented by dotted line, the temperature goes down faster that means the equilibrium occurs earlier because of the high value of electron phonon coupling factor of copper. But in the case of gold-aluminum assembly that is represented by the dashed line, the temperature at the end of the run time is higher compared to single gold because of the low value of lattice specific heat of aluminum.

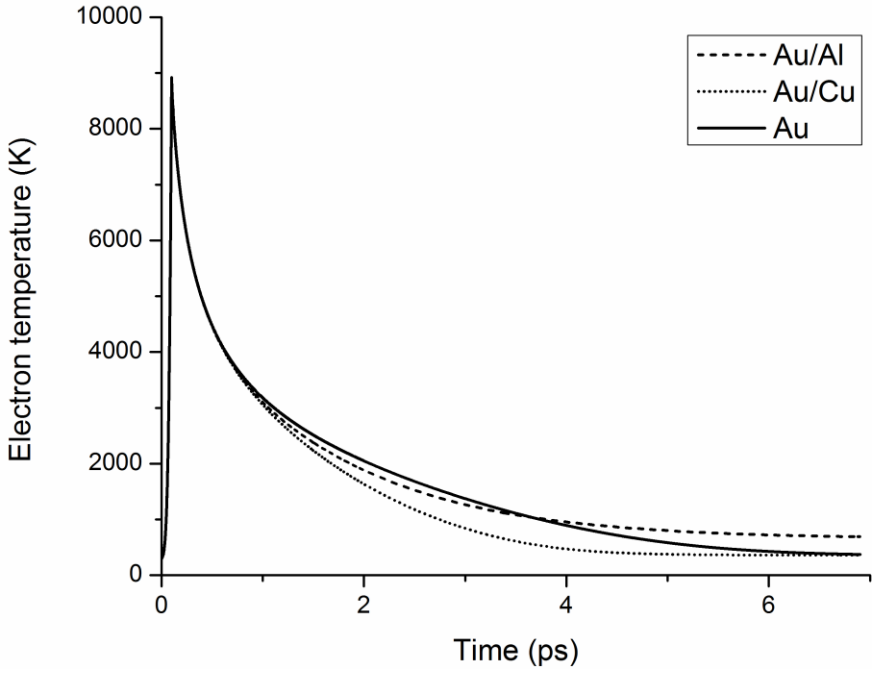

Figure 5.5 Temporal distribution of the surface electron temperature at the center of the laser beam of 100 fs and 0.2 J/cm^2, for single gold layer, double-layer of gold/copper films and double-layer of gold/aluminum films

The temporal evolution of the surface lattice temperature at the center of the same laser beam for Au, Au/Cu and Au/Al is shown in figure 5.6, same temperature distribution for the three cases up to 2 ps then the temperature distribution becomes different. The lattice temperature at the end of run time of 7 ps for the single Au is 393 K while it is 360 K and 395 K in the case of Au/Cu and Au/Al respectively. It is clear that for Au and Au/Cu the system reaches the equilibrium as the lattice temperature becomes constant with time with a noticeable reduction of the temperature at the surface of Au/Cu that refers to the high value of electron phonon coupling factor of copper so the copper substrate acts as a heat sink where the temperature in the copper layer film increases as a result of preferential coupling of the heat at the interface and that causes a reduction in the temperature at the surface of gold as expected and reported in (F. Chen, et al., 2011). While the surface lattice temperature of Au/Al keeps increasing with time due to very low specific heat of aluminum layer (F. Chen, et al., 2011).

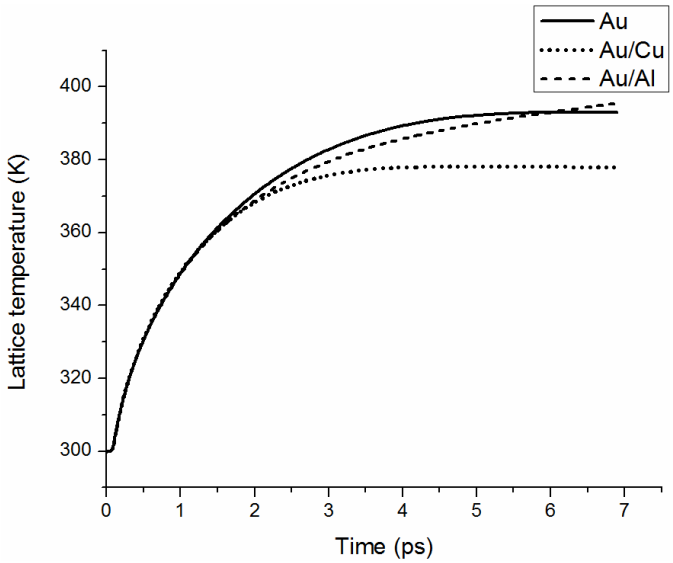

Figure 5.6 Temporal distribution of the surface lattice temperature at the center of the laser beam of 100 fs and 0.2 J/cm^2, for single gold layer, double-layer of gold/copper films and double-layer of gold/aluminum films

Figures 5.7 and 5.8 show the electron and lattice temperature spatial distribution respectively in the single Au film after irradiation by the laser pulse of 100 fs and 0.2 J/cm^2 at different times. It can be seen that once the surface electrons absorb the photon energy from the laser beam the temperature increase suddenly to its maximum value of 8916 K in a very short time and then the energy transfers to other electrons, and the heat diffuses inside the target with time, at this time the lattice temperature remains at room temperature. After the steady state between the electrons is achieved the coupling of the heat from electrons to the phonons in the system starts, which leads to the reduction in the electron temperature and increasing in the lattice temperature with the time until the equilibrium between the electron and lattice system is achieved. It should be mentioned that the diffusion of the heat for both electrons and phonon subsystems are from the surface to the bulk of the target.

For the double-layer Au/Al films irradiated by the laser pulse at the same conditions, the lattice and electron spatial distribution with time can be seen in figures 5.9 and 5.10, the electron temperature distribution has almost the same behavior as that in the case of single Au layer but in this case the surface electrons of the top-layer absorb the photon energy and the heat diffuses to the bulk of this layer which caused by the electronic thermal conduction, then at the interface (z = 100 nm) the electrons transfer the heat to the electrons of the second layer which leads to the increasing in the electron temperature and causes heat diffusion spatially. In the case of the lattice temperature spatial distribution, since the electron-phonon coupling factor of Al is very high compared to Au preferential coupling of the heat between the electrons and the phonons of Al layer (F.

Chen, et al., 2011) leads to the increasing in the lattice temperature at the interface which diffuses through the bulk of the second layer, after that the electron phonon coupling occurs at the surface of the first layer which causes increasing in the lattice temperature and decreasing in the electron temperature as can be seen. It is clear that the temperature at the interface is higher than that at the surface of the Au and also the heat diffusion rate at the interface is higher as well.

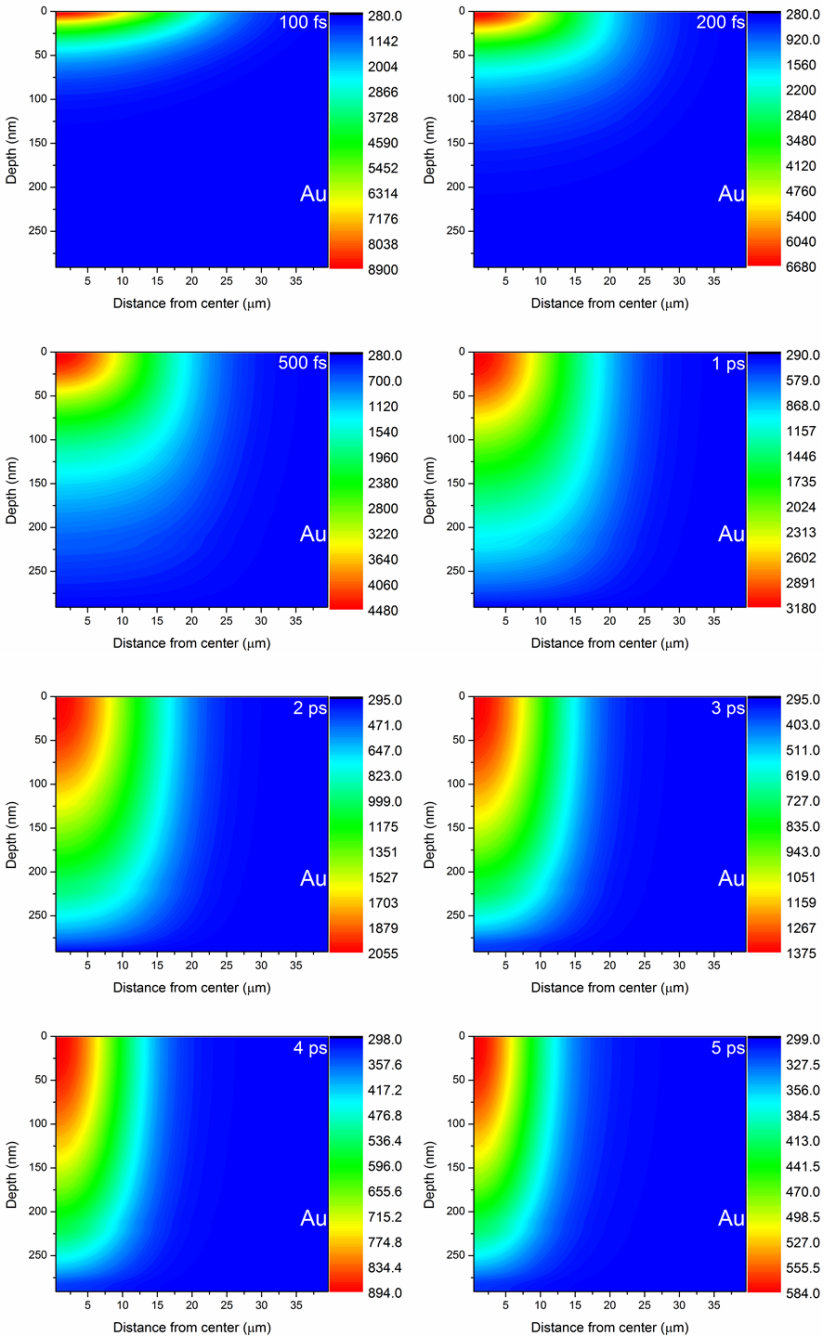

Figure 5.7 Two-dimensional electron temperature distribution at different times for single Au film, 100 fs and 0.2 J/cm^2

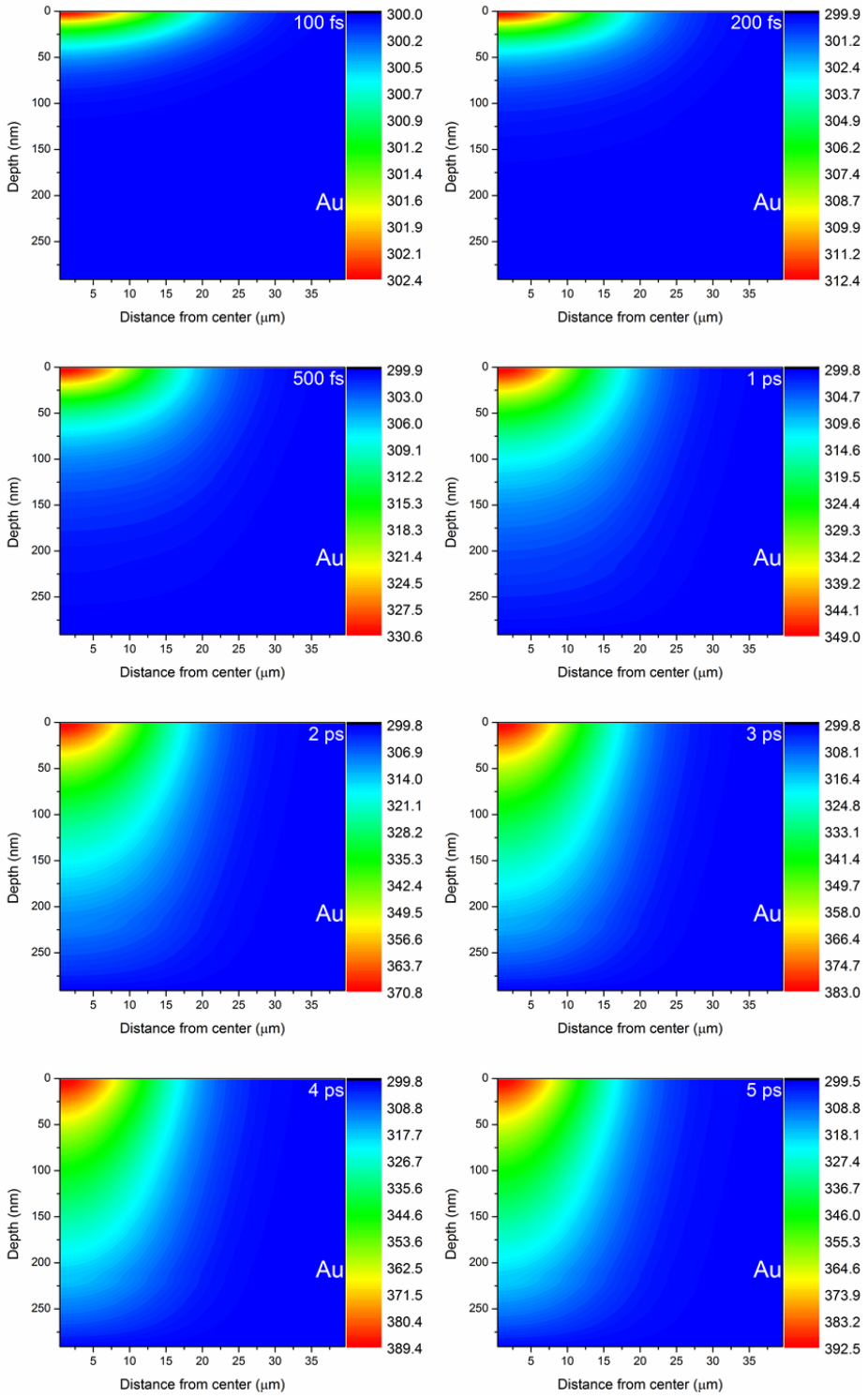

Figure 5.8 Two-dimensional lattice temperature distribution at different times for single Au film, 100 fs and 0.2 J/cm^2

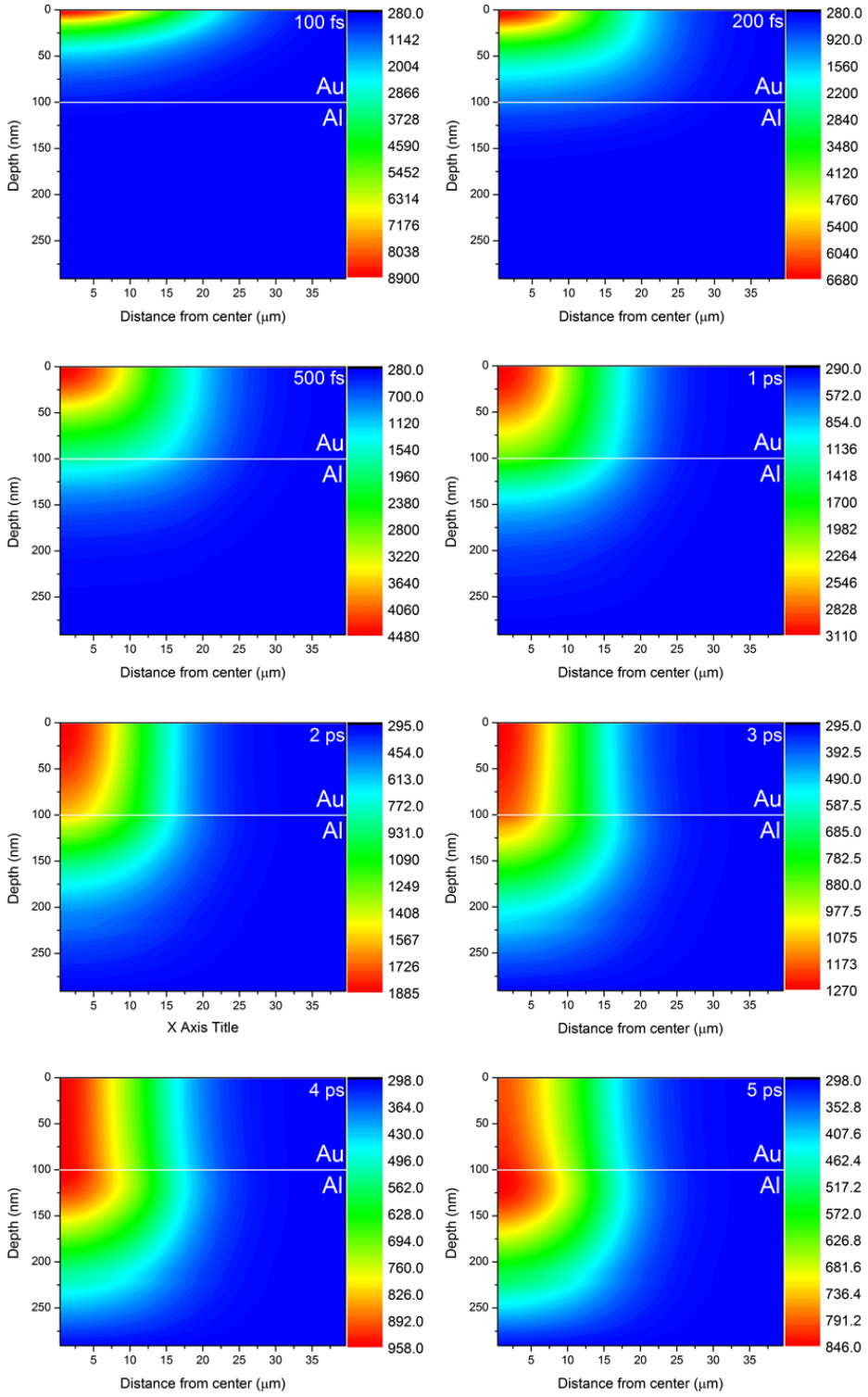

Figure 5.9 Two-dimensional electron temperature distribution at different times for double-layer films of Au/Al, 100 fs and 0.2 J/cm^2

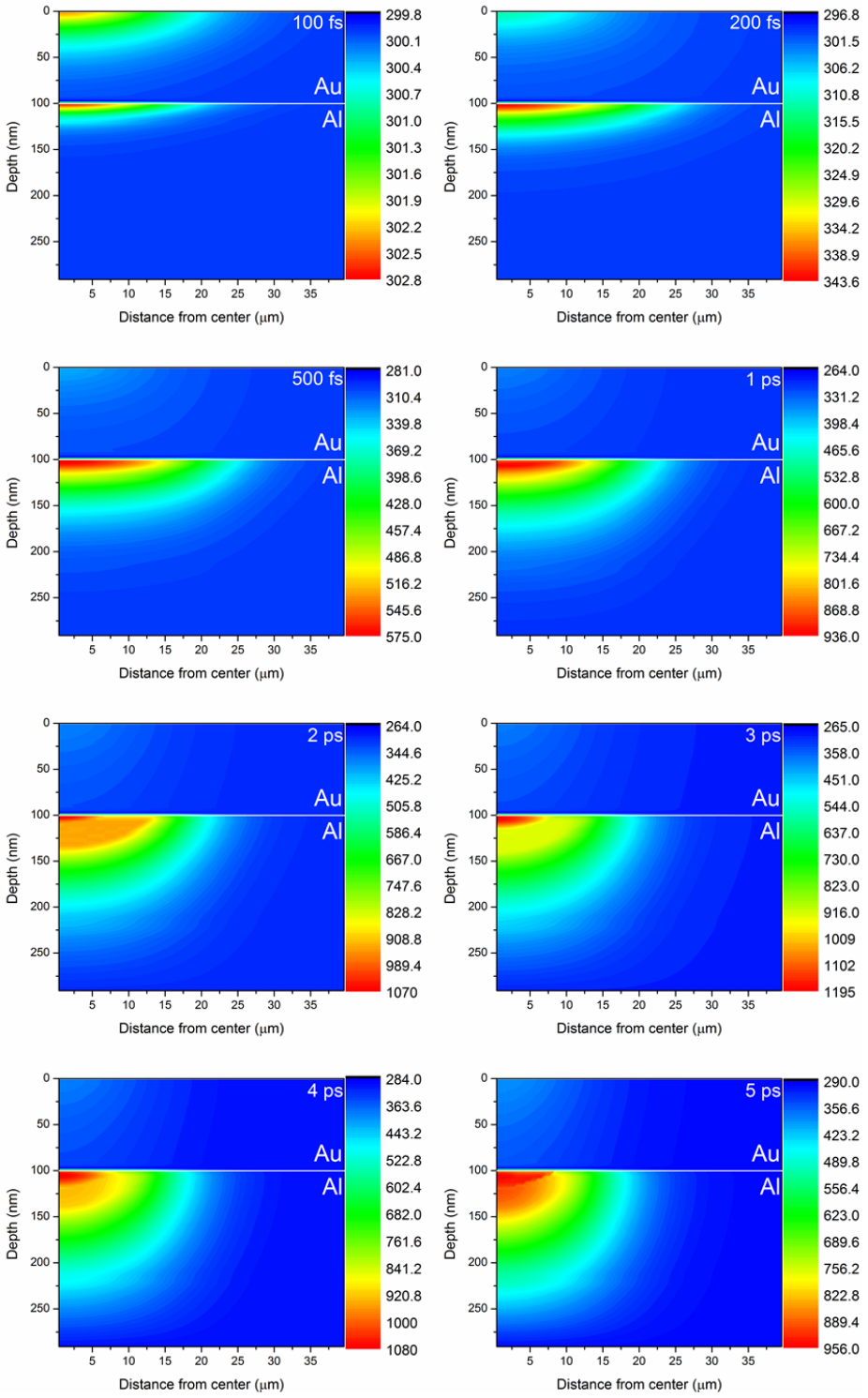

Figure 5.10 Two-dimensional lattice temperature distribution at different times for double-layer films of Au/Al, 100 fs and 0.2 J/cm^2

The lattice and electron temperature spatial distribution of Au/Cu at different times are presented in figures 5.11 and 5.12 respectively. The electron temperature evolution in time and space is almost similar to that in the case of single Au layer target, but again the lattice temperature evolution shows different behavior similar to the Au/Al assembly where the high electron-phonon coupling factor of the copper let this layer act as a heat sink (Ibrahim, et al., 2003), that lowers the temperature in the first layer. It is noted that the temperature rise at the interface is less than that for Au/Al because the specific heat of Al is very small, so little bit of the energy absorbed causes high increase in the temperature.

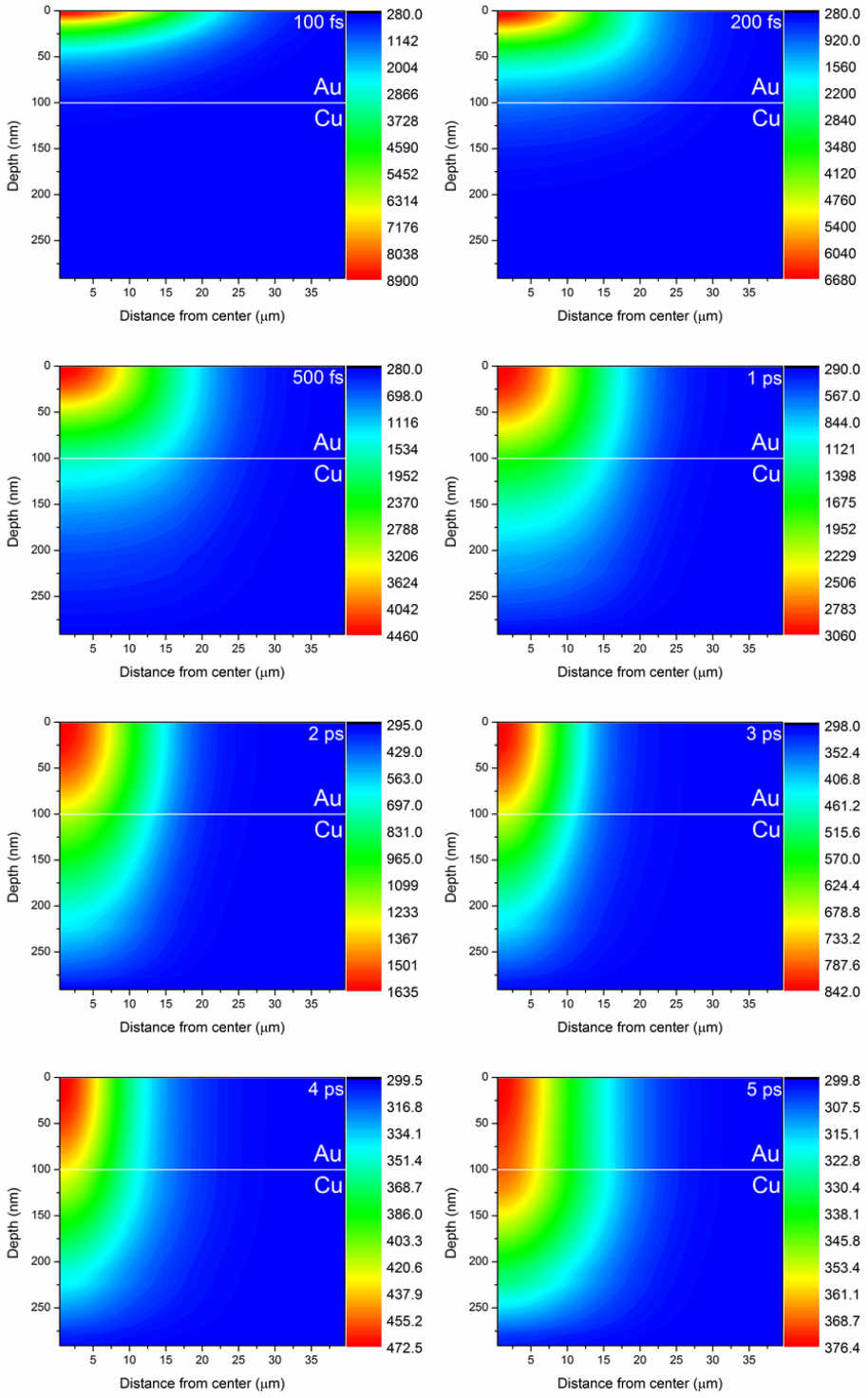

Figure. 5.11 Two-dimensional electron temperature distribution at different times for double-layer films of Au/Cu , 100 fs and 0.2 J/cm^2

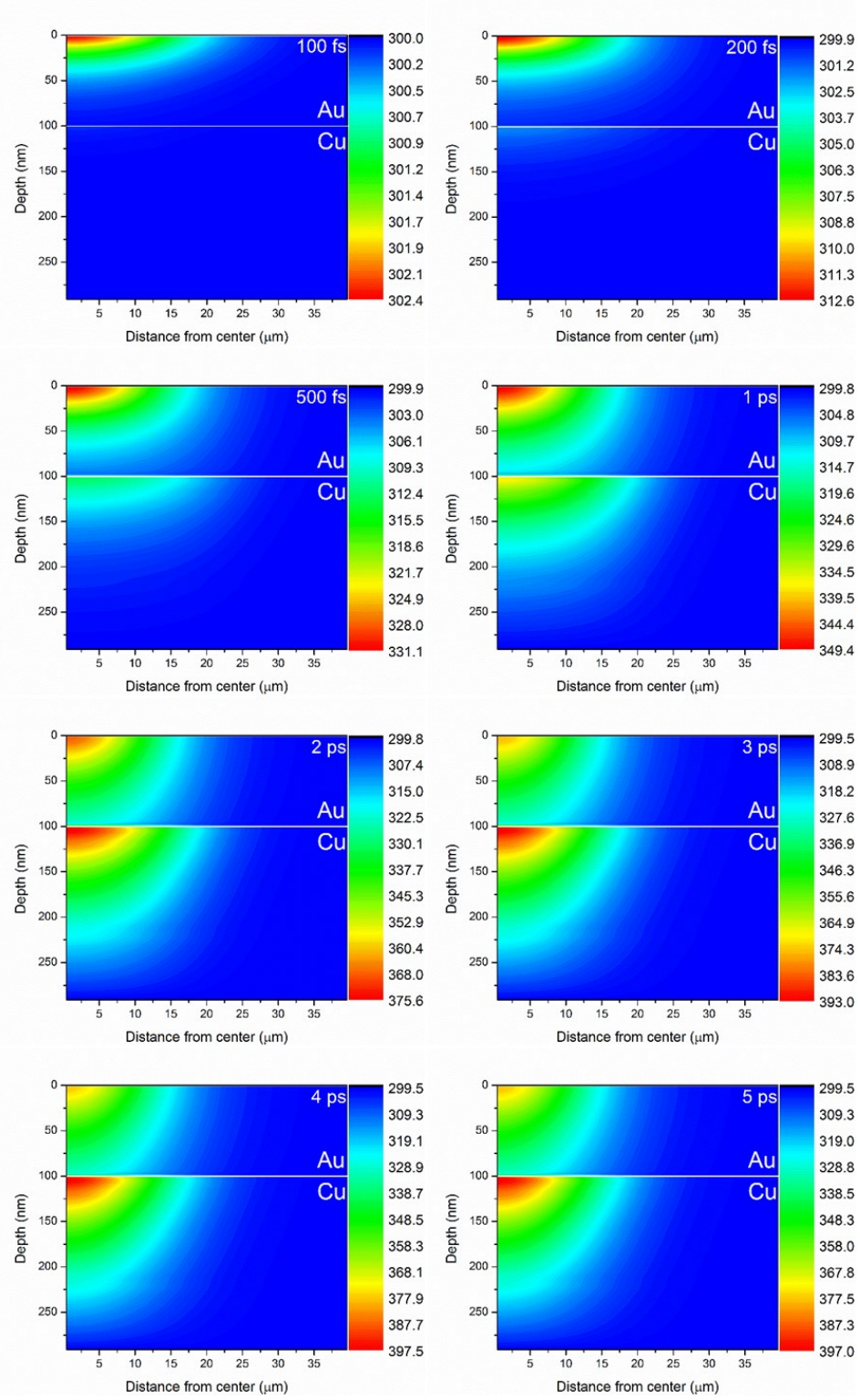

Figure 5.12 Two-dimensional lattice temperature distribution at different times for double-layer films of Au/Cu, 100 fs and 0.2 J/cm^2

Figure 5.13 shows the temporal distribution of electron temperature for the double-layer of Au/Al films at the center of laser beam of 100 fs and 0.2 J/cm^2 at different depths. The solid line represents the temperature at the surface which has the highest values because these electrons absorb the photon energy directly, then the energy diffuse along the depth where the temperature starts to decrease. For example, the maximum temperatures at the surface, at 60 nm, at the interface (100 nm) and at 200 nm are 8916 K, 2803 K, 1952 K, and 829 K respectively. In addition, the temperature distributions lines that represent deeper depths also have different shapes without steep increasing at the beginning as can be seen in the figure.

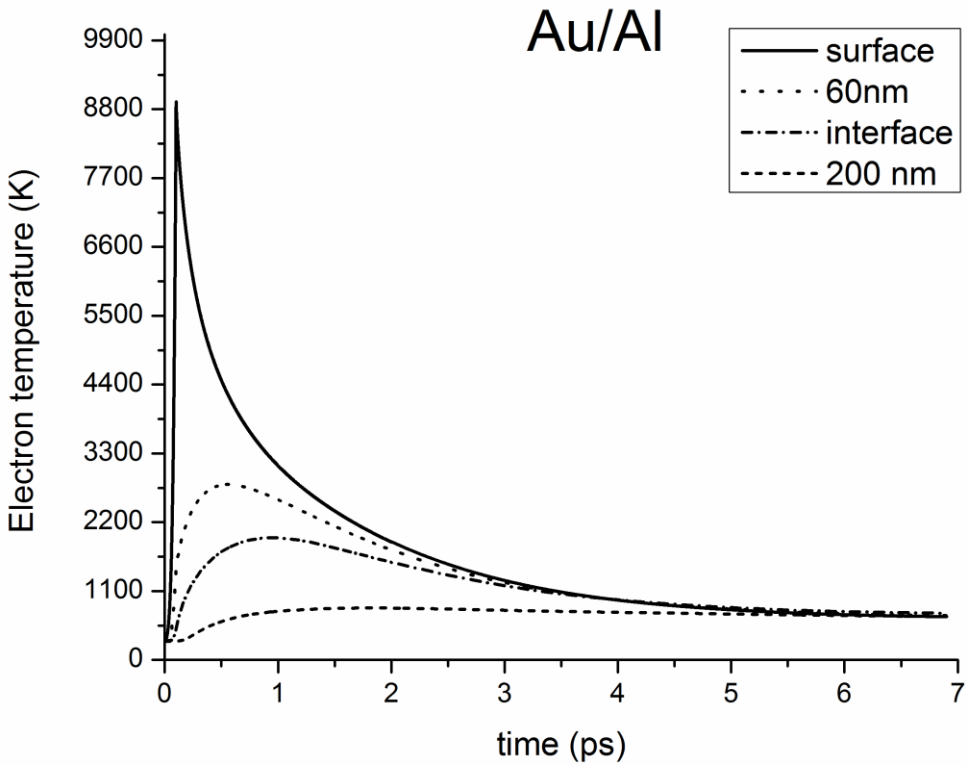

Figure 5.13 Temporal distribution of surface electron temperature of double-layer films of Au/Al at the center of the laser beam, 100 fs and 0.2 J/cm^2, at different depths

The temporal distribution of the lattice temperature of Au/Al at the center of the laser beam of the same conditions with different depths is shown in figure 5. 14. It is clear that the interface temperature (the dashed-dotted line) shows the highest values. Again this refers to the higher value of electron-phonon coupling factor of Al, next to it the temperatures at 200 nm then the surface temperature (solid line) and finally the lowest temperature distribution is at 60 nm, which is within the top-layer. For example at 2 ps the temperature at the surface was 369 K while it was 338 K, 774 K and 672 K at 60 nm, interface and 200 nm respectively.

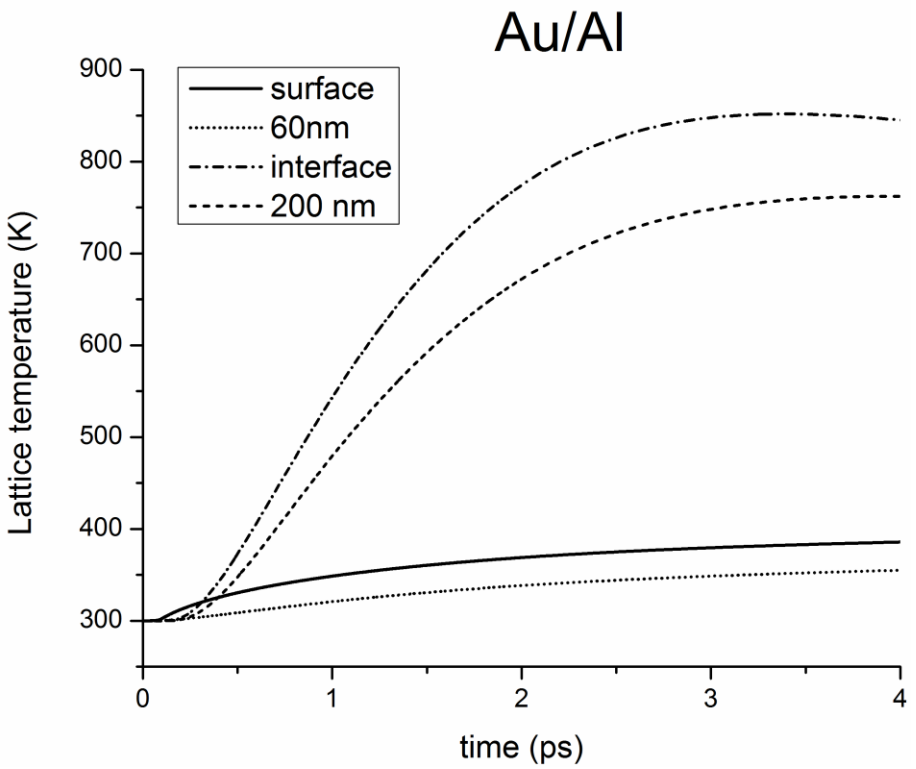

Figure 5.14 Temporal distribution of surface lattice temperature of double-layer films of Au/Al at the center of the laser beam, 100 fs and 0.2 J/cm^2, at different depths

The temporal distribution of electron temperature of Au/Cu at the center of the laser pulse for different depth can be seen in figure 5. 15. It is clear that the temperature has the highest values with time at the surface that is represented by the solid line then the temperature goes down along the depth. For example the maximum electron temperature at the surface was 8916 K and it was 2775 K, 1801 K, and 1125 K at 60 nm, 100 nm (interface) and 200 nm respectively.

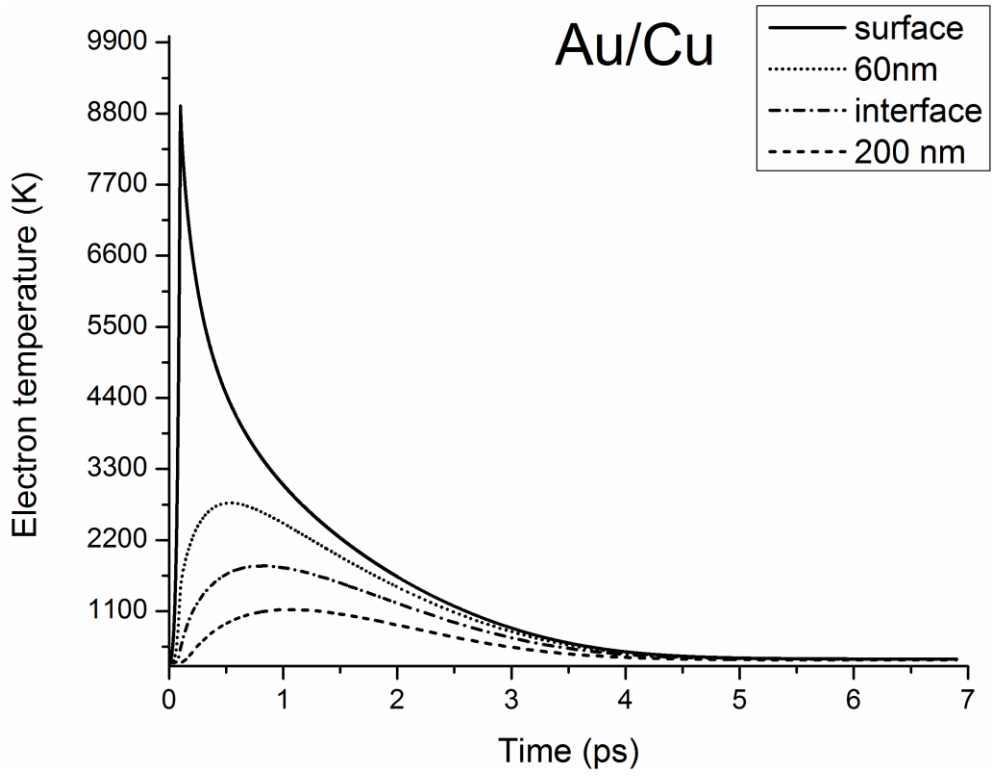

Figure 5.15 Temporal distribution of surface electron temperature of double-layer films of Au/Cu at the center of the laser beam, 100 fs and 0.2 J/cm^2, at different depths

Figure 5.16 shows the temporal distribution of the lattice temperature for Au/Cu at the center of the laser pulse, as can be seen in this figure the temperature has its maximum at the surface (solid line) at the beginning then the maximum lattice

temperature was at the interface (dash-dotted line) where the coupling factor is higher. For example the temperatures at 2 ps were 368 K, 336 K, 379 K, and 340 K at the surface, 60 nm, interface and 200 nm respectively.

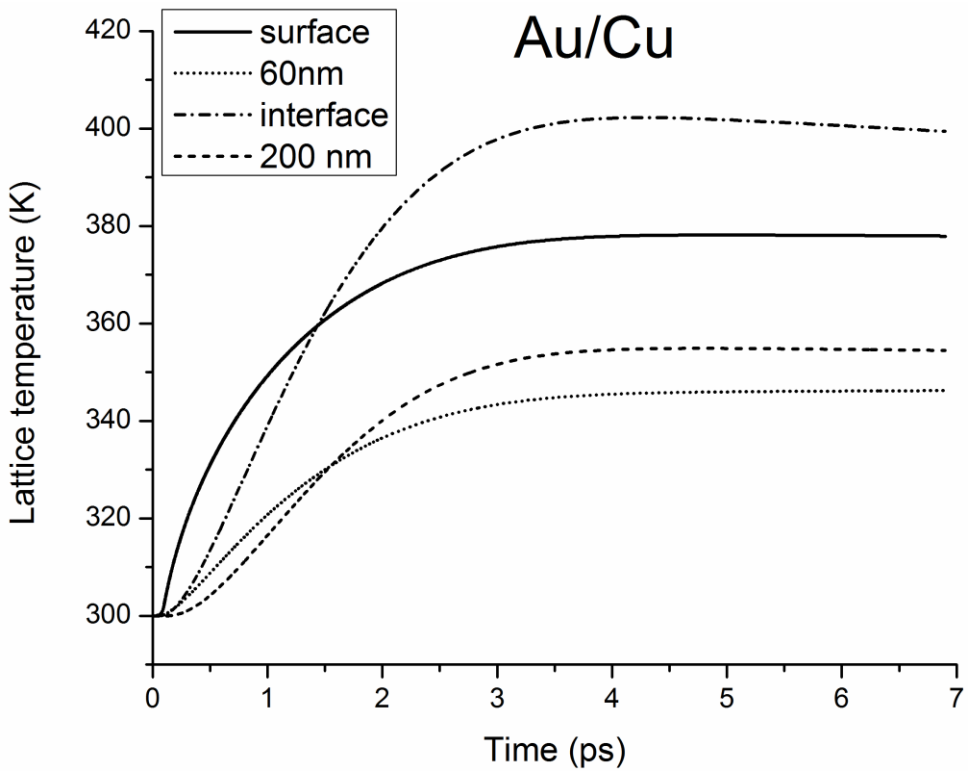

Figure 5.16 Temporal distribution of surface lattice temperature of double-layer films of Au/Cu at the center of the laser beam, 100 fs and 0.2 J/cm^2, at different depths

Figure 5.17 shows the spatial distribution of electron temperature of Au/Cu assembly at the center of the laser beam at different times. At all values of times the electron temperature had the maximum value at the center, then it decreases gradually along the depth. As can be seen in this figure the surface electron temperature decreases with time after 100 fs because of the heat coupling with the lattice subsystem, in addition, the heat

diffuses more inside the assembly where the electron temperature increases along the depth with time as can be seen in the lines of 500 fs and 1 ps where the heat diffuses more along z direction compared to the line of 100 fs but the electron temperature decreases eventually until the equilibrium with the lattice subsystem is achieved.

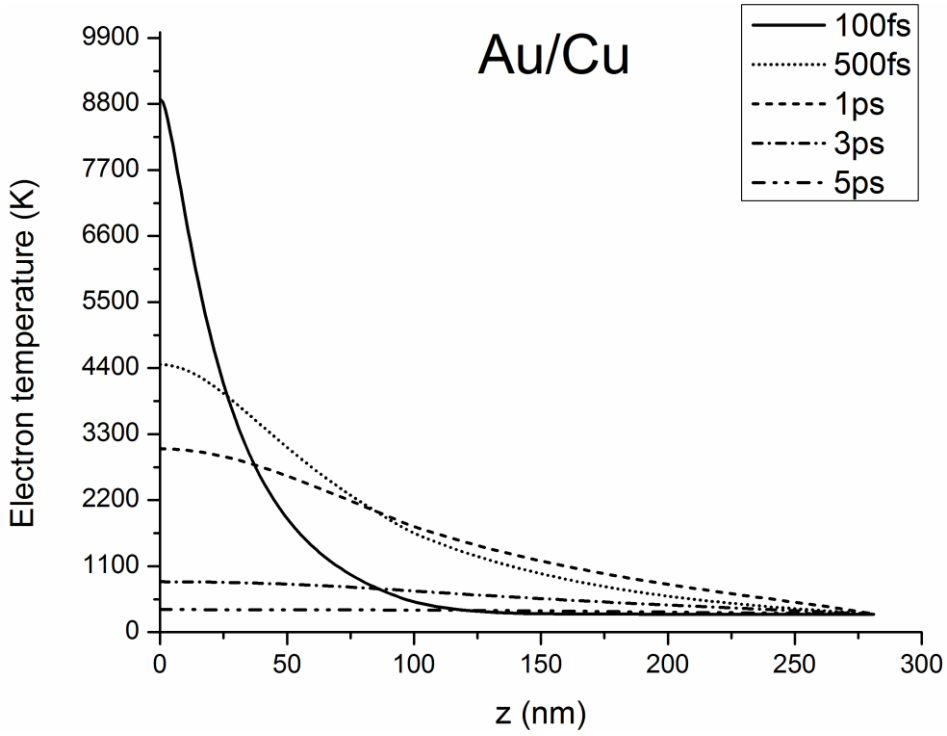

Figure 5.17 Spatial distribution of the electron temperature of double-layer films of Au/Cu at the center of the laser beam, 100 fs and 0.2 J/cm^2, at different times

The lattice temperature along z direction for Au/Cu assembly at the center of the laser beam of 100 fs and 0.2 J/cm2 at different times is shown in figure 5.18. The solid line represents the lattice temperature at 100 fs it shows that the maximum temperature was at the surface then it decreases gradually along the depth. After that the interface (at 100 nm) between the two layers shows a jump in the value of temperature and then it

decreases spatially again. Finally the interface temperature had a value higher than that at the surface. For example at 5 ps the lattice temperature at the surface was 378 K while it was 401 K at the interface.

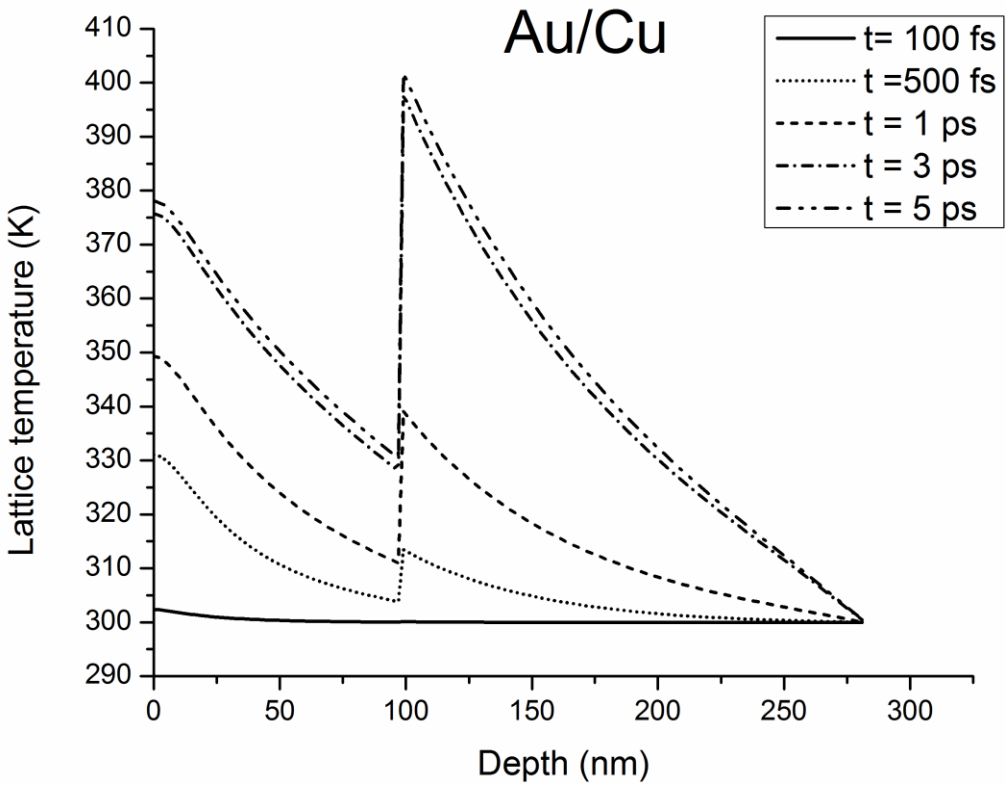

Figure 5.18 Spatial distribution of the lattice temperature of double-layer films of Au/Cu at the center of the laser beam, 100 fs and 0.2 J/cm^2, at different times

Figure 5.19 shows the temporal distribution of the surface electron temperature at the center of laser beam for Au/Cu, using both constant value of electron-phonon coupling factor (black line) and Chen's model (J. K. Chen, et al., 2005) (red line) in order to make a comparison between these two cases. As can be seen in this figure there is a little change in the electron temperature where using Chen's model leads to have higher value of electron temperature compared to the constant coupling factor.

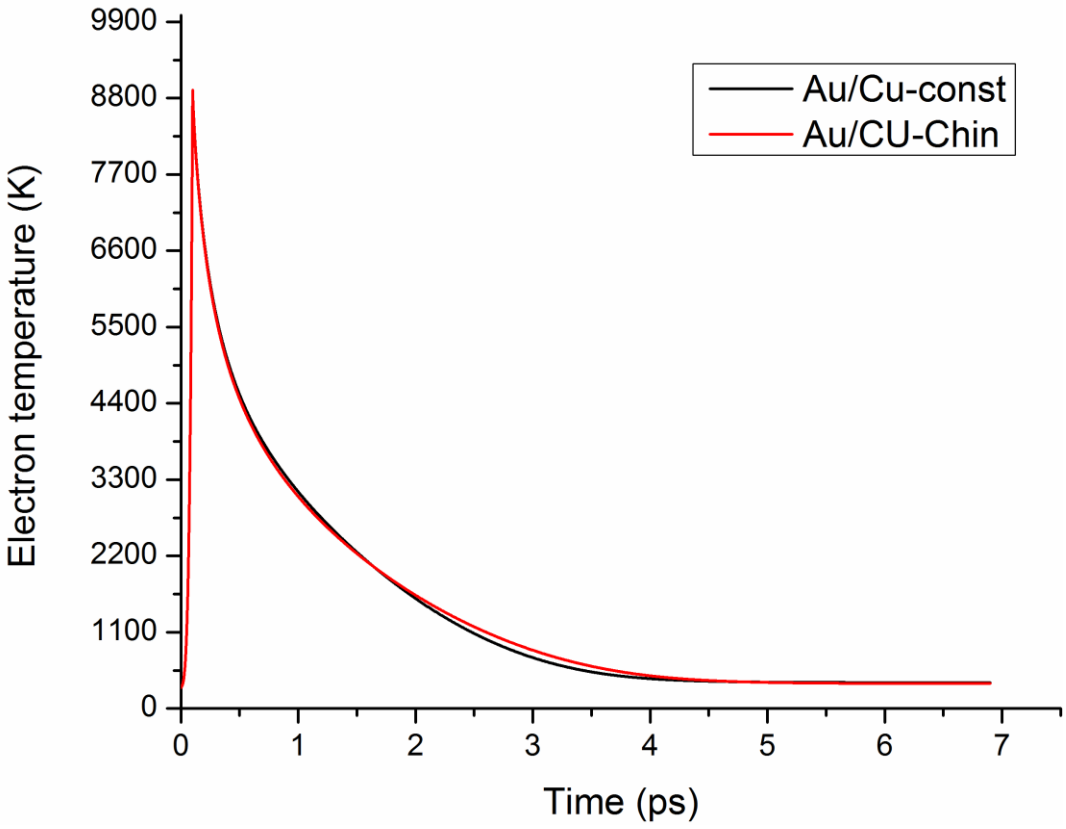

Figure 5.19 Temporal distribution of the surface electron temperature of Au/Cu at the center of the laser beam of 100 fs and 0.2 J/cm^2 in the case of constant and Chen model electron-phonon coupling factor

The temporal distribution of the surface lattice temperature at the center of the laser beam for Au/Cu is represented in figure 5.20 using both constant electron-phonon coupling factor and Chen's model. As can be seen there is a noticeable difference between the two cases, where Chen's model gives higher lattice temperature with time.

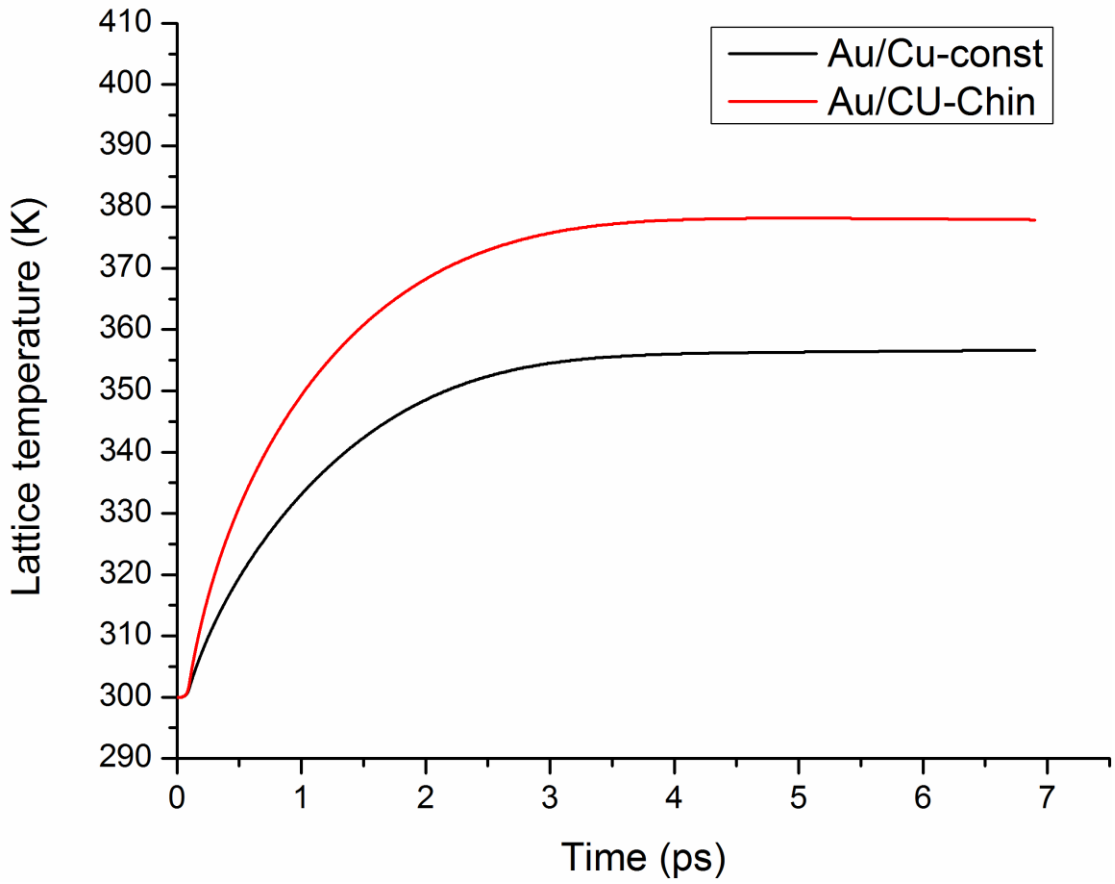

Figure 5.20 Temporal distribution of the surface lattice temperature of Au/Cu at the center of the laser beam of 100 fs and 0.2 J/cm^2 in the case of constant and Chen model electron-phonon coupling factor

The same results was found by F. Chen et al. (2011) This leads to conclude that the temperature dependent thermal properties must be taken into account in the case of ultrashort laser pulse irradiation (F. Chen, et al., 2011)

Conclusion

In this chapter the spatial and temporal thermal evolution through double-layer metal films irradiated by femtosecond laser pulse was studied using two-dimensional form of

the two-temperature model with temperature dependent thermal properties. Coating of 100 nm of gold was used as the top-layer of the assembly and both copper and aluminum were selected as substrates. The laser pulse duration of 100 fs with a fluence of 0.2 J/cm^2 and spot size of 50 μm was used. It was found that the thermal properties of the second layer play an important role in determining the thermal response of the first layer. Higher value of electron-phonon coupling factor of the substrate causes a remarkable reduction in the lattice temperature of the first layer compared to the single-layer target by acting as a heat sink as a result of the preferential coupling of the heat at the interface between the two layers, which can be noticed by a clear jump in the lattice temperature at the interface. It was found also that there is a negligible difference in the temporal and spatial distribution of the electron temperature between single gold film and double-layer films of both Au/Al and Au/Cu. Finally, the temperature dependent thermal properties must be taken into account for femtosecond laser heating for example using the temperature dependent coupling factor that is represented by Chen's model increases the thermal response of the target compared to using constant value.

CHAPTER SIX: EXPERIMENTAL INVESTIGATION OF FEMTOSECOND LASER ABLATION OF COPPER TARGET

Introduction

Femtosecond laser ablation has gained lots of attention over the last three decades as a technique for precise machining (Shirk & Molian, 1998). The ability of femtosecond laser for material removal with a minimal heat-affected zone gives this technique an advantage compared to the longer laser pulse ablation such as nanosecond laser (Pronko et al., 1994; Shirk & Molian, 1998). Moreover, the fact that the femtosecond laser interacts with materials in fast manner that even the laser produced plasma that comes at later time has no chance to interrupt the laser pulse (Shirk & Molian, 1998). Therefore, the laser pulse energy going to be deposited entirely in the exposed surface and the ablation is expected to be effective and optimum.

In the previous chapters of this thesis we reviewed the theoretical base of the femtosecond laser ablation mechanisms in general, and we have tried to develop a computer code to simulate the behavior of surface exposed to an ultrashort laser pulse. The results presented in these chapters include a parametric study that shows thermal response of copper exposed to an ultrashort laser pulses at various parameters. Some of these parameters that we tried to simulate were the effect of the laser pulse spot size and total pulse energy (fluence), reflectivity, and the thermal properties. The main goal of this

investigation is to perform a practical parametric study to benchmark our simulation results.

The practical investigations of the femtosecond laser ablation have started during the eighties of the last century. At that earlier time people noticed the main characteristic of the ultrashort laser ablation mechanism where optimum material removal without molten layer with lower ablation threshold has been reported. Kuper and Stuke (1987) investigated the ablation behavior of polymer exposed to femtosecond and nanosecond Excimer laser pulses at a wavelength of 248nm. Their main observation was the occurrence of laser induced ablation by femtosecond laser pulse at low fluence as five times lower than the ablation threshold of nanosecond laser pulse (Kiiper & Stuke, 1987). Also they noticed the advantage of the femtosecond laser pulses to create a smooth and well defined crater edges (Kiiper & Stuke, 1987). Similar study was also conducted by Ihlemann et al. (1991) who performed an experiment to compare the ablation behavior of fused silica exposed to femtosecond and nanosecond laser pulses at various wavelengths. The main observations were the impact of the laser wavelength on the ablation rate (Ihlemann, et al., 1991). In the comparison between the femtosecond and the nanosecond laser at the same wavelength, the nanosecond laser pulses exhibit higher ablation rate (Ihlemann, et al., 1991). Another important observation was the femtosecond laser created a smoother shaped holes in comparison with the nanosecond laser pulses (Ihlemann, et al., 1991). Perhaps due to the nature of the fused silica as a highly transparent and non-crystalline dielectric material, the superiority of the femtosecond laser pulses in ablation rate was not noticeable.

Several years later P. P. Pronko et al. (1994) showed the trend of increasing of ablation threshold with the pulse width. In their study they compared the ablation threshold of silicon samples ablated by different Ti:sapphire laser pulses that varies in width from 200 fs to 7 ns. (Pronko, et al., 1994). Despite the strong dependency of the ablation threshold on the laser pulse width, the ablation threshold did not show any increase within a range that extended from the femtosecond range to 1 ps (Pronko, et al., 1994). Thus, emphasize that in this range the mechanism of ablation is identical. On the other hand when the laser pulse is longer more contribution to heat conduction is expected, which helps to dissipate more heat deep under the surface and contribute to a relatively larger heat-affected zone, thicker molten layer and less ablated atoms. Also they highlighted the tendency of femtosecond laser to produce small crater size (Pronko, et al., 1994).

Then, Chicbkov et al. (1996) have reported a stunning scanning electron microscope (SEM) images for femtosecond laser ablation of several metallic targets. In their work, they compared the crater shape of drilled 100 μm thick steel target irradiated by multiple laser pulses (10^4) at various pulse width regimes (Chicbkov, et al., 1996). The effect of the molten layer formation and their evolution during the laser irradiation plays the most significant role in shaping the crater (Chicbkov, et al., 1996). In the nanosecond laser case the molten layer forms within the border of the crater flows vertically by the aid of the recoil vapor pressure and solidifies to end up as a solid columnar structure lining the side wall of the crater forming a “corona” structure (Chicbkov, et al., 1996). In the other case of shorter pulses such as 80ps, the molten layer forms and flows vertically with the

aid of the recoil vapor pressure and solidifies in place without moving to the side of the crater walls (Chicbkov, et al., 1996). On the other extreme, the case of ultrashort laser pulses at 100 fs, no molten layer is tend to be formed and metallic target expected to be drilled smoothly and precisely (Chicbkov, et al., 1996).

These early observations of the femtosecond laser ablation in the low fluence regime, and its advantages over the nanosecond laser pulses as a precise ablation technique encourage many other research groups around the world to do more studies in depth. S. Preuss et al. (1995) performed an experiment to measure the ablation threshold and the ablation rate of various metallic targets irradiated by 500 fs, 248 nm Excimer laser pulses (Preuss, et al., 1995). In their study, they tried to develop a simple model to estimate the ablation threshold and the ablation rate of various metals based on the thermal and optical properties of the irradiated surface (Preuss, et al., 1995). In their hypothesis they assumed the time is not enough for heat conduction in the case of ultrashort pulses exposure, so that all of the energy absorbed will be used for the ablation, the optical properties of the surface were used to determine the amounts of the energy absorbed and reflected during the interaction (Preuss, et al., 1995). The main contributor for the ablation threshold for certain materials after considering the optical properties was the latent heat of evaporation of that material at 298K. Their main assumption was the ablation will only occur once the total volume energy stored in the irradiated sample reach or exceed the evaporation enthalpy of that material (Preuss, et al., 1995). Their calculated value of ablation threshold has found to be underestimated for all of the tested elements. The degree of disagreement between the calculated and the measured value of ablation

threshold fluence were solely dependent on the material (Preuss, et al., 1995). Several studies (X. Liu, et al., 1997; Nolte et al., 1997; Preuss, et al., 1995) were also conducted by other groups and confirmed the primarily noticed characteristics of ultrashort pulse laser ablation in the near ablation threshold regime.

In 1996, Luft et al (1996) decided to test these advantages of ultrashort pulses in different way. They argued, since the main advantage of using ultrashort pulses is a high precision micromachining; let's test these advantages in a condition that is similar to a micromachining system by using very high fluence (to boost the productivity) and applying the irradiation in Air (not in vacuum system). They compared 700 J/cm^2 fluence each for copper vapor laser (50 fs pulse width) and Ti:sapphire laser (200 fs). Also they wanted to look at and compare the heat-affected zone produced by each laser and how far they are going to penetrate in the matrix around the laser pulse produced crater or hole (Luft, et al., 1996). In order to see the heat-affected zone, they have to use a heat sensitive material. They used a cold rolled copper samples, these samples were heat sensitive enough as any spike of heat within the metal matrix could trigger a recrystallization response (Luft, et al., 1996). A recrystallized region within a cold worked microstructure could be observed easily by examining a sectioned sample surface using optical or electronic microscope. In their results, they showed that at higher laser pulse fluence, the basic differences between the femtosecond and nanosecond ablation are not valid any more (Luft, et al., 1996). Femtosecond laser ablation was also noticed to exhibit thick molten layer formation and deep heat-affected zone (Luft, et al., 1996). After that, Sokolowski-Tinten et al. (1998) studied the transient nature of the material response after

irradiation by 120 fs laser pulse. In this study, they used ultrafast time resolved optical spectroscopy to generate micrographs of several metallic surfaces being exposed to ultrashort laser pulses (Sokolowski-Tinten, et al., 1998).

In a continuation to the theoretical studies of the ultrashort laser pulse interaction with metal, Perez and Lewis (2002), reported a result of molecular dynamic simulation for ultrashort pulse interaction with metals. According to their results, the mechanical fragmentation is a third possible mechanism for ablation. This mechanism is explained by the significant amount of stresses that can be stored in the irradiated surface during the laser pulse interaction(Perez & Lewis, 2002). Bukuk Oh et al. (2007) had compared a 2-D theoretical model of femtosecond laser ablation based on phase explosion with experimental results. Their results show a good agreement in terms of crater depth between their model and actual crater created by 150 fs laser pulses of Cu and Ni sample (Oh, et al., 2007). Their results emphasize that the phase explosion mechanism is the main contributor for the femtosecond laser ablation of metallic sample in the medium fluence regime (Oh, et al., 2007). Another interesting study for materials ablation by quadruple femtosecond laser pulses at various delay time between pulses was reported by Ihtesham et al. (2003) this study showed the advantage of quadruple of femtosecond laser pulses separated by 1 ns delay time between pulses in producing deeper crater in stainless steel, silicon and glass compared to the same fluence of laser pulses separated by 1 ms of delay (Ihtesham, Xianfan, et al., 2003).

Femtosecond and nanosecond laser ablation at ultraviolet wavelength had been compared by Zeng et al. (2004) in this investigation a third harmonic generator has been

used convert both the nanosecond and femtosecond laser wavelength from their fundamental wavelengths to 266nm. The results of this study show the superiority of the femtosecond laser pulse to induce deeper crater compared to nanosecond laser at the same fluence (Zeng, et al., 2004) of around (11 J/cm^2). The plasma expansion due to laser irradiation in atmospheric pressure was also studied (Zeng, et al., 2004). The results show that the plasma expansion due to femtosecond laser irradiation was noticed to be directed in one direction while the plasma expansion due to nanosecond laser pulses was observed to be isotropic (Zeng, et al., 2004). Another interesting results for a comparison between femtosecond and nanosecond laser pulses ablation of thin film was reported by Meunier et al. (2009) in their studies they compared the surface modification induced by single laser pulse irradiation of Aluminum nitride film coted on sapphire substrate (Meunier, et al., 2009). Also they studied the effect of surface oxygen content on the ablation threshold. Their results showed the influence of nanosecond laser pulse in producing large heat-affected zone. This zone was denoted by a large radius of film color changes around the laser induced crater (Meunier, et al., 2009). On the other hand the femtosecond laser shows a gentle ablation without film color changes around the ablated crater. Also the laser ablation threshold was found to be independent on the surface oxygen content in the case of femtosecond laser irradiation (Meunier, et al., 2009). The opposite trend was noticed in the case of ns laser pulse irradiation where the surface oxygen content influenced the nanosecond laser ablation threshold (Meunier, et al., 2009). This influence was connected with the shift of the band gab of the AlN created by film oxygen content (Meunier, et al., 2009). This phenomenon shed the light on the importance of the ionization process in the ns laser ablation mechanism.

As descried in details in chapter 2 through 5 in this thesis, a two-dimensional numerical code to solve the heat transfer equation based on the two-temperature model has been developed. This model was also used to evaluate the temperature distribution and the ablated depth of various materials irradiated by ultrashort lase pulse. The main goal of using the TTM is due to its ability to deal with the ultrafast heat transfer scenario related to ultrafast laser pulse irradiation of surfaces by considering the calculation of electron and phonon temperatures and the energy transport between the electrons and the lattice subsystems. It is found that the time required for reaching the equilibrium between the electron and lattice temperatures depend on both the materials thermal properties and the irradiation conditions. In general, the time required for reaching the equilibrium for most of the materials is in the order of several picoseconds. Coupling our simulation results to experimental investigation is so vital to validate our modeling approach. In this chapter reported the experimental investigations that have been performed to study femtosecond laser ablation of copper target.

Experimental Setup

This investigation was conducted in our will equipped facility at the Center for Materials Under eXtreme Environment (CMUXE) at Purdue University. The main laser facilities intended to be used is the femtosecond laser facility in the High Energy Density Physics laboratory (HEDP Lab). This lab is equipped with a Ti:Sapphire femtosecond laser system which produces a minimum of 40 fs laser pulses at 800 nm wavelength. The femtosecond laser system uses a mode-locked Ti:Sapphire oscillator (Synergy,

Femtolase, Inc.) and a chirped pulse amplifier (Amplitude Technology, Inc.) to produce a laser pulses that can be varied in width up to hundreds of picoseconds.

A set of copper target were prepared (mechanically polished) and irradiated by multiple 40 fs laser pulses at various pulse energy. At each energy the same target spot was irradiated by 10 pulses of laser to increase the depth of laser-produced crater. This approach of multiple laser pulses was used to create a crater that is deeper than the surface morphology fluctuation due to surface roughness. The laser pulse spot size was fixed at 30 μm for all cases. For some selected pulse energies, the effect of crater depth versus number of pulses were studied by shooting various number laser pulses at different spots and measuring the produced crater depths.

The post irradiated samples were evaluated quantitatively and qualitatively by using the Atomic Force Microscope (AFM) and the Scanning Electron Microscope (SEM) respectively. An example of the use of these microscopy techniques is presented in figure 6.1 the SEM image shown in figure 6.1-a shows the surface modification caused by 10 laser pulses. Although SEM image is very good in showing the modified surface features, this technique cannot provide a precise measurement of the crater depth. AFM can provide a 3-D presentation of the modified surface with a very precise height measurement capability (fractions of nm). AFM image of a surface modified by 10 pulses of laser is shown in figure 6.1-b. a two-dimensional crater profiles sections can be extracted from the AFM images as shown in figure 6.1-c. this section is very useful and it can be directly compared with our simulation results.

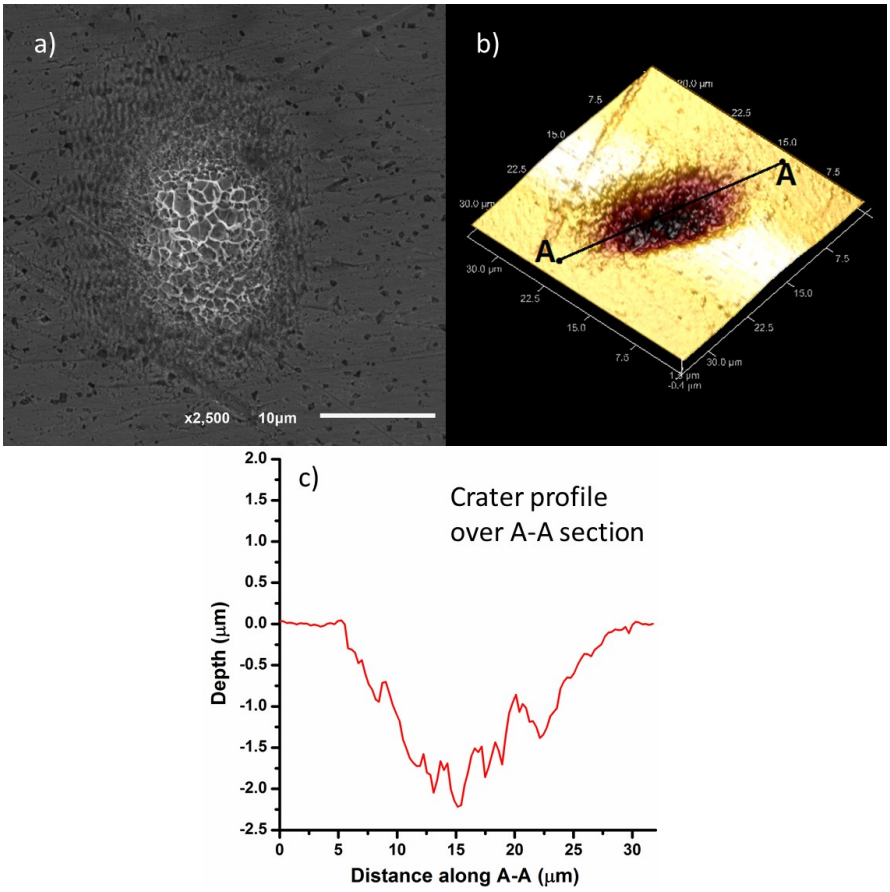

Figure 6.1 An example for the qualitative and the quantitative evaluation of the laser produced crater used in this study

Results and Discussion

Pure copper sample were mechanically polished and irradiated by ultrashort (40 fs) pulses of T:Sapphire laser at 800 nm wavelength. Each spot was shot by 10 pulses. The experiment was repeated by varying the total pulse energy for each spot. The laser pulses were focused to 30 µm spot size on the sample surface. The selected pulse energies designed to span a laser fluence range from 8.2 J/cm^2 to 0.14 J/cm^2. Figure 6.2 shows SEM images of the irradiated Cu targets. As it can be seen in this figure, the laser

irradiation caused a noticeable spots on the target surface. We also have noticed a shrink in the size of the laser produced surface spots as the laser pulse energy decrease. 58 μJ pulses caused around 20 μm surface spots (crater), while 5 μJ pulses caused a surface spot that is less than 10 μm in size. The reason behind this variation in laser produced spot size is the Gaussian nature of the spatial profile of the laser pulse. At high pulse energy bigger part of the laser pulse will have enough fluence to cause ablation or surface modification and that will result in a bigger crater diameter. We also have noticed what it appears to be melting and re-solidification of part of the surface is it can be clearly seen in the higher energy pulses.

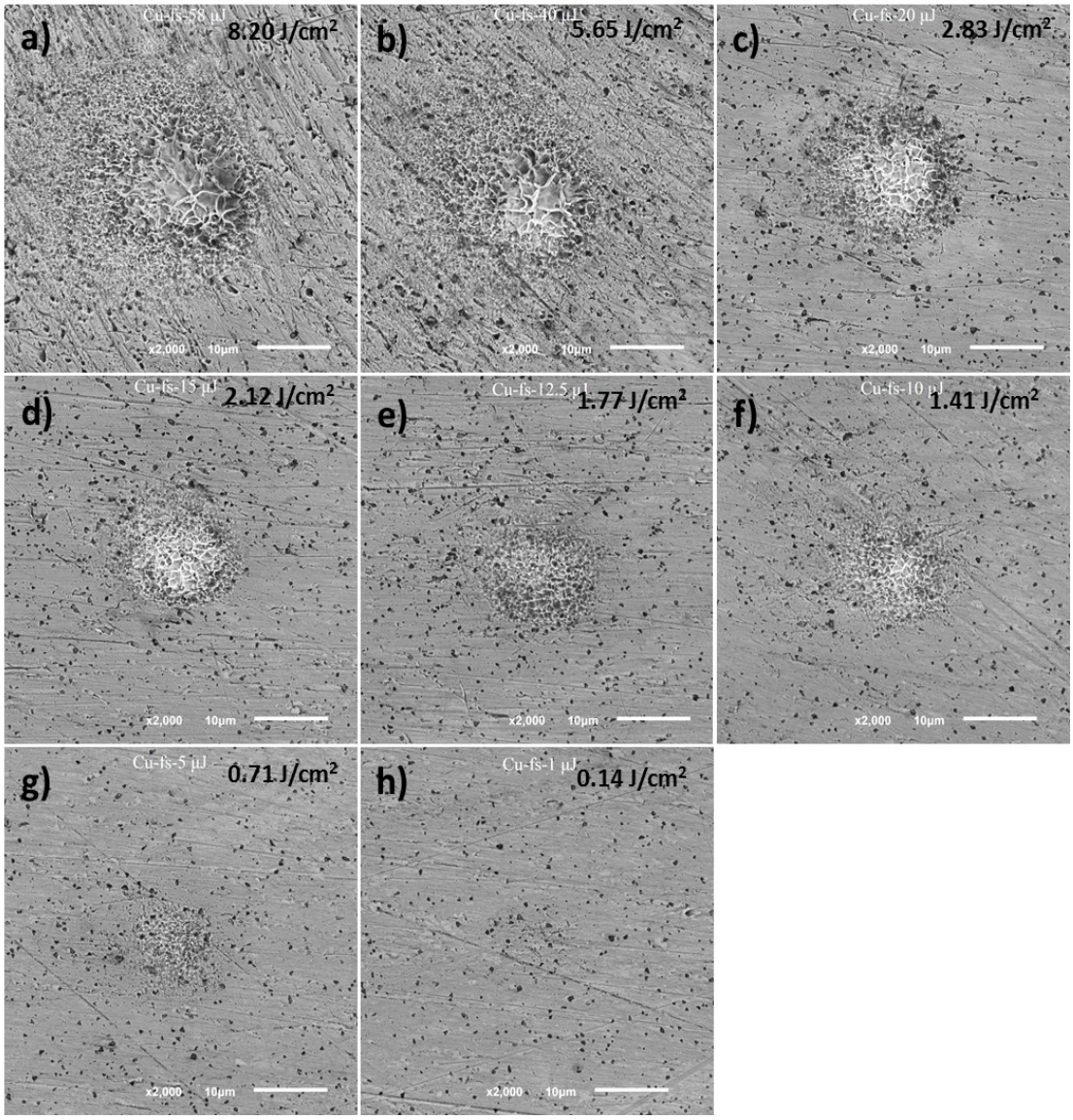

Figure 6.2 SEM images of the surface craters produced by irradiating 10 pulses of (40 fs) T:sapphire (800 nm) laser on Cu target, laser spot size was fixed at 30µm. Images from (a) to (h) shows the effect of different laser pulse energies

The laser produced surface craters shown in figure 6.2 were reanalyzed by AFM. A two-dimensional craters profile was extracted from the AFM images. Figure 6.3 shows 4 different profiles for craters produced by different pulse energies. Figure 6.3-a shows the profile of the target surface that was shot by 10 pulses of 1 µJ of fs laser (0.14 J/cm^2). In

this case of pulse energy, no material removal was seen. Increasing the laser pulse energy to 10 μJ result in noticeable ablation as shown in figure 6.3-b. the amount of ablated materials was further increased by increasing the laser pulse energy to 20 μJ and 58 μJ as shown in figure 6.3-c and d respectively.

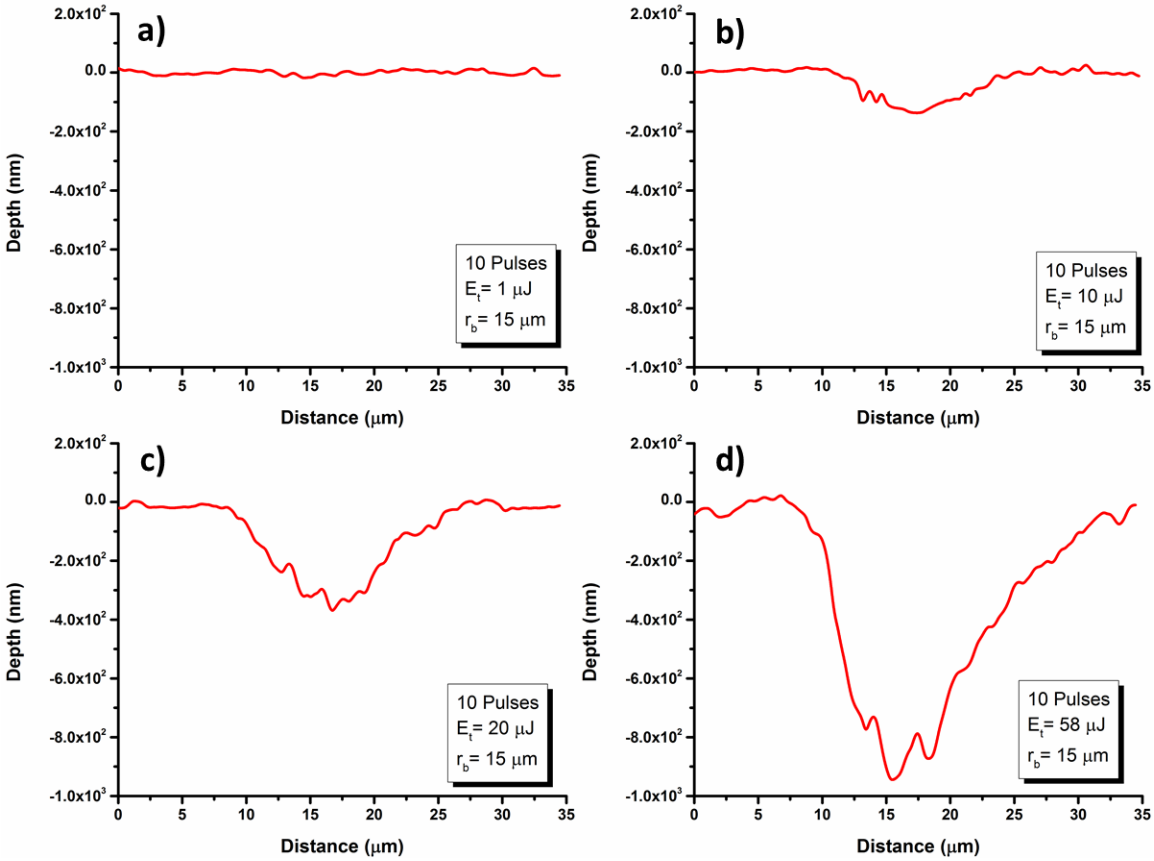

Figure 6.3 Surface craters profiles extracted from AFM images of craters produced by irradiating 10 pulses of (40 fs) T:sapphire (800 nm) laser on Cu target, laser spot size was fixed at 30μm. Images from (a) to (d) shows the effect of different laser pulse energies

The areas under the crater profiles shown in figure 6.3 can be used as a good indication of the ablated volume or mass. Plotting these ablated areas versus the laser fluence will be useful in determination the minimum laser fluence that can cause material

ablation (ablation threshold) indicate. The areas under the laser produced craters profiles were measured for all 8 cases of different laser pulse energies shown in figure 6.2. The plot of these values versus the corresponding laser fluence of each case is presented in figure 6.4-a. as can be seen in this figure, a sudden jump in the trend of ablated volume versus fluence was found at a laser fluence value between (2.1 and 2.8) J/cm^2. Below and above this sudden increase the ablated mass was found to be linearly proportional to laser fluence. A one reason might be valid in explaining this sudden change is the difference in the dominant ablation mechanisms in these two fluence regimes. A new ablation mechanism such as phase expulsion might be dominant at ablation fluence above 2 J/cm^2, which can cause a jump in the ablated mass above certain fluence. The linear trend of ablated volume versus fluence below (2.2 J/cm^2) was used to predict the ablation threshold. Figure 6.4-b shows the linear trend of this fluence range. Extrapolating the linear function that fits the data gives an ablation threshold at (0.45 J/cm^2). This value of the ablation threshold of copper found to be in a good agreement with our simulation results (Chapter 4).

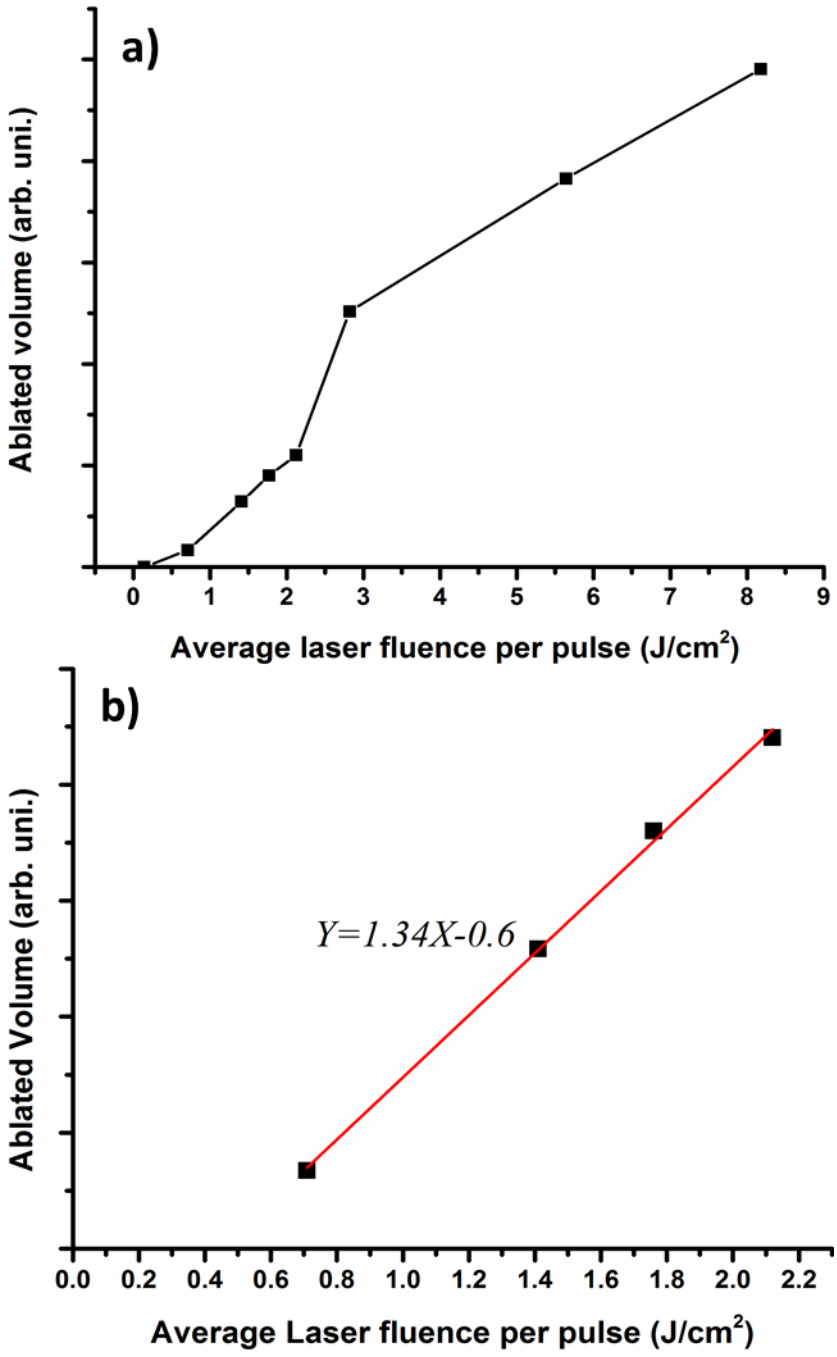

Figure 6.4 Plot of the ablated volume vs. average laser pulse fluence, the data was extracted AFM images of craters produced by irradiating 10 pulses of (40 fs) T:sapphire (800 nm) laser on Cu target, laser spot size was fixed at 30μm. The general trend is shown in (a) and the linear trend of ablated volume vs. low fluence laser pulses shown in (b)

The next step is to directly compare the crater profile produced by the femtosecond laser pulse ablation as predicted by the simulation results and the crater profiles obtained by the experiments. It is worthwhile to mention that the craters obtained experimentally were obtained from 10 pulses irradiation while the simulation result predicted the crater after one pulse irradiation. For the sake of direct comparison between the experimental and simulation results, the effect of multiple laser shots on the crater depth and shape was studied. For this purpose, a series of surface craters were produced by irradiating different regions of Cu target by various number of laser pulses, all at the same pulse energy (20 μJ). Figure 6.5 shows SEM images of the craters produced by varying the number of laser pluses. Two main observations were noticed in the shape of the craters at large number of pulses. The first observation is disappearance of the re-solidified materials at higher number of pulses. Also at higher number of pulses, the craters walls appears to be clean and much smother compared to what have seen earlier in the case of 10 pulses irradiation. The second observation is the formation of a nanostructure surrounding the edges of the crater appears in the case where high number of pulses was applied.

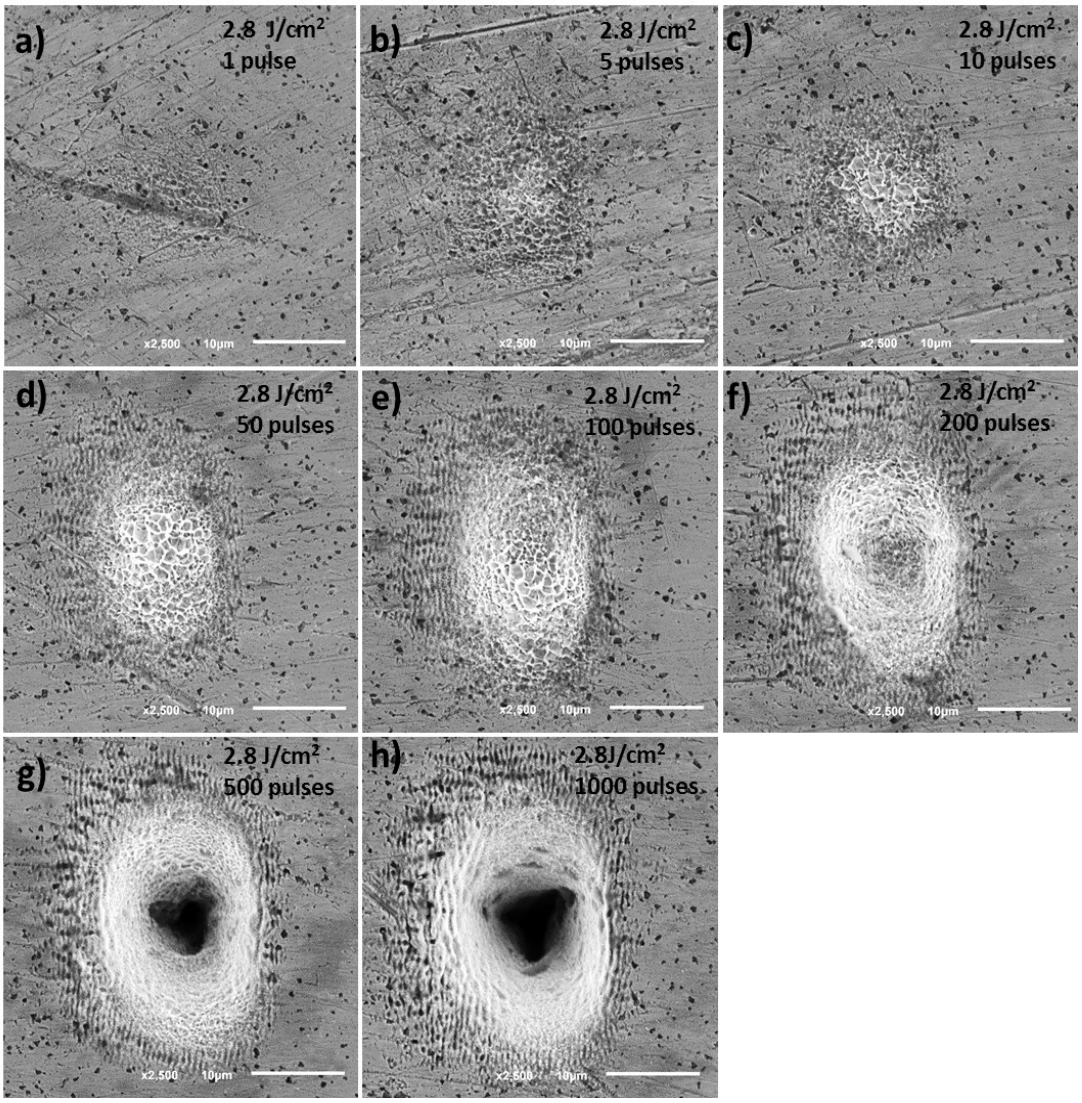

Figure 6.5 SEM images of the surface craters produced by irradiating various number of pulses of (40 fs) T:sapphire (800 nm) and (20μJ/pulse) laser on Cu target, laser spot size was fixed at 30 μm

AFM was used to examine the craters shown in figure 6.5 due to the fact that the AFM has a very limited depth measurement range, AFM was not able to show the images of the craters produced by large number pulses (200 pulses and above). So that we relied on the craters produced by (1, 10, 20, 50, and 100 pulses) to study the effect of number of

laser pulses on the crater depth. Figure 6.7 shows some of the AFM extracted crater profiles produced by varying the number of laser pulses

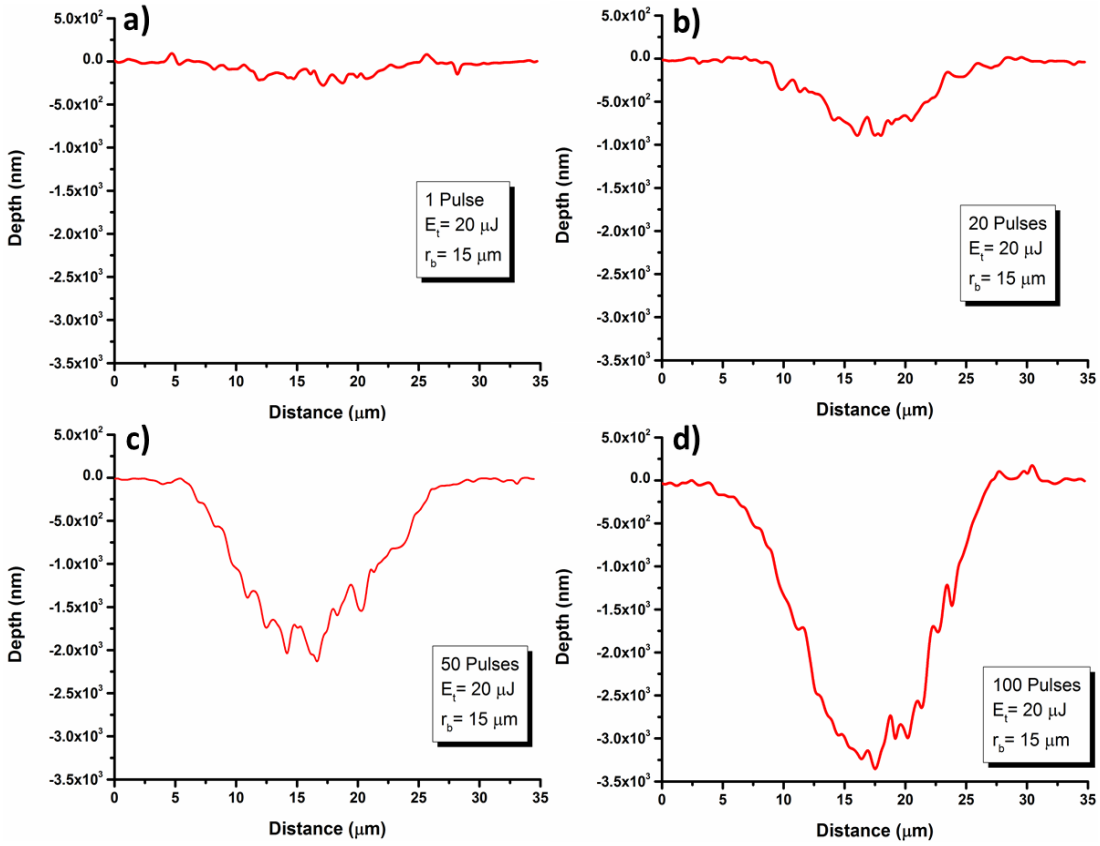

Figure 6.6 Surface craters profiles extracted from AFM images of craters produced by irradiating various number of pulses of (40 fs) T:sapphire (800 nm) and (20µJ/pulse) laser on Cu target, at a laser spot size of 30 µm

The maximum depth of the craters shown in figure 6.5 (a) through (e) were plotted versus number of laser pulses and presented in figure 6.7. As can be seen in this figure, the maximum craters depth shows a linear trend of increase in response to the increase in

number of laser pulses. It was found that the crater depth increased approximately by factor of three when the number of laser pulses increased from 1 pulse to 10 pulses.

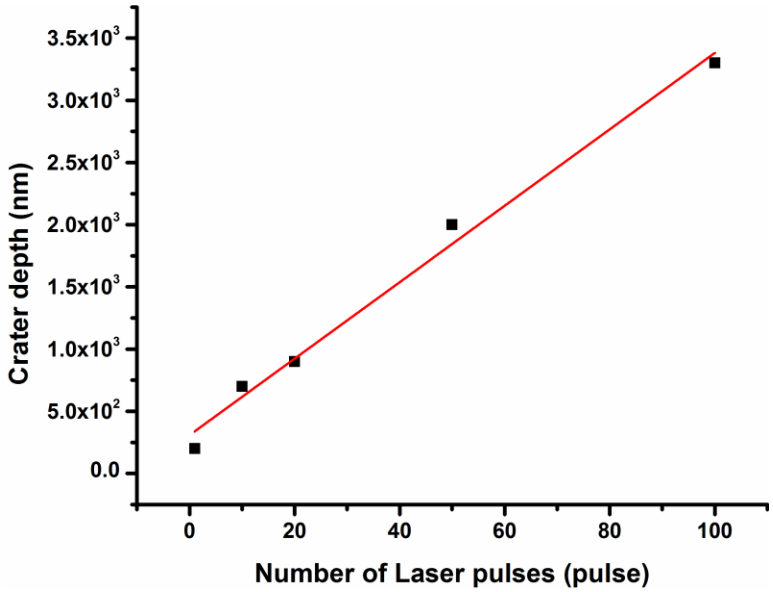

Figure 6.7 Plot of the maximum crater depth vs number of laser pulses, the data was extracted from AFM images of craters produced by irradiating various pulses of (40 fs) T:sapphire (800 nm) and (20 μJ/pulse) laser on Cu target, laser spot size was fixed at 30 μm

The craters profiles produced experimentally by 10 pulses of laser were divided by 3 (i.e., 10 pulses to 1 pulse correction) and compared with our simulation result. Figure 6.8 presents a direct comparison between the simulation and the experimental results for three different pulse energies. As can be seen in figure 6.8-a and b, our simulation results have reasonable agreement with the experimental data in terms of crater depth and diameter. There is an obvious discrepancy between the experimental and the simulation results in crater shape. In the case of low pulse energy (Fig. 6.8-c) both simulation and experimental results shows no ablation.

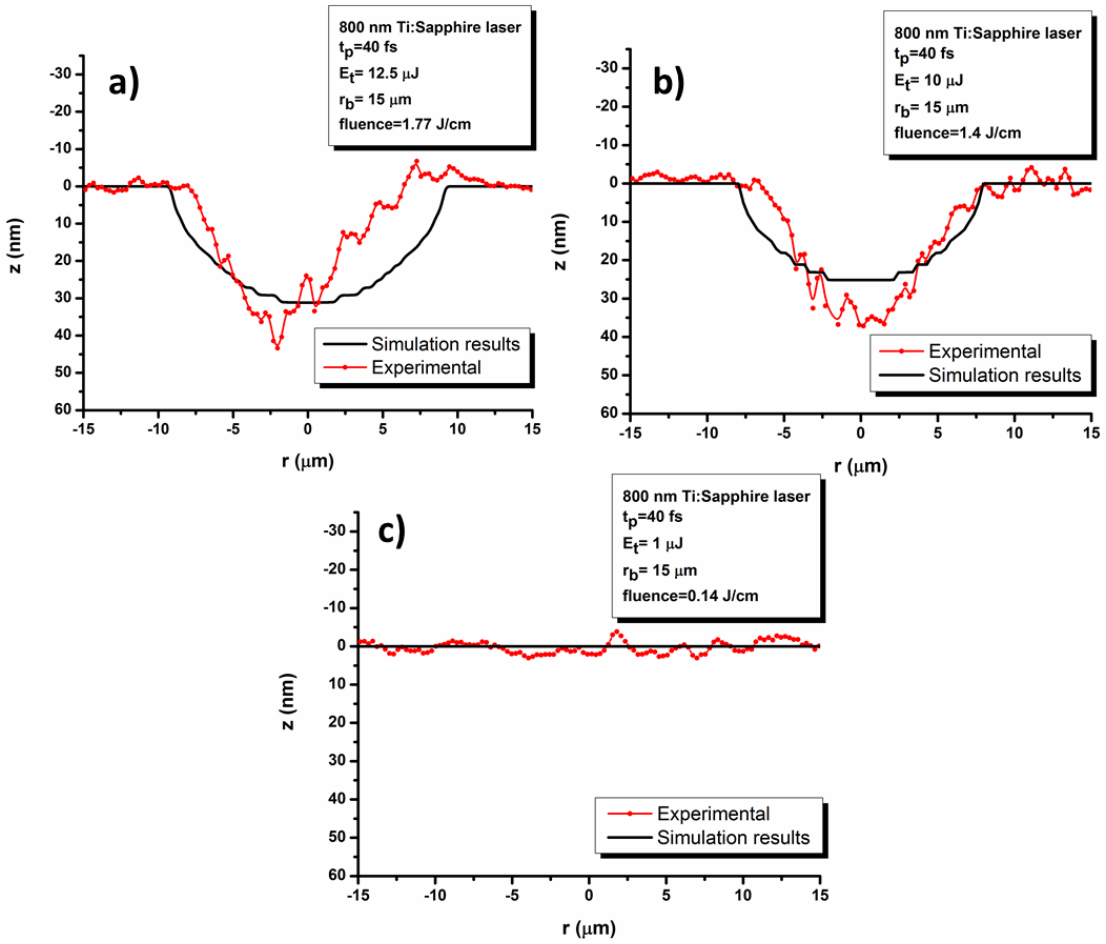

Figure 6.8 A direct comparison between the simulation and the experimental results for three different pulse energies with R=0.7

Conclusion

In an attempt to validate the simulation results for femtosecond laser ablation of copper target, a pure copper sample were mechanically polished and irradiated by ultrashort (40 fs) pulses of T:Sapphire laser at 800 nm wavelength. The laser produced surface craters were reanalyzed by SEM and AFM microscopy. A two-dimensional crater profiles extracted from the AFM images were used to evaluate the ablated volume in response to the laser irradiation. The linear trend of ablated volume versus fluence below

(2.2 J/cm^2) was used to predict the ablation threshold. The ablation threshold for Cu by 40fs laser was found to be (0.45 J/cm^2). This value of the ablation threshold of copper found to be in a good agreement with the simulation results (Chapter 4). This value was obtained by extrapolating the linear function that fit the data of the ablated volume versus laser fluence. The effect of multiple laser shots on the crater depth and shape were studied. At large number of laser pulses irradiation, the re-solidified materials that was noticed in the case of 10 pulses irradiation was found to be disappeared and the craters walls appears to be clean and much smother. Formation of a nanostructure surrounding the edges of the crater appears in the case where high numbers of pulses were applied. It was found that the crater depth increased approximately by factor of three when the number of laser pulses increased from 1 pulse to 10 pulses. Our simulation results show a reasonable agreement with experimental data in terms of prediction the crater depth and diameter. There is an obvious discrepancy between the experimental and the simulation results in crater shape. In the case of low pulse energy (below 0.4 J/cm^2), both simulation and experimental results shows no ablation.

CHAPTER SEVEN: SUMMARY AND CONCULUSIONS

In this work the parabolic form of the two-step temperature model was developed and used to study the non- thermal equilibrium two-dimensional heat distribution when metal targets are irradiated by femtosecond laser pulse with temperature and phase dependent thermal properties. Gaussian temporal and spatial distributions of laser power density were chosen. The behavior of the calculated temporal and spatial temperature distribution of the electron and the lattice was explained by the physics of the heat exchange mechanisms among electrons, photons, and lattice atoms. The electrons absorb the energy from the photons spontaneously then transfer the energy to the lattice system according to electron-phonon coupling mechanism. The impact of the spot size of the femtosecond laser beam was studied, and it was found that larger spot size for a fixed total energy leads to smaller maximum power density so less heat deposited to the material and finally lower equilibrium temperature. It was found that rate of interaction between the electrons and the lattice is influenced by the electron-phonon coupling factor, as the coupling factor increase the thermal equilibrium can be achieved earlier. The impact of the reflectivity was studied and that higher value of reflectivity leads to high rate of photons reflection and less absorption of the energy in the target.

After that the ablation of copper target irradiated by ultrashort laser pulses was studied by estimating the crater shape and size and the ablated mass using thermal

evaporation and phase explosion mechanisms. The ablation by the thermal evaporation can be estimated by calculating the surface recession velocity, which is a function of surface temperature, vapor pressure, and the latent heat of vaporization. The phase explosion mechanism is characterized by the sudden explosive ejection of gas and superheated liquid droplets as a result of extremely high power density absorbed in ultrashort time, this mechanism is considered as the main mechanism of the ablation by the ultrashort laser pulse interaction with material target. For this mechanism any target material reaches the temperature of 90% of thermodynamic critical temperature was eliminated and then accounted for the ablation depth. The impact of the total energy and the spot radius on the ablation was studied. It was found that when the ablation increases as the total energy increases because the heat that is deposited and absorbed increases, also as the spot size increases the absorbed heat flux decreases and that lowers ablated material.

The impact of the electron temperature dependent electron-phonon coupling factor and the electron heat capacity on the thermal evolution of the copper target irradiated by the femtosecond laser pulses was studied. The first model that is used for the electron-phonon coupling is the Lin's models, in this model the calculations of the electronic structure of the density of state have been done at high electron temperature and the excitation of the d band electrons and their contribution to the coupling of the heat between electrons and phonons was taken into account. The second model was the Chen's model, in which the electron-electron collisions and electron-lattice collision rates calculations were performed. The two models were compared to the commonly used constant values for the electron-phonon coupling factor. It was found that the rate of

coupling of the heat from electrons to the lattice subsystems increases when these models are used, this because the electron-phonon coupling factor increases as the electron temperature increases leading to fasten the coupling rate. It was observed also that at high fluence the thermalization time when these models were used approaches to the fixed value regardless of the fluence while it kept increasing with the fluence when constant value of the coupling factor was used as reported by lee et al. (2011), and this is another reason that lead us to conclude that temperature dependent electron-phonon coupling must be taken into account. The comparison between the Lin's model of the electron heat capacity based on the density of state calculation and the well-known linear relationship between the electron heat capacity and the electron temperature was presented. It was found that the electron heat capacity that is calculated from the Lin's model is higher than that is calculated by using the linear formula, that caused a noticeable decrease in the electron temperature when the Lin's model was used hence the thermalization time increases.

The ultrashort laser interaction with double-layer metal films was studied numerically using the two-temperature model for both layers. 100 nm of gold was used as a top-layer of the assembly and both copper and aluminum were selected to use as substrates. It was found that the thermal properties of the substrate determine the thermal response of the first layer. For example, the higher value of electron-phonon coupling factor of the substrate leads to the reduction in the lattice temperature of the first layer compared to the single-layer target because of the preferential coupling of the heat that occurs at the

interface between the two layers which was observed from the results of high values of the lattice temperature at the interface.

In order to validate the simulation results of the thermal response and the corresponding ablation of the copper target irradiated by femtosecond laser some experiments have been done. In this practical study a set of copper samples was irradiated by femtosecond laser pulses of T:Sapphire laser at 800 nm wavelength. The laser produced surface craters were reanalyzed by SEM and AFM microscopy. The ablation threshold for Copper by 40fs laser was found to be 0.45 J/cm^2. This value of the ablation threshold of copper found to be in a good agreement with the simulation results. The relationship between the number of pulses and the ablation depth was investigated. It was found that the crater depth increased by a factor of three when the number of laser pulses increased from 1 pulse to 10 pulses. The experimental data of the ablated depth and the crater shape show almost a reasonable agreement with the simulation results.

Finally, it is recommended to study in more details the impact of the reflectivity as a function of target temperature, phase, and the wavelength of the laser beam. It is also recommended to study other possible ablation models and compare with this work and with experimental results. Special experiments can also be designed with various short pulse lengths to investigate the transition and domination of specific ablation mechanisms. In addition, it will be useful if several types of material targets can be studied, for example dielectric versus semiconductor material, noble metals versus transition metals, heavy metals versus light metals…etc.

LIST OF REFERENCES

LIST OF REFERENCES

Afanasiev, Y. V., Chichkov, B. N., Demchenko, N. N., Isakov, V. A., & Zavestovskaya, I. N. (2000). Extended two-temperature model of laser ablation of metals. *Proc. of SPIE, 4065*, 349.

Al-Malkawi, G., & Hassanein, A. (2013). Non-equilibrium two-dimensional thermal evolutions in target materials irradiated by femtosecond laser pulse. *Laser and Particle Beams, 32*(01), 33-39.

Al-Nimr, M. A., & Arpacib, V. S. (2000). The thermal behavior of thin metal films in the hyperbolic two-step model. *International Journal of Heat and Mass Transfer, 43*, 2021-2028.

Anisimov, S. I., Kapeliovich, B. L., & Perel'man, T. L. (1974). Electron emission from metal surfaces exposed to ultrashort laser pulses. *Soviet Physics JETP, 39*(2), 375-377.

Anisimov, s. I., & Rethfeld, B. (1997). THEORY OF ULTRASHORT LASER PULSE INTERACTION WITH A METAL. *SPIE proc., 3093*.

Ashcroft, N., & Mermin, D. (1976). *Solid State Physics*. New York.

Bulgakova, N. M., & Bulgakov, A. V. (2001). Pulsed laser ablation of solids: transition from normal vaporization to phase explosion. *Applied Physics A Materials Science & Processing, 73*(2), 199-208.

Bulgakovaa, N. M., & Bourakov, I. M. (2002). Phase explosion under ultrashort pulsed laser ablation: modeling with analysis of metastable state of melt. *Applied Surface Science, 197-198*, 41.

Changrui, C., & Chowdhury, I. H. (2004). Molecular Dynamics Study of Phase Change Mechanisms During Femtosecond Laser Ablation. *Journal of Heat Transfer, 126*(5), 8p.

Chen, A. M., Jiang, Y. F., Sui, L. Z., Ding, D. J., Liu, H., & Jin, M. X. (2011). Thermal behavior of thin metal films irradiated by shaped femtosecond pulse sequences laser. *Optics Communications, 284*(8), 2192-2197.

Chen, A. M., Jiang, Y. F., Sui, L. Z., Liu, H., Jin, M. X., & Ding, D. J. (2011). Thermal analysis of double-layer metal films during femtosecond laser heating. *Journal of Optics, 13*(5), 055503.

Chen, A. M., Xu, H. F., Jiang, Y. F., Sui, L. Z., Ding, D. J., Liu, H., et al. (2010). Modeling of femtosecond laser damage threshold on the two-layer metal films. *Applied Surface Science, 257*(5), 1678-1683.

Chen, F., Du, G., Yang, Q., Si, J., & Hou, H. (2011). Ultrafast Heating Characteristics in Multi-Layer Metal Film Assembly Under Femtosecond Laser Pulses Irradiation.

In A. Ahsan (Ed.), *Two Phase Flow, Phase Change and Numerical Modeling* (pp. 584).

Chen, J. K., & Beraun, J. E. (2001). Numerical Study of Ultrashort Laser Pulse Interactions with Metal Films. *Numerical Heat Transfer A, 40*(1), 1-20.

Chen, J. K., & Beraun, J. E. (2003). Modelling of ultrashort laser ablation of gold films in vacuum. *J. Opt. A: Pure Appl. Opt., 5*, 168.

Chen, J. K., Beraun, J. E., & Tham, C. L. (2003). Investigation of thermal response caused by pulse laser heating. *Numerical heat transfer, Part A, 44*, 705.

Chen, J. K., Latham, W. P., & Beraun, J. E. (2005). The role of electron–phonon coupling in ultrafast laser heating. *Journal of Laser Applications, 17*(1), 63.

Chicbkov, B. N., Momma, C., Nolte, S., Alvensleben, F., & Tiinnermann, A. (1996). Femtosecond, picosecond and nanosecond laser ablation of solids. *Appl. Phys. A, 63*, 109.

Colombier, J., Combis, P., Bonneau, F., Le Harzic, R., & Audouard, E. (2005). Hydrodynamic simulations of metal ablation by femtosecond laser irradiation. *Physical Review B, 71*(16).

Electron-Phonon Coupling and Electron Heat Capacity in Metals at High Electron Temperatures. (April, 2012). from www.faculty.virginia.edu/CompMat/electron-phonon-coupling/

Fang, R., Zhang, D., Wei, H., Li, Z., Yang, F., & Gao, Y. (2010). Improved two-temperature model and its application in femtosecond laser ablation of metal target. *Laser and Particle Beams, 28*(01), 157-164.

Fang, R., Zhang, D., Wei, H., Li, Z., Yang, F., & Tan, X. (2008). Effect of Pulse Width and Fluence of Femtosecond Laser on Electron-Phonon Relaxation Time. *Chinese Physics Letters, 25*(10), 3716-3719.

Furusawa, K., Takahashi, K., Cho, S.-H., Kumagai, H., Midorikawa, K., & Obara, M. (2000). Femtosecond laser micromachining of TiO_2 crystal surface for robust optical catalyst. *Journal of Applied Physics, 87*(4), 1604-1609.

Gamaly, E., Madsen, N., Duering, M., Rode, A., Kolev, V., & Luther-Davies, B. (2005). Ablation of metals with picosecond laser pulses: Evidence of long-lived nonequilibrium conditions at the surface. *Physical Review B, 71*(17).

Gamaly, E. G., Rode, A. V., Luther-Davies, B., & Tikhonchuk, V. T. (2002). Ablation of solids by femtosecond lasers: Ablation mechanism and ablation thresholds for metals and dielectrics. *Physics of Plasmas, 9*(3), 949.

Gao, X., Song, X.-W., & Lin, J.-Q. (2011). Thermal characteristics of double-layer thin film target ablated by femtosecond laser pulses. *Chinese Physics B, 20*(2), 024210.

Gragossian, A., Tavassoli, S. H., & Shokri, B. (2009). Laser ablation of aluminum from normal evaporation to phase explosion. *Journal of Applied Physics, 105*(10), 103304.

Grimvall , G. (1976). The Electron-Phonon Interaction in Normal Metals *Physica Scripta, 14*.

Gurevich, E. L., Kittel, S., & Hergenröder, R. (2012). Experimental and numerical study of surface alloying by femtosecond laser radiation. *Applied Surface Science, 258*(7), 2576-2579.

Hassanein, A. (1996). Disruption damage to plasma-facing components from various plasma instabilities. *Fusion Technology, 30*(3), 713-719.

Hassanein, A. M. (1983). *Modeling the interaction of high power ion or electron beams with solid target materials*.

Hess, H. (1998). Critical Data and Vapor Pressures for Aluminium and Copper. *89*.

Hirayama, Y., & Obara, M. (2005). Heat-affected zone and ablation rate of copper ablated with femtosecond laser. *Journal of Applied Physics, 97*(6), 064903.

Ho, C.-Y., Shih, C.-S., Hung, K.-M., Ma, C., & Lin, S.-Y. (2012). A Model for Femtosecond-Laser-Pulse Ablation of Metal Thin Films. *Chinese Journal of Physics, 50*(6), 939.

Hopkins, P. E., & Norris, P. M. (2007). Substrate influence in electron–phonon coupling measurements in thin Au films. *Applied Surface Science, 253*(15), 6289-6294.

Horng, H. E. (1984). Low Temperature Specific Heat of The Ternary Superconductor Lu Ru B2. *CHiNESE jOURNAL OF PHYSiCS, 22*.

Hu, H.-F., Ji, Y., Hu, Y., Ding, X.-Y., Liu, X.-W., Guo, J.-H., et al. (2011). Thermal analysis of intense femtosecond laser ablation of aluminum. *Chinese Physics B, 20*(4), 044204.

Huang, J., Zhang, Y., & Chen, J. K. (2009). Ultrafast solid–liquid–vapor phase change in a thin gold film irradiated by multiple femtosecond laser pulses. *International Journal of Heat and Mass Transfer, 52*(13-14), 3091-3100.

Huttner, B. (2009). Femtosecond Laser Pulse Interactions with Metals. *Springer Series in Materials science, 119*, 315-337.

Hwang, D. J., Chimmalgi, A., & Grigoropoulos, C. P. (2006). Ablation of thin metal films by short-pulsed lasers coupled through near-field scanning optical microscopy probes. *Journal of Applied Physics, 99*(4), 044905.

Ibrahim, W., Elsayed-Ali, H., Shinn, M., & Bonner, C. (2003). Femtosecond damage threshold of multi-layer metal films *SPIE proc., 4932*.

Ihlemann, J., Wolff, B., & Simon, P. (1991). Nanosecond and Femtosecond Excimer Laser Ablation of Fused Silica. *Appl. Phys. A, 54*, 363.

Ihtesham, H., Chowdhury, & Xianfan, X. (2003). Heat transfer in femtosecond laser processing of metal. *Numerical Heat transfer A 44*, 219-232.

Ihtesham, H., Xianfan, X., & Andrew, M. W. (2003). Ultrafast pulse train micromachining. *Proc. of SPIE, 4978*, 138.

Jiang, L., & Tsai, H.-L. (2007). Modeling of ultrashort laser pulse-train processing of metal thin films. *International Journal of Heat and Mass Transfer, 50*(17-18), 3461-3470.

Kaganov, M. I., Lifshitz, I. M., & Tanatarov, L. V. (1957). Relaxation between electrons and the crystalline lattice

Sov. Phys. JETP, 4.

Karakas, A., Tunc, M., & Camdali, Ü. (2010). Thermal analysis of thin multi-layer metal films during femtosecond laser heating. *Heat and Mass Transfer, 46*(11-12), 1287-1293.

Kelly, R., & Miotello, A. (1996). Comments on explosive mechanisms of laser sputtering *Applied Surface Science, 96-98*.

Kiiper, S., & Stuke, M. (1987). Femtosecond UV Excimer Laser Ablation. *Appl. Phys. B, 44*, 199.

Kim, J., & Na, S. (2007). Metal thin film ablation with femtosecond pulsed laser. *Optics & Laser Technology, 39*(7), 1443-1448.

Komashko, A. M., Feit, M. D., Rubenchik, A. M., Perry, M. D., & Banks, P. S. (1999). Simulation of material removal efficiency with ultrashort laser pulses. *Applied Physics A, 69*(1 (supplement)), S95.

Lee, H., Jeong, Y.-U., & Chan, K. F. (2009). The Advent of Laser Therapies in Dermatology and Urology: Underlying Mechanisms, Recent Trends and Future Directions. *Journal of the Optical Society of Korea, 13*(3), 321-329.

Lee, J. B., Kang, K., & Lee, S. H. (2011). Comparison of Theoretical Models of Electron-Phonon Coupling in Thin Gold Films Irradiated by Femtosecond Pulse Lasers. *Materials Transactions, 52*(3), 547-553.

Lee, J. B., & Lee, S. H. (2011). Thermal Boundary Resistance Effect on Non-Equilibrium Energy Transport in Metal-Dielectric Thin Films Heated by Femtosecond Pulse Lasers. *Materials Transactions, 52*(7), 1492-1499.

Lewis, L. J., & Perez, D. (2009). Laser ablation with short and ultrashort laser pulses: Basic mechanisms from molecular-dynamics simulations. *Applied Surface Science, 255*(10), 5101-5106.

Lin, Z., & Zhigilei, L. (2007). THE ROLE OF THERMAL EXCITATION OF D BAND ELECTRONS IN ULTRAFAST LASER INTERACTION WITH NOBLE (Cu) AND TRANSITION (Pt) METALS *Proceedings of MNC2007*

Lin, Z., Zhigilei, L., & Celli, V. (2008). Electron-phonon coupling and electron heat capacity of metals under conditions of strong electron-phonon nonequilibrium. *Physical Review B, 77*(7).

Liu, K.-C. (2007). Analysis of thermal behavior in multi-layer metal thin films based on hyperbolic two-step model. *International Journal of Heat and Mass Transfer, 50*(7-8), 1397-1407.

Liu, X., Du, D., & Mourou, G. (1997). Laser Ablation and Micromachining with Ultrashort Laser Pulses. *JOURNAL OF QUANTUM ELECTRONICS, 33*, 1706.

Lorazo, P., Lewis, L., & Meunier, M. (2003). Short-Pulse Laser Ablation of Solids: From Phase Explosion to Fragmentation. *Physical Review Letters, 91*(22).

Luft, A., Franz, U., Emsermann, A., & Kaspar, J. (1996). A study of thermal and mechanical effects on materials induced by pulsed laser drilling. *Appl. Phys. A, 63*, 93.

Margetic, V., Bolshov, M., Stockhaus, A., Niemax, K., & Hergenrder, R. (2001). Depth profiling of multi-layer samples using femtosecond laser ablation. *Journal of Analytical Atomic Spectrometry, 16*(6), 616-621.

Marla, D., Bhandarkar, U. V., & Joshi, S. S. (2011). Critical assessment of the issues in the modeling of ablation and plasma expansion processes in the pulsed laser deposition of metals. *Journal of Applied Physics, 109*(2), 021101.

Martynyuk, M. M. (1974). Vaporization and Boiling of Liquid Metal in an Exploding Wire. *Soviet Physics Technical Physics, 19*.

Martynyuk, M. M. (1977). Phase explosion of a metastable fluid. *Combustion, Explosion and Shock Waves, 13*(2), 178.

Martynyuk, M. M. (1993). Transition of liquid metals into vapor in the process of pulse heating by current. *International Journal of Thermophysics, 14*.

McMillan, W. (1968). Transition Temperature of Strong-Coupled Superconductors. *Physical Review, 167*(2), 331-344.

Meunier, M., Gruzdev, V., Tzou, R., Salakhutdinov, I., Danylyuk, Y., McCullen, E., et al. (2009). Ablation of aluminum nitride films by nanosecond and femtosecond laser pulses</title>. *7201*, 72011B-72011B-72010.

Nedialkov, N. N., Imamova, S. E., Atanasov, P. A., Berger, P., & Dausinger, F. (2005). Mechanism of ultrashort laser ablation of metals: molecular dynamics simulation. *Applied Surface Science, 247*(1-4), 243-248.

Nolte, S., Momma, C., Jacobs, H., Tu¨nnermann, A., Chichkov, B. N., Wellegehausen, B., et al. (1997). Ablation of metals by ultrashort laser pulses. *J. Opt. Soc. Am. B, 14*(10), 2716.

Oh, B., Kim, D., Kim, J., & Lee, J.-H. (2007). Femtosecond laser ablation of metals and crater formation by phase explosion in the high-fluence regime. *Journal of Physics: Conference Series, 59*, 567-570.

Oraevsky, A. A., DaSilva, L. B., Feit, M. D., Glinsky, M. E., Mammini, B. M., Paquette, K. L., et al. (1995). Plasma Mediated Ablation of Biological Tissues with Ultrashort Laser Pulses. *Proc. SPIE, 2391*, 423-431.

Perez, D., & Lewis, L. (2002). Ablation of Solids under Femtosecond Laser Pulses. *Physical Review Letters, 89*(25).

Phipps, C. R., Lin, Z., & Zhigilei, L. V. (2006). <title>Thermal excitation of d band electrons in Au: implications for laser-induced phase transformations</title>. *6261*, 62610U-62610U-62614.

Preuss, S., Demchuk, A., & Stuke, M. (1995). Sub-picosecond UV laser ablation of metals. *Appl. Phys. A, 61*, 33.

Pronko, P. P., Dutta, S., Squier, J., Rudd, J. V., Du, D., & Mourou, G. (1994). Machining of sub-micron holes using a femtosecond laser at 800 nm. *Optics Communications, 114*, 106.

QIU, Q., JUHASZ, T., SUAREZ, C., W, B., & TIEN, C. L. (1994). Femtosecond laser heating of multi-layer metals-II. Experiments *Int. J Heat Mass Transfer, 37*.

Qiu, T. Q., & Tien, C. L. (1993). Heat transfer mechanisms during short-pulse laser heating of metals. *Journal of Heat Transfer, 115*, 835.

QIU, T. Q., & TIEN, C. L. (1994). Femtosecond laser heating of multi-layer metals-l. Analysis. *Int. J Heat Mass Transfer, 37*.

Ren, Y., Chen, J. K., & Zhang, Y. (2011). Optical properties and thermal response of copper films induced by ultrashort-pulsed lasers. *Journal of Applied Physics, 110*(11), 113102.

Ren, Y., Chen, J. K., Zhang, Y., & Huang, J. (2011). Ultrashort laser pulse energy deposition in metal films with phase changes. *Applied Physics Letters, 98*(19), 191105.

Schäfer, C., Urbassek, H., & Zhigilei, L. (2002). Metal ablation by picosecond laser pulses: A hybrid simulation. *Physical Review B, 66*(11).

Shirk, M. D., & Molian, P. A. (1998). A review of ultrashort pulsed laser ablation of materials. *JOURNAL OF LASER APPLICATIONS, 10*, 18.

Shubhrokallol. (May 2013). Explosive boiling or phase explosion - p-T diagram. from commons.wikimedia.org/wiki/File:Explosive_boiling_or_phase_explosion_-_p-T_diagram.jpg

Sitnikov, D. S., & Ovchinnikov, A. V. (2011). Application of Femtosecond Laser pulses for Nanometer Accuracy Profiling of Quartz and Diamond Substrates and for Multi-Layered Targets and Thin-Film Conductors Processing. *World Academy of Science, Engineering and Technology, 5*.

Sokolowski-Tinten, K., Bialkowski, J., Cavalleri, A., & von der Linde, D. (1998). Transient States of Matter during Short Pulse Laser Ablation. *physical Review Letters, 81*, 224.

Sonntag, S., Roth, J., Gaehler, F., & Trebin, H. R. (2009). Femtosecond laser ablation of aluminium. *Applied Surface Science, 255*(24), 9742-9744.

Tan, X.-y., Zhang, D.-m., Mao, F., Li, Z.-h., Yi, D. I., & Zhang, X.-z. (2009). Theoretical and experimental study of energy transportation and accumulation in femtosecond laser ablation on metals. *Transactions of Nonferrous Metals Society of China, 19*(6), 1645-1650.

Tien, C. L., Majumdar, A., & Gerner, F. M. (1998). *microscale energy transport*.

Tzou, D. Y., Chen, J. K., & Beraun, J. E. (2002). Hot-electron blast induced by ultrashort-pulsed lasers in layered media. *International Journal of Heat and Mass Transfer, 45*.

Veal, B., & Rayne, J. (1962). Heat Capacity of β-CuZn below 4.2°K. *Physical Review, 128*(2), 551-555.

Vidal, F., Johnston, T., Laville, S., Barthélemy, O., Chaker, M., Le Drogoff, B., et al. (2001). Critical-Point Phase Separation in Laser Ablation of Conductors. *Physical Review Letters, 86*(12), 2573-2576.

Wang, H., Dai, W., & Melnik, R. (2006). A finite difference method for studying thermal deformation in a double-layered thin film exposed to ultrashort pulsed lasers. *International Journal of Thermal Sciences, 45*(12), 1179-1196.

Wu, B., & Shin, Y. C. (2007). A simple model for high fluence ultra-short pulsed laser metal ablation. *Applied Surface Science, 253*(8), 4079-4084.

Xu, X., Cheng, C., & Chowdhury, I. H. (2004). Molecular Dynamics Study of Phase Change Mechanisms During Femtosecond Laser Ablation. *Journal of Heat Transfer, 126*(5), 727.

Xu, X., & Willis, D. A. (2002). Non-Equilibrium Phase Change in Metal Induced by Nanosecond Pulsed Laser Irradiation. *Journal of Heat Transfer, 124*(2), 293.

Yilbas, B. S. (2002). Short-pulse laser heating of gold-chromium layers: thermo-elasto-plastic analysis. *JOURNAL OF PHYSICS D: APPLIED PHYSICS, 35*.

Zeng, X., Mao, X. L., Greif, R., & Russo, R. E. (2004). Experimental investigation of ablation efficiency and plasma expansion during femtosecond and nanosecond laser ablation of silicon. *Applied Physics A, 80*(2), 237-241.

Zhang, Y., & Chen, J. K. (2007). Melting and resolidification of gold film irradiated by nano- to femtosecond lasers. *Applied Physics A, 88*(2), 289-297.

Zhigilei, L. V., Lin, Z., & Ivanov, D. S. (2009). Atomistic Modeling of Short Pulse Laser Ablation of Metals: Connections between Melting, Spallation, and Phase Explosion. *J. Phys, Chem. C, 113*(27), 11892.

VITA

VITA

Ghadeer H. Al-Malkawi
Graduate School, Purdue University

Education

B.S., Chemical Engineering, 2007, Jordan University of Science and Technology, Irbid, Jordan
M.S., Nuclear Engineering, 2013, Purdue University, West Lafayette, Indiana
Ph.D., Nuclear Engineering, 2014, Purdue University, West Lafayette, Indiana

Research Interests

Numerical simulation of heat transfer
Thermal response of material under intense radiation
Radiation damage in materials